

## Stress-strain characterization of human bone

**Auteur :** p207972

**Promoteur(s) :** Ruffoni, Davide

**Faculté :** Faculté des Sciences appliquées

**Diplôme :** Master en ingénieur civil biomédical, à finalité spécialisée

**Année académique :** 2022-2023

**URI/URL :** <http://hdl.handle.net/2268.2/22264>

---

### *Avertissement à l'attention des usagers :*

*Tous les documents placés en accès ouvert sur le site le site MatheO sont protégés par le droit d'auteur. Conformément aux principes énoncés par la "Budapest Open Access Initiative"(BOAI, 2002), l'utilisateur du site peut lire, télécharger, copier, transmettre, imprimer, chercher ou faire un lien vers le texte intégral de ces documents, les disséquer pour les indexer, s'en servir de données pour un logiciel, ou s'en servir à toute autre fin légale (ou prévue par la réglementation relative au droit d'auteur). Toute utilisation du document à des fins commerciales est strictement interdite.*

*Par ailleurs, l'utilisateur s'engage à respecter les droits moraux de l'auteur, principalement le droit à l'intégrité de l'oeuvre et le droit de paternité et ce dans toute utilisation que l'utilisateur entreprend. Ainsi, à titre d'exemple, lorsqu'il reproduira un document par extrait ou dans son intégralité, l'utilisateur citera de manière complète les sources telles que mentionnées ci-dessus. Toute utilisation non explicitement autorisée ci-avant (telle que par exemple, la modification du document ou son résumé) nécessite l'autorisation préalable et expresse des auteurs ou de leurs ayants droit.*

---



UNIVERSITY OF LIEGE  
FACULTY OF APPLIED SCIENCES

---

# Stress-strain characterisation of fibrolamellar bone

---

Master thesis conducted by  
**GAËLLE SANDRONT**  
with the aim of obtaining the degree of Master in Biomedical  
Engineering

Supervisor  
DAVIDE RUFFONI

Co-supervisor  
CANTAMESSA ASTRID

ACADEMIC YEAR 2022-2023





# Abstract

Fibrolamellar bone is found in animals experiencing rapid growth phases, which makes it intriguing to researchers studying rapid bone development, such as during bone healing. This bone variety is composed of three discernible structures located between two blood vessels. The initial stage involves the formation of hypercalcified bone, acting as a supportive scaffold for the subsequent emergence of parallel-fibered bone. Eventually, a layer of lamellar bone is laid down, further enhancing this structure. The mechanical characteristics of fibrolamellar bone across these distinct layers remain largely unexplored, which is regrettable given its potential significance and interest.

This thesis strives to enhance our comprehension of the mechanical characteristics exhibited by fibrolamellar through a detailed analysis of its stress-strain behaviour with a keen focus on the lamellar region. Furthermore, another objective is to gain deeper insights into how variations in surface roughness impact the analyses. The results are derived using a method known as nanoindentation, which is utilised to measure mechanical properties with nanoscale precision. Utilising the data from nanoindentation, and applying the Olivier-Pharr model, it becomes possible to compute stress-strain behaviour.

The initial phase of this thesis required a calibration procedure to ensure precise outcomes. This calibration process was executed on fused quartz, chosen due to its well-established Young's modulus and being considered as perfect with no impurity.

In the second part, a more comprehensive exploration of fibrolamellar bone is conducted. Nanoindentation is employed to derive stress-strain curves and determine the Young's modulus in a specific location. Furthermore, scanning electron microscopy aids in pinpointing indentation locations and quantifying lamellar thickness. The investigation revealed that thick lamellae are stiffer than their thin counterparts. However, establishing a direct correlation with the stress-strain curves proved challenging due to the influence of surface roughness on the sample, which affected the outcomes. The curves of thick lamellae display an initial linear elastic phase followed by a swift yielding, while those from thin lamellae showcase a more compliant behaviour. This contrast is likely attributed to the differing orientation of collagen fibers between the two lamellae types. Furthermore, the study also revealed that parallel-fibered bone displays a high stiffness.

In conclusion, this study is pioneering, offering a methodology to comprehensively understand and correlate mechanical properties with underlying structures. Future research could apply this approach to further elucidate the impact of roughness on fibrolamellar bone or explore its applicability to osteons, given their shared characteristics.

# Acknowledgements

I embarked on this thesis as my first foray into the world of research, an endeavor I found incredibly fascinating and rewarding. As the culmination of this journey, my writing process has been both a challenging and fulfilling experience. Thus, I would like to express my heartfelt gratitude to several individuals who played pivotal roles in making this endeavor possible.

Foremost, I extend my deepest appreciation to my thesis promoter, Professor Ruffoni. His guidance, encouragement, and the opportunity to explore this subject have been invaluable. His patience in addressing my questions and his insightful tips on writing have significantly contributed to the completion of this thesis.

I am also grateful to the entire team at the MBBM lab. Their collective support and environment of collaboration have provided me with a wealth of insights and inspiration. A special acknowledgment goes to Astrid Cantamessa for her generosity in sharing her time and knowledge. Her willingness to answer my numerous questions and provide helpful guidance has been instrumental in shaping this work.

I would also like to express my gratitude to Professor Philippe Compere for generously dedicating his time to capture the images using scanning electron microscopy.

Lastly, my heartfelt thanks go out to my friends and family. Their unwavering encouragement, emotional support, and patience during this academic journey have meant the world to me. I acknowledge that dealing with my evolving moods and challenges was not always easy, and their steadfast presence has been a pillar of strength.

This thesis is not only a representation of my academic accomplishments but also a testament to the collective efforts of those who believed in me and contributed to my growth. Thank you.

# Contents

<b>Abstract</b>	<b>I</b>
<b>Acknowledgements</b>	<b>II</b>
<b>Introduction</b>	<b>1</b>
<b>1 Background</b>	<b>3</b>
1.1 Bones . . . . .	3
1.1.1 Generalities . . . . .	3
1.1.2 Trabecular bones . . . . .	5
1.1.3 Cortical bone . . . . .	7
1.1.4 Bone remodelling process . . . . .	10
1.1.5 Hierachy of bones . . . . .	13
1.1.6 Fibrolamellar bone . . . . .	17
1.2 Scanning electron microscopy . . . . .	20
1.3 Nanoindentation . . . . .	22
1.4 Main aim of This Thesis . . . . .	23
<b>2 Methodology</b>	<b>25</b>
2.1 Sample preparation . . . . .	25
2.2 Nanoindenter . . . . .	26
2.2.1 System . . . . .	27
2.2.2 Scanning probe microscopy . . . . .	28
2.2.3 Calibration of the transducer . . . . .	28
2.2.4 Cleaning of the tip . . . . .	29
2.2.5 Tip calibration . . . . .	29
2.2.6 Sample measurement . . . . .	34
2.2.7 Static indent . . . . .	36
2.2.8 Summary of the protocol . . . . .	36
2.2.9 Impact of the roughness. . . . .	37
2.2.10 Impact of the fitting equation . . . . .	38
2.3 Scanning electron microscopy . . . . .	40

<b>3</b>	<b>Results</b>	<b>41</b>
3.1	Data Structuring . . . . .	41
3.2	Nanoindentation tests . . . . .	42
3.2.1	Sample 1 . . . . .	42
3.2.2	Sample 2 . . . . .	49
3.3	Scanning electron microscopy . . . . .	63
3.3.1	Sample 1 . . . . .	63
3.3.2	Sample 2 . . . . .	64
<b>4</b>	<b>Discussion</b>	<b>69</b>
4.1	Scanning electron microscopy . . . . .	69
4.2	Static indentation . . . . .	70
4.3	Stress-strain curves . . . . .	71
4.3.1	Parallel-fibered bone . . . . .	71
4.3.2	Lamellar bone . . . . .	71
4.3.3	Impact of roughness . . . . .	72
4.4	Limitations . . . . .	73
4.5	Future Works . . . . .	73
	<b>Conclusion</b>	<b>75</b>
	<b>Appendices</b>	<b>76</b>
<b>A</b>	<b>Nanoindentation test</b>	<b>78</b>
A.1	Zone 1b . . . . .	78
A.2	Zone 1c . . . . .	81
<b>B</b>	<b>SEM picture</b>	<b>84</b>
B.1	Sample 1 . . . . .	84
B.2	Sample 2 . . . . .	84
	<b>Bibliography</b>	<b>90</b>

# Introduction

Bone is an intriguing material due to its unique properties. Its remarkable combination of strength and lightweight structure makes it a model for efficiency in engineering. Beyond its mechanical attributes, bones play a crucial role in supporting and protecting the body, while their ability to self-heal has implications for material design.

Due to its composition, bone possesses high stiffness and toughness. Nature achieves this intricate balance of qualities, which is challenging to replicate artificially. While stiffness imparts stability, toughness allows bones to endure impacts without breaking. This remarkable duality is only found only in nature.

Bone is classified as a hierarchical material, meaning that distinct structures are present at different levels of observation. With advancements in technology, it is now possible to delve into smaller scales, such as the nano or micro levels, for in-depth exploration. An interesting type of bone is fibrolamellar bone found in animals experiencing rapid growth phases, which makes it intriguing to study. This bone type consists of diverse structures, each holding its own significance in enabling such rapid growth.

This thesis aims to deepen our understanding of the mechanical properties of fibrolamellar bone by extensively analysing its local stress-strain behaviour, particularly in the lamellar region. Additionally, it seeks to explore how surface roughness variations influence the analyses. The study employs nanoindentation, a technique for nanoscale precision in assessing mechanical properties. Utilising nanoindentation data and the Olivier-Pharr model enables the computation of local stress-strain behaviour, a groundbreaking approach never before applied to fibrolamellar bone. This thesis is organised into four main chapters.

The first chapter introduces the background information, elucidating the overarching concepts central to this thesis. Within this section, insights into fibrolamellar bone are provided. Additionally, a comprehensive understanding of the functions of scanning electron microscopy, along with the underlying principles of nanoindentation techniques, is presented. The concluding segment of this chapter is dedicated to outlining the objectives pursued throughout the thesis.

The second chapter is devoted to the experimental part of this master thesis. First the

sample preparation is explained. Subsequently, the methodology utilised for deriving stress-strain curves is expounded upon. Within the same section, the calibration approach employed is also detailed. Finally, the chapter concludes by outlining the method employed for data acquisition using scanning electron microscopy.

The third one showcases the presented results. It features the presentation of stress-strain curves that have been obtained, accompanied by an evaluation of the indents roughness. Following this, the chapter provides a visual representation of scanning electron microscopy images, and in conjunction, outlines the measurements of lamellae thicknesses.

The final chapter of this thesis engages in a comprehensive analysis of the achieved results. Additionally, it addresses the limitations encountered during the study and provides insights into future perspectives.

# Chapter 1

## Background

The aims of this chapter is to provide the general context of the project. In the first section some generalities about the bone is be given as well as a deeper description of fibrolamellar bone. Subsequently, a description of the scanning electron microscopy is given. Then a section is devoted to the nanoindentation technique. Finally, the main aims of this thesis are underlined.

### 1.1 Bones

#### 1.1.1 Generalities

Bones are integral to the musculoskeletal system and play a crucial role in ensuring the system fulfils its purpose. Indeed it has 4 functions [1, 2, 3]:

1. Haematopoiesis: It's the formation of red blood cells and stem cells in the red bone marrow found in trabecular bone.
2. Mineral storage: The skeleton is considered the mineral bank of our body as it contains approximately 99% of the Calcium ( $Ca^{2+}$ ) and Phosphorus. The rest of Calcium is found in the blood and is regulated thanks to the remodelling process.
3. Protection of vital organs: Bone combines high energy absorption and low weight allowing protection.
4. Support and motion: The skeleton supports the body and the combination of bones, muscles and joints allows the motion of the body.

Bones are composed of an organic phase (protein), an inorganic phase (mineral crystals) and water. Their proportion will differ if we consider their weight (wet) and volume as represented in FIGURE 1.1. The organic phase is mainly composed of collagen type I and the inorganic phase is composed of hydroxyapatite [1, 2, 3]. Bone composition is discussed later in SUBSECTION 1.1.5.



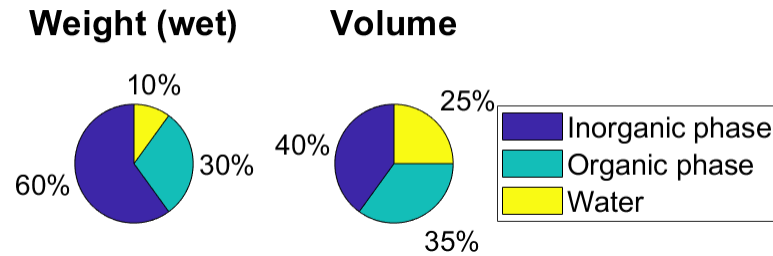


Figure 1.1: Composition of bone [3].

Varieties of bones exist within the body, each characterised by unique structure and function. They are discernible based on size and shape, and their representation is depicted in FIGURE 1.2. This section delves into these bone types, with a specific focus on long bones, given their central role of study in this thesis.

► Flat bones

These types of bones protect vital organ and muscle attachment [3, 4]. They are mostly part of the skull but they are also found in other parts of the body, e.g. the scapula.

► Short bones

These small bones offer resistance to compression and are present within the joints of the skeleton, as well as in the ankle and wrist articulations [3, 4]. They have a plethora of shapes and are lightweight and highly porous which made them suitable for energy absorption.

► Long bones

These bones provide stability against bending and buckling [3, 4]. They are found in the legs, arms, fingers, and toes, e.g. the tibia. In order to achieve this function, it needs to have a high rigidity and to be lightweight. They are elongated along the main axis, cylindrical and rounded at the extremities.

The structure of long bone is divided into three main regions as illustrated in FIGURE 1.3. At the extremities, the epiphysis contains the spongy bone also known as trabecular bones. The central part, or diaphysis, is filled with compact bone called cortical bone. Finally, between these two regions, there is the metaphysis which also contains spongy bones[3, 5].

The epiphyseal line separates the metaphysis from the epiphysis. It progress from the epiphyseal plate responsible for longitudinal bone growth [6]. The periosteum, an outer bone membrane, comprises two distinct layers: the outer layer is more fibrous, while the inner one contains more cells such as osteoblasts and endothelial pericytes, involved in bone formation [7]. Another connective tissue, the endosteum, houses quiescent osteoblasts and osteoclasts

[8]. Similar to osteoblasts, osteoclasts also contribute to bone formation and, more broadly, to bone homeostasis. As the name suggests, bone lining cells are located on the surfaces of the bone and play a crucial role in bone remodelling [9]. These types of cells and processes are described in more details in SUBSECTION 1.1.4.

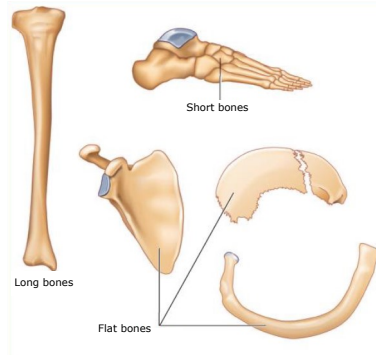


Figure 1.2: Types of bones (adapted from [4]).

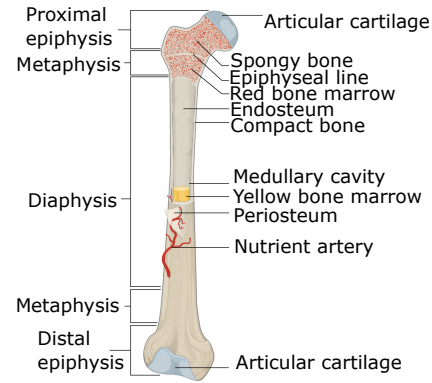


Figure 1.3: Structure of long bones (adapted from [10]).

### 1.1.2 Trabecular bones

As previously stated, trabecular bones are located at the ends of long bones as well as within flat and irregular bones and within the vertebral bodies [3]. They compose approximately 20% mass of the adult human skeleton [2].

#### ► Structure

Trabecular bones consist of spongy and porous materials, composed of trabeculae and pores. These trabeculae are either plate-like or rod-like, and the pores are interconnected and filled with red marrow [6, 3] as shown in Figure 1.4. The pore dimensions are typically in the order of  $10^3 \mu\text{m}$ , while the trabeculae are in the order of  $10^2 \mu\text{m}$  [3, 11]. This type of bone presents low density, reaching a porosity of 75% to 95%. This density gradually decreases as the shaft of the bone is reached, allowing the bone to remain lightweight while carrying significant loads with low stress at the metaphysis and high stress at the diaphysis (cortical bone) [12]. The shapes of trabeculae vary depending on their location, and they measure approximately  $100 - 150 \mu\text{m}$  thick [12]. Two more factors can also influence the shape: loading and age. Indeed, with aging, the porosity increases, causing the trabeculae to adopt a rod-like appearance [13]. As for loading, in areas experiencing higher compressive forces, the trabeculae become thicker and more closely spaced, looking more like plates. On the other hand, in regions experiencing more tensile forces, the trabeculae become thinner, appearing more like rods [3].

Trabecular bone displays a heterogeneous patchwork-like structure due to the ongoing processes of remodelling and mineralisation. This structure is composed of various bone

packets, each exhibiting distinct mineral content, stiffness, and age, as represented in FIGURE 1.5. The depicted figure showcases different levels of grey, corresponding to varying mineral content within the bone. A dark shade indicates a lower mineral content while a light one indicates higher mineral content. This variation in mineral content significantly impacts the mechanical properties. Indeed, as the mineral content increases, the bone becomes stiffer [14].

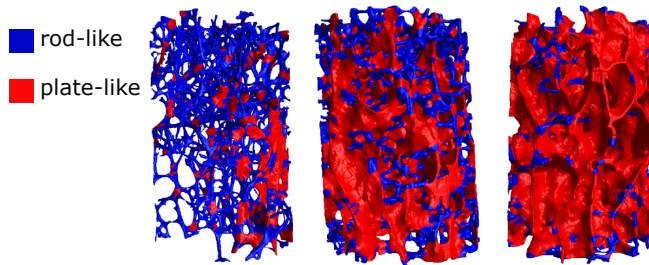


Figure 1.4: Different structures of trabeculae: rod-like, hybrid and plate-like from left to right (adapted from [15]).

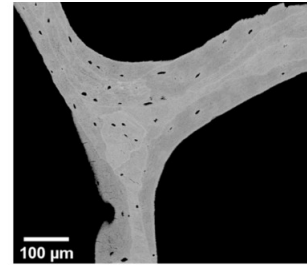


Figure 1.5: Patchwork-like structure present in trabecular bone (adapted from [16]).

#### ► Mechanical properties

Trabecular bone displays anisotropy and is considered as an orthotropic material [17]. Its mechanical behaviour is often attributed to the interaction between bone architecture and bone tissue [3]. FIGURE 1.6 illustrates the stress-strain curves, exhibiting three distinct regions: the linear elastic region, the plateau region and the densification region. These curves may vary depending on the relative densities of trabecular bones which differ based on their location[3].

At low levels of strains, the bone behaves linearly until the trabecular rods and plates start to collapse under increased stress. The peak observed at the end of this linear region is known as the yield point. Beyond this point, the bone starts to be damaged plastically, i.e. when the load is removed, the bone will not be able to recover its initial configuration. The collapse of trabeculae enables the bone to undergo a large amount of compressive strain without experiencing an increase in stress. Consequently, the bone can store a considerable amount of energy. When the trabeculae come into contact with each other, causing a reduction in porosity, the stress quickly intensifies [3, 1].

Trabecular bone is a highly heterogeneous material, making it challenging to describe its mechanical properties with a single average value. For this reason, the apparent density is commonly chosen to describe this type of bone. Indeed, this parameter has the greatest influence on the elasticity and failure characterised by the Young's modulus  $E$  (the stiffness of a material) and ultimate stress  $\sigma_u$  (stress a material can withstand before breaking) respectively. A correlation between the apparent density and both mechanical parameters can

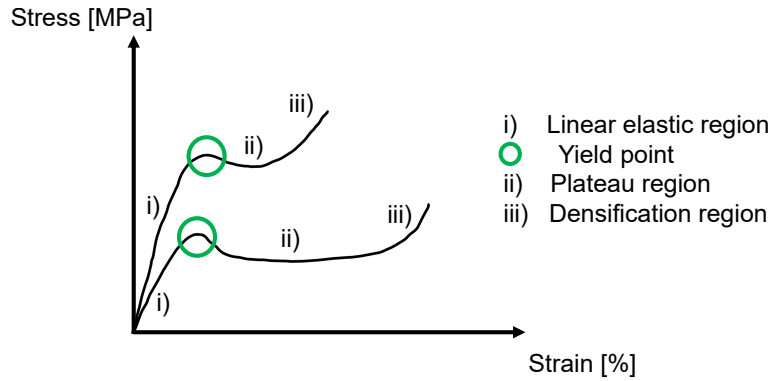


Figure 1.6: Stress-strain curves of trabecular bone loaded under compression (inspired from [12]).

be computed and is written in EQUATION 1.1 and 1.2 respectively. In both cases, the Young's modulus and ultimate stress increase with the apparent density. Indeed, more material in a bone increases its stiffness and strength [3, 1].

$$E \propto (\rho_{app})^2 \quad (1.1)$$

$$\sigma_u \propto (\rho_{app})^{2.2} \quad (1.2)$$

It is important to note that two types of bone can have the same apparent density but not the same architecture. Consequently, their mechanical properties will be different. Moreover, the stress-strain presented here is obtained under compression. If the tests were conducted under tension, the curves would be different.

### 1.1.3 Cortical bone

As previously stated cortical bone is located under the periosteum and in the diaphyses of long bones. Approximately 80% mass of the adult human skeleton is composed of this type of bone [2].

#### ► Structure

During the developmental stage in young individuals, the structure of cortical bone is characterised by the presence of primary osteons. By contrast, in mature individuals, cortical bone becomes more ordered, uniform, and developed due to the ongoing remodelling process [12]. In adults, cortical bone is composed of lamellar and osteonal bone also called Haversian bone as illustrated in FIGURE 1.7. Lamellar bone is made of large concentric rings of lamellae around the outer 2 – 3 mm of the diaphysis and within the osteons (interstitial lamellae). Additional detail are given on them in SECTION 1.1.5. Osteonal bone consists of roughly 10-15 lamellae, arranged in concentric cylinders encircling a central Haversian canal

that facilitates the passage of blood vessels [3]. This canal possesses an approximate diameter of  $50\text{ }\mu\text{m}$  and is oriented parallel to the main axis of bone. The structural units of cortical bone, known as osteons, typically have a diameter ranging from  $100\text{--}200\text{ }\mu\text{m}$  and extend in length from  $1\text{--}3\text{ mm}$  [18, 12]. In the areas between these osteons, interstitial bone can be found, representing the bone tissue that remains after the remodelling process [12].

Compared to trabecular bone, cortical bone exhibits a lower porosity, resulting in a higher density. This is due to the fact that it has to withstand compressive force as well as provide support and protection. Its porosity varies with age from 8% to 5% as there is a higher nutrient demand during bone growth. The porosity comes from the Haversian and Volkmann canals, as well as the osteocyte lacunae and canaliculi of the osteocyte lacunocanalicular network [19]. The Haversian canal serves as the primary channel within the osteons, allowing blood vessels to pass through. Surrounding this, there is the lacuna-canalicular porosity, formed by canaliculi and ellipsoidal-shaped osteocyte lacunae. These regions remain unmineralised and house the osteocytes. The canaliculi are small canals connecting the Haversian canals with osteocytes and also linking them with the periosteum, representing the external layer of long bones. The changes in cortical bone porosity and the presence of these components are essential for bone growth, remodelling, and overall bone health throughout an individual's life.

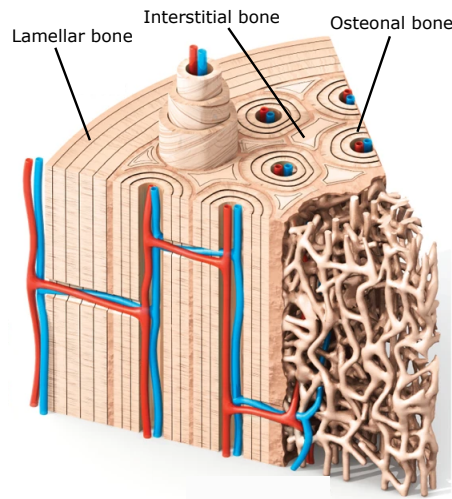


Figure 1.7: Structure of cortical bone (adapted from [20]).

#### ► Mechanical properties

Cortical bone is assumed to behave like a ductile material, and as such, its stress-strain curves can be represented by FIGURE 1.8, obtained under compression. This curve is divided into two zones: an elastic region and a plastic region. The slope of the first zone is used to compute the Young modulus. The end of this elastic region, i.e. the elastic limit, is repre-

sented by the yield point, characterised by a yield stress and strain. Beyond this point, the bone is deformed plastically which means that once the load is removed, the bone do not recover its initial shape. Then, in the plastic region, the bone continues to deform plastically and the curve stops once the material break. This break occurs at the failure point, characterised by the ultimate stress and strain.

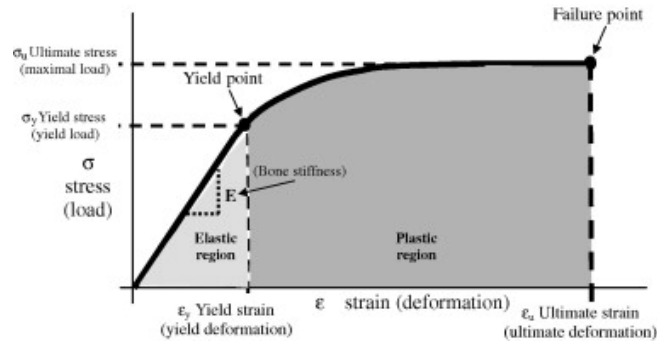


Figure 1.8: Stress-strain curve for a ductile material loaded under compression [21].

In fact, due to its specific structure, cortical bone exhibits anisotropic behaviour, meaning its mechanical properties vary depending on the direction of the applied load, as depicted in FIGURE 1.9. In longitudinal loading, the bone behaves as a ductile material and the ultimate stress is higher in compression while the ultimate strain is higher in tension. In transverse loading, the bone behaves as a brittle material and the ultimate stress and strain are both higher in compression. However, the yield stress remains constant despite the anisotropy.

Furthermore, cortical bone exhibits greater strength in longitudinal loading, which is expected considering that most of the forces are applied in this direction, and the bone has adapted its structure accordingly. Similarly, cortical bone demonstrates higher strength in compression, as it is more frequently subjected to such forces. These observations are illustrated in FIGURE 1.9.

The mechanical properties of cortical bones are affected by porosity, mineral content, and ageing. As time elapses, the porosity of cortical bones may change due to alterations in the quantity, size, and dimensions of Haversian and Volkmann's canals, consequently affecting their overall mechanical behaviour. When the porosity decreases, the ultimate stress and Young's modulus increase as the amount of material increases too. Regarding the mineral content, in healthy individuals there is not much variation, and thus it does not significantly impact the Young's modulus. Nonetheless, differences can be observed between young and mature bone. Finally, the age also play a role. Indeed, the Young's modulus decreases slightly and the ultimate stress decreases by 1% every year. As a result old bone becomes more brittle. Additionally, ageing also correlates positively with porosity.

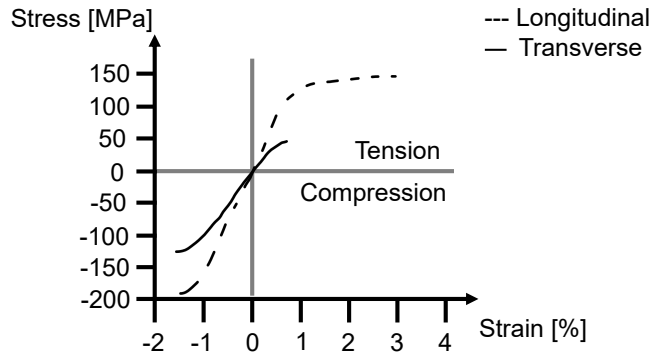


Figure 1.9: Stress-strain behaviour of adult human cortical bone samples in the transverse and longitudinal direction for compression and tension (inspired from [3]).

In situ, water is found in the bone inducing a viscoelastic effect. Nonetheless, if physiological strain rates are considered i.e.  $0.01 - 1$  %/second, these effects can be neglected. Otherwise, the stiffness and strength increase whereas ultimate strain decreases. This ultimately results in an increase in brittleness.

#### 1.1.4 Bone remodelling process

Bone remodelling has 3 main functions, it allows the bone to [3]:

1. Regulate Calcium homoeostasis which refers to the regulation of calcium within the body. It is essential for various physiological processes, and disturbances in the balance of calcium, whether excessive or deficient, can result in significant medical disorders.
2. Adapt to changes in the loading environment. For instance, engaging in regular sports activities and thus experiencing increased loading leads to an increase in bone mass and reinforcement of bone architecture. In such cases, the cortical thickness can increase up to 40 %. In opposition, if the loading decrease, bone mass reduces, and bone architecture weakens.
3. Replace damaged or old bone. This process allows microcracks within the bone to be repaired.

The process of bone remodelling entails three types of cells: osteoblasts, osteoclasts, and osteocytes. Osteoblasts are responsible for bone formation and are derived from multipotent mesenchymal stem cells [3]. They never work alone, always in clusters and first deposit collagen that must be mineralised. At the end of their process, about 15 % of them become entrapped in the matrix to form osteocytes and the rest remains at the surface to become bone-lining cells [22, 23]. Osteoclasts, derived from multipotent precursor cells, are giant multinucleated cells with a diameter of up to 100  $\mu$ m. They are commonly located near calcified bone surfaces and within lacunae and play a crucial role in bone resorption. They break

down and remove old or damaged bone tissue by digesting the link between the collagen and the hydroxyapatite crystals [22]. They create small cavities in the bone, allowing space for new bone deposition by osteoblasts [3]. Osteocytes are a form of osteoblasts trapped inside the bone matrix during the remodelling. They display different morphologies and activities according to the age of cells. Their activity is reduced but they continue to produce protein matrix[22]. They are interconnected through canaliculi to establish a network capable of detecting structural damage. In other words, they are acting as a strain sensor and detecting detecting mechanical forces and strains [3]. They are digested by osteoclasts during the resorption process. They play a role in the activation of osteoblasts and osteoclasts, although the precise mechanism remains somewhat ambiguous [3, 22, 23].

Therefore, bone remodelling is a dynamic process orchestrated by the coordinated assembly of osteoclasts and osteoblasts, forming distinct and temporary anatomic structures known as basic multicellular units (BMUs). These specialized bone cells work together within the framework of the BMU to achieve efficient bone turnover. While the physical characteristics of BMUs differ between cortical and trabecular bone, their underlying biological functions remain comparable [22, 24]. In cortical bone, BMUs, also known as osteons, has the shape of a cylindrical channel about 150-200  $\mu\text{m}$  wide, as shown in FIGURE 1.11 whose length is about 2000  $\mu\text{m}$  [22]. Ten osteoclasts dig into the bone at a rate of 20-40  $\mu\text{m}$  per day to form this cavity in the main loading direction. Following that, thousands of osteoblasts fill the tunnel, rebuilding the bone. At the end of the process, the cylinder, i.e. osteon is formed and its cavity is filled by one or two blood vessels. Encircling the osteons is a distinctive structure known as the cement line, separating the remodeled portion from the non-remodeled one [25]. Every year, roughly 2% to 5% of cortical bone is remodelled by this process [22]. On the other hand, within trabecular bone, BMUs are bone packets. In this context, osteoclasts have a higher digging speed about 25  $\mu\text{m}$  per day, creating a hole of about 40-60  $\mu\text{m}$  filled by new bone material [22]. At the end of this process, the bone has distinct mineral contents depending on the age of their creation, resulting in a patchwork-like architectural appearance. These bone packs are also bordered by cement lines.

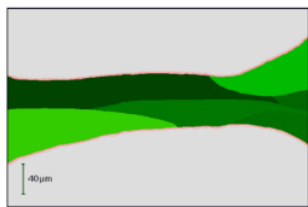


Figure 1.10: Bone packets present at the end of the remodelling process for trabecular bone (adapted from [3]).

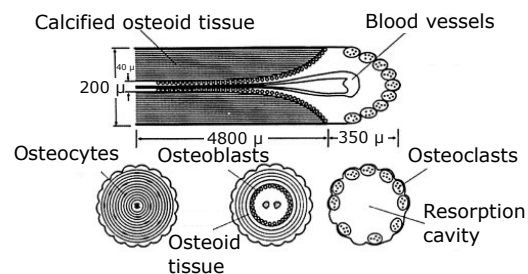


Figure 1.11: Remodelling process in cortical bone (adapted from [26]).



FIGURE 1.12 illustrates the four different phases the bone undergoes to remodel itself. The initial stage of bone remodelling involves resorption, wherein mononuclear preosteoclasts migrate to the targeted area and merge to form multinucleated osteoclasts. This phase typically takes 2 weeks to be completed. Then, the reversal stage begins, during which mononuclear cells appear. These cells play a vital role in preparing the resorbed area for new osteoblasts to initiate bone formation and, providing essential signals that promote osteoblast differentiation and migration. This second step requires approximately 4-5 weeks. Subsequently, the bone remodelling process enters in the formation phase, during which osteoblasts actively deposit new bone to replace the previously resorbed tissue. This phase typically spans approximately four months. Once this phase is completed, flattened lining cells cover the bone, signalling the end of the active remodelling cycle. Finally, the bone undergoes the mineralization process. Subsequent to this mineralization, a resting period commences, during which the bone remains relatively stable until the initiation of a new remodelling cycle in response to the body's physiological demands or external factors. Failure of this process to function effectively can give rise to conditions like osteoporosis [22, 27].

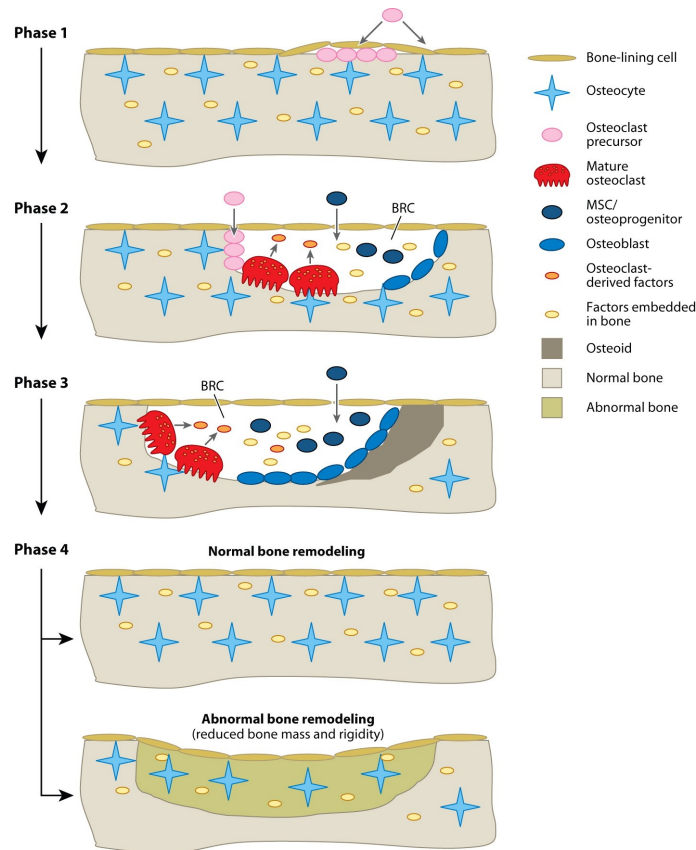


Figure 1.12: Bone remodelling process (adapted from [27]).

### 1.1.5 Hierachy of bones

Bone is an intriguing material that is composed of a plethora of structures spanning various length scales. Gaining a complete understanding of its mechanical properties entails delving into the mechanical traits displayed by its constituent elements, as well as comprehending how these elements are interconnected across various levels of structure. This section explains the hierarchical levels and structures that encompass the macrostructure, microstructure, sub-microstructure, nanostructure, and sub-nanostructure. An overview of all the different structures is provided in FIGURE 1.13

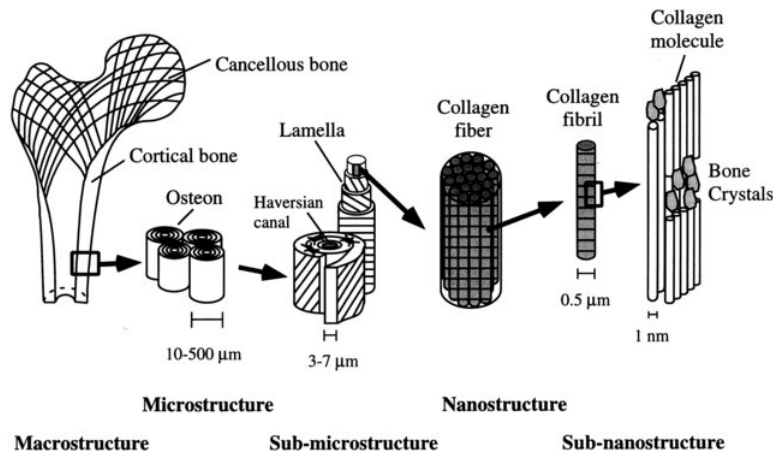


Figure 1.13: Hierarchical structural organisation of bone (from [28]).

► **Macrostructure** ( $cm - mm$ )

At this level, we encounter cortical and trabecular bone which were previously explained in SECTION 1.1.3 and 1.1.2.

► **Microstructure** (10 to 500  $\mu m$ )

At this level, mineralized collagen fibres organise into planar structures known as lamellae, typically ranging from 3 to 7  $\mu m$  in width [28], and their arrangement contributes to the formation of various structural patterns such as osteon (explained in SECTION 1.1.3), lamellar bone and woven bone. Additionally, individual trabeculae can also be observed at this level of examination (explained in SECTION 1.1.2). Finally, there is fibrolamellar bone which is explained in the next section as it is the main focus of this master thesis.

Woven bone is a type of bone tissue that is often formed during the early stages of development and during the process of fracture repair [29]. Indeed, it has a high deposition rate of 4  $\mu m$  per day and thus as a consequence this structure is found in areas that require bone material to grow quickly. Its structure, depicted in FIGURE 1.14 is characterised by collagen fibres with diameters ranging from 0.1 to 3  $\mu m$  with a random orientation [19, 30]. This

arbitrary organisation is due to the high deposition rate and results in a relatively porous material at the microscale as there is a gap between the fibrils. Woven bone contains osteocytes arranged randomly and connected by canaliculi. Although woven bone can achieve a high degree of mineralisation through mineral deposition, its mechanical properties remain weak due to its porosity and its lack of arrangement [19].

Lamellar bone is the mature form of adult bone illustrated in FIGURE 1.15. It has a lower deposition rate than woven bone: less than  $1 \mu\text{m}$  per day [19]. It is characterised by a high level of organisation, with collagen fibrils and minerals arranged precisely in thin sheets called lamellae with alternating thickness, either thin (about  $1 \mu\text{m}$ ) or thick (about  $5 \mu\text{m}$ ) lamellae. Their arrangement resembles a twisted plywood structure (illustrated in FIGURE 1.16), with parallel fibres within each lamella and a consistent angle change between layers. As a consequence, there is no preferred direction enhancing the mechanical properties of the bones. Indeed, these lamellae with different orientations hamper microcrack propagation. Lamellar bone is less mineralised compared to woven bone and thus is more flexible and it can adapt more easily to different mechanical demands. It also contains osteocytes connected together by canaliculi [19].

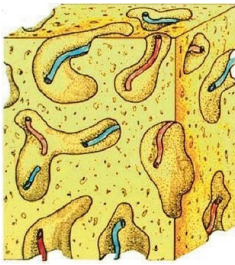


Figure 1.14: Woven bone (from [30]).

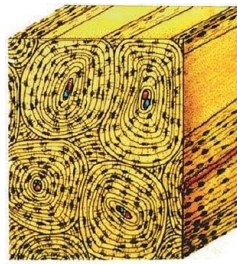


Figure 1.15: Lamellar bone (from [30]).

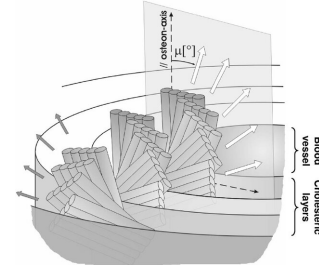


Figure 1.16: Twisted-plywood structure (from [31]).

#### ► Sub-microstructure (1 to $10 \mu\text{m}$ )

At this level, single lamella can be found with an approximate dimension of  $3 - 7 \mu\text{m}$  [28]. The way they are organised will lead to the following different pattern found in bones and explained previously: arrays of parallel fibrils (which leads to parallel-fibered bone), woven fibre structure (which form woven bone), plywood-like structures (which leads to lamellar bone) and radial fibril arrays (which form osteon) [32].

#### ► Nanostructure (100 $\text{nm}$ to $1 \mu\text{m}$ )

At this level, mineralised collagen fibres are composed of tropocollagen molecules, minerals and water which are the basic building blocks of bone as depicted in FIGURE 1.17. The tropocollagen molecules are aligning themselves sequentially and forming connections exclusively with their adjacent molecules. These clusters of collagen molecules are then arranged in

a stacked manner, where each stack is shifted by  $67\text{ nm}$ , resulting in a gap between the starting and ending points of each array of collagen molecules within the structure. Within those holes, mineral crystals nucleate and start to grow in a specific direction forming platelets aligned with the collagen fibrils. The mineral particles have dimensions ranging from  $2\text{-}10\text{ nm}$  in thickness,  $15\text{-}30\text{ nm}$  in width and  $20\text{-}50\text{ nm}$  in length while the collagen molecules have diameter of  $1.5\text{ nm}$  and a length of  $300\text{ nm}$  [3].

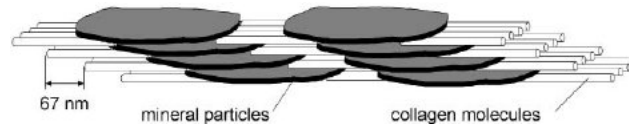


Figure 1.17: Mineralised collagen fibers (from [33]).

► Subnanostructure (smaller than  $100\text{ nm}$ )

As previously explained, the bone is composed of an organic phase, an inorganic phase and water with the proportion stated in TABLE 1.1.

The organic phase is composed of different types of proteins:

- Collagen type I which is the main constituent of this organic matrix as it composes 90% of its weight. Its structure, depicted in FIGURE 1.18 [3, 12], is composed of a series of highly repetitive amino acid sequences i.e. Gly-X-Y forming a polypeptide. Gly represents the glycine, X and Y may vary but most of the time there are proline and hydroxyproline respectively. Three polypeptide chains called  $\alpha$  chains are folded together into a triple-helical structure by hydrogen bonds to form the collagen molecule also called tropocollagen that aggregates to form fibrils of collagen [34, 14]. Covalent cross-links make the fibrils stable and as a result, the collagen molecule is formed [14]. Tropocollagen has a dimension of  $1.5\text{ nm}$  in diameter and  $300\text{ nm}$  in length while the fibrils have a diameter of  $80 - 120\text{ nm}$  [34, 29]. This type of collagen is composed of two different chains which are two  $\alpha 1$  and one  $\alpha 2$  [3, 14, 34].
- Collagen types III and IV differ from collagen type I by the structure of their chain. Indeed, type III collagen is composed of 3  $\alpha 1$  chains while type IV is composed of two  $\alpha 1$ -like and one  $\alpha 2$ -like genes [3, 35, 36]. Collagen type III is present on the surfaces of the Haversian canal and the bone-periosteal junction. It plays a role in the creation of trabecular bone. Research has shown that it can hinder proper bone formation and bring about changes to the remodeling process while fractures are healing [35].
- Proteoglycans and non-collagenous proteins such as osteocalcin, osteonectin and osteopontin [3, 29].

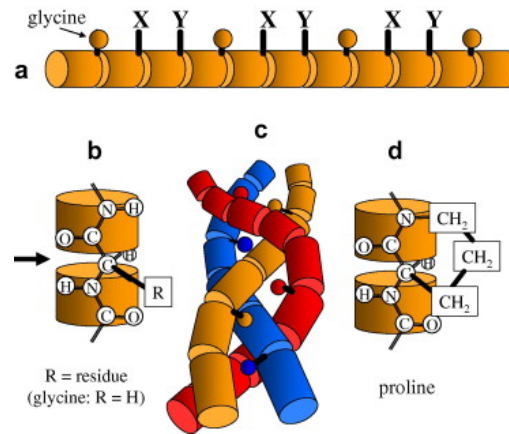


Figure 1.18: Structure of the collagen molecule (a) Amino acid sequence (b) Glycine (c) The triple-helical arrangement (d) Proline and hydroxyproline (Y) (from [14]).

The inorganic phase is composed of mineral crystals called hydroxyapatite  $\text{Ca}_{10}(\text{PO}_4)_6(\text{OH})_2$  which is a form of naturally occurring Calcium phosphate. This crystal contains some impurities including potassium (K), magnesium (Mg), strontium (Sr), sodium (Na) that may bound with the Calcium ion  $\text{Ca}^{2+}$ ; carbonate ( $\text{CO}_3^{2-}$ ) that may interact with the phosphate ion  $\text{PO}_4^{4-}$  and chloride (Cl), fluoride (F) that may link with the hydroxide ion  $\text{OH}^-$  [3]. The crystals are tiny platelets with the following average dimension: 2 – 3 *nm* in thickness, 25 *nm* in width and 50 *nm* in length [28].

Lastly, water is a fundamental constituent, present in various forms within the crystal surfaces, in the interstitial spaces between collagen fibres when minerals are absent, and allegedly within the canaliculi, lacunae, and blood vessels [29]. The presence or absence of water has a significant impact on the mechanical properties of the structure. For example, dehydration leads to a reduction in the distance between collagen molecules, resulting in increased stiffness and strength of collagen. Consequently, the overall toughness of bones decreases.[34]

Bone exhibits remarkable mechanical behaviour due to the contrasting properties of its organic and inorganic phases. The proteins provide elasticity and toughness while minerals provide stiffness to the bone. This combination of properties makes bones strong yet flexible, allowing them to efficiently withstand various forces and impacts [34].

### 1.1.6 Fibrolamellar bone

Fibrolamellar bone is a unique structure commonly found in larger animals that require rapid growth in diameter. It acts as a temporary primary organisation during fast development, providing both strength and support to bear the weight of the growing animal, including handling compression and bending forces [19].

#### ► Structure

Fibrolamellar bone is made of three different structures shown in FIGURE 1.19. It consists of a hypercalcified central (PHL) layer acting as a scaffold for the growth of parallel fibres (PFL). Then lamellar bone (LB) is deposited on top of it and the whole structure surrounds a blood vessel. The change between these structure is gradual, indicating that the boundaries do not possess distinct demarcations but instead meld seamlessly into one another . [37].

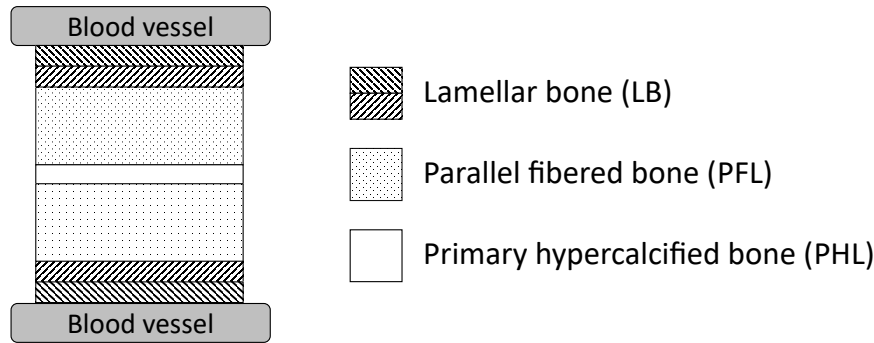


Figure 1.19: Structure of fibrolamellar bone.

In the primary hypercalcified bone (PHL) represented in white in FIGURE 1.19, two distinct features can be found: fibrils and pores [37]. The first feature is organised into arrays, each having a diameter of approximately  $1\text{-}1.5\ \mu\text{m}$  in minipig [37]. Inside each array, the fibrils exhibit a parallel alignment with one another. However, it is important to note that there is no specific preferred orientation of these arrays. Moreover, there is no indication of a  $67\ \text{nm}$  gap between two consecutive fibres along the same line [37]. The individual pore diameters measured in this structure are in the range of several tens of nanometers, consistent with the measurements of individual pore volumes. These pores appear to be devoid of any organic material. Additionally, the presence of canaliculi is relatively limited [37, 38, 39]. In this layer, osteocytes are also present, and while their organisation seems somewhat random, they exhibit a specific alignment, with their primary axis parallel to the orientation of the layer [38]. Based on these observations, it can be inferred that the PHL is expected to demonstrate more or less isotropic material properties [37].

Parallel-fibered bone (PFL) is the primary component of the fibrolamellar unit found in long bones and appears in white with black dots in FIGURE 1.19. This type of bone is char-

acterised by collagen fibrils demonstrating a distinct and consistent preferred orientation, spanning approximately from  $85^\circ$  to  $120^\circ$ , closely aligning with the main axis of the bone [37]. These fibrils are organised into bundles of  $1.5$  to  $3\ \mu\text{m}$ . The bundles closest to the PHL (inner part) possess a distinctive enclosure, unlike those found farther away (outer part), where thin layers separate the bundles [37]. Canaliculi are also located this layer, but they are organised differently depending on whether they are in the inner or outer part. In the inner part, canaliculi are notable for their relatively large diameter, measuring approximately  $200\ \text{nm}$ , and the presence of surrounding collagen fibres slightly flattens their shape. These canaliculi demonstrate an irregular orientation, following complex and twisting pathways [37]. Conversely, in the outer part of the bone, the canaliculi exhibit a more distinct and defined orientation, aligning in straight lines parallel to the collagen fibrils. These canaliculi possess ellipsoidal cross-sections in shape [37]. The difference in canaliculi orientation and osteocytes arrangement serve as reliable markers, revealing changes in bone structure.

Lamellar bone is located alongside the blood vessels and exhibits both thin and thick lamellae as previously stated in SUBSECTION 1.1.5. These lamellae consist of collagen fibres arranged in various orientations. Within a lamella, these fibres can have two different kinds of orientations. The first one is characterised by a change in the favoured direction, spanning from  $10^\circ$  to  $70^\circ$ . The other orientation occurs when the fibres are predominantly oriented at angles  $10^\circ$  and  $90^\circ$ , resulting in distinct plateaus where the collagen fibrils align consistently in the same direction [37]. Additionally, osteocytes and canaliculi are also found in this layer. Osteocytes are meticulously organized and aligned parallel to the lamellae, whereas canaliculi are elongated and mostly oriented perpendicular to the lamellar interfaces [37, 38, 40].

#### ► Mechanical properties

Barrera et al. (2016) conducted a study that centered around testing deer bone samples in three distinct directions: axial, transverse, and radial, using compression as the testing method [41]. The samples were harvested from the proximal diaphysis of the bone and researchers observed that fibrolamellar bones demonstrated the highest Young's modulus when tested in the axial direction. Indeed, the axial direction is the one that needs to withstand the highest loads, as it is aligned with the primary force direction. Following the axial orientation, the transverse direction exhibited the next highest Young's modulus value, indicating its ability to withstand compression forces. Finally, the radial direction showed the lowest Young's modulus among the three orientations. The material behaviour of the bones in this study demonstrated orthotropic characteristics, meaning that their mechanical properties vary with different orientations.

Benecke et al. investigated the relationship between tensile stress and strain in a fibro-lamellar unit obtained from a bovine femur. The range of analysis covered dimensions from  $10\ \mu\text{m}$  to  $1\ \text{mm}$  within the bone sample [42]. The researchers observed that up to the yield point, the strain rate remained uniform throughout the bone. However, beyond this yield point, the strain rate showed significant variation depending on the position within the sam-

ple. In the regions where the bone was damaged, the strain rate increased sharply, indicating higher levels of deformation. On the other hand, in undamaged regions, the strain rate remained relatively constant. The findings suggest that the way bone responds to applied force is not consistent across its entire structure. Instead, how bone reacts to force significantly differs based on factors such as the presence of any damage within the bone and the specific location within the bone structure where the force is being exerted.

In their study, Seto et al. (2008) performed different tests on fibrolamellar bone taken from the periosteal region of a 12 month old calf's femur [43]. Firstly, micromechanical tensile loading was performed in different directions relative to the main collagen fibre axis, ranging from  $0^\circ$  (parallel to it) to  $90^\circ$  (perpendicular to it). The results revealed a substantial anisotropy, meaning that the mechanical properties of the bone varied significantly with different orientations. Indeed, Young's modulus and ultimate tensile strength are approximately 20 and 15 times higher in the sample with an orientation of  $0^\circ$ . In other word, the bone is stiffer when the angle decreases which is illustrated by a higher Young's modulus. This trend was consistent for both wet and dry samples. Then, nanoindentation tests were done and a similar trend was observed. Indeed as the indentation surface increased, the indentation modulus decreased from  $23.1 \pm 0.7$  [GPa] to  $15.4 \pm 0.5$  [GPa].

Limited information is available regarding local-level mechanical properties, as most available data pertains to tissue-level characteristics. Fortunately, a master's thesis authored by Pauline specifically focuses on fibrolamellar bone [44]. In her research, she discovered that thick lamellae exhibit the highest storage modulus, followed by parallel fibers bone. The hypercalcified layer ranks third, while thin lamellae come in fourth. The specific values of these storage moduli can be referenced in TABLE 1.1. Additionally, she calculated the thickness of the lamellae and determined that thick lamellae range in size from 2.79 to 4.65  $\mu\text{m}$ , while thin lamellae exhibit a size varying from 1.39 to 2.6  $\mu\text{m}$ .

	Storage modulus [GPa]
Thick lamellae	$46.46 \pm 3.56$
Thin lamellae	$32.8 \pm 4.17$
Parallel fibers bone	$42.65 \pm 3.93$
Central layer	$38.11 \pm 1.89$

Table 1.1: Young's modulus in the different layer in the fibrolamellar bone (from [44]).



## 1.2 Scanning electron microscopy

Scanning electron microscopy (SEM) is an imagery technique that uses electrons to image bone and bone cells with a resolution in the range of  $1\ \mu m$  to  $1\ nm$ . Indeed, this approach facilitates the examination of surface characteristics such as topography, crystalline structure, chemical composition, and electrical properties within the uppermost layer of approximately  $1\ \mu m$  of the sample. The resolution depends on the type of microscope and the signal. It works by generating an accelerated electron beam onto the sample which generates a high-quality image. SEM offers several advantages over optical microscopy such as a large depth of field, higher magnification and a wide range of information other than just surface topography as previously stated [45].

The FIGURE 1.20 illustrates the main components of the SEM:

- **Electron gun:** It is the source to generate electrons with high energy ( $2 - 1000\ kV$ , wavelength of  $0.027 - 0.009\ nm$ ). There are three main different types of electron gun which are the tungsten hairpin filament heated, lanthanum hexaboride  $LaB_6$  filaments and field emission gun. The first type is the most common one and works by thermionic emission, i.e. the filament is heated until it reaches a certain threshold, after which electrons escape the material. The second type of gun also works by thermionic emission with the difference that it emits a brighter beam. The last gun works by field emitters, as the name suggests, and require no heat. Instead, a high electric field is applied causing a minimal deviation in electron energy and resulting in a brighter beam [45, 46].
- **Condenser lens:** The beam converges and focuses on the aperture allowing for control over the beam diameter [47].
- **Objective lens:** It is responsible for focusing the beam directly onto the specimen after passing through the aperture. [46, 47].
- **Scan coils:** It is the deflection system responsible for scanning the designated zone and deflecting the beam in a zigzag pattern above the sample [46, 48].
- **Detector:** It detects the signal emitted from the surface of the sample. There are different kinds of detectors according to the type of signal [48].

Electrons have the ability to penetrate the specimen, forming a teardrop-shaped volume whose dimensions are determined by various factors including the energy of the electron beam, the atomic masses of elements present in the specimen, and the angle at which the electron beam interacts with the specimen. The term "penetration depth" refers to the distance that electrons can travel into the specimen before being significantly scattered or absorbed. It increases when the electron beam possesses higher energy, and has a large angle of incidence and low atomic mass [45].

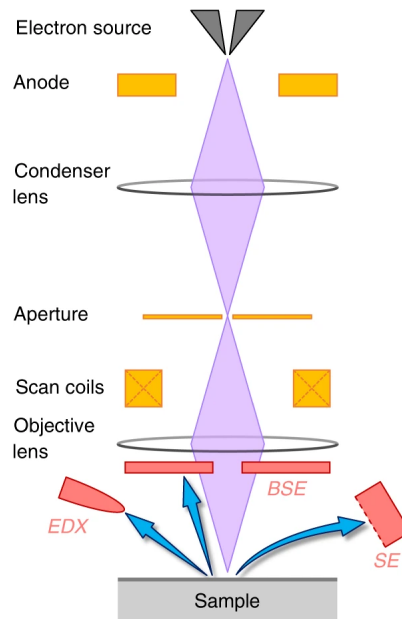


Figure 1.20: Schematic of the scanning electron microscopy (from [49]).

The specimen can be either thin or thick. For thin samples, the electrons pass through it without being significantly absorbed and are viewed using transmission electron microscopy (TEM). On the other hand, if the sample is thick, the electrons no longer pass through the sample. As a consequence, only particles emitted or scattered from the surface can provide information. These particles illustrated in FIGURE 1.21, are created by the interaction between the electron beam and the specimen. These signals are the following: secondary, backscattered and Auger electrons, X-rays and cathodoluminescence (emission of light). After the signal is detected by the detector, it is fed to a monitor. The monitor's rastering process ensures that the image displayed on the screen aligns with the scanning pattern of the electron beam. Finally, the magnification is determined by comparing the size of the raster on the specimen to the size of the display on the monitor [45, 46].

In this master thesis, thick samples are measured with backscattered electrons (BSE), i.e. incident electrons reflected back by the nuclei within the atoms of the sample as depicted in FIGURE 1.22. They possess a high energy with a good resolution despite their low abundance. The deviation of electrons is impacted by the atomic number ( $Z$ ) of the atom present on the surface of the sample [45]. Specifically, a specimen containing a heavier element with a higher  $Z$  exhibits more efficient backscattering than lighter elements as it re-emits more electrons. Consequently, these heavier elements appear brighter in the BSE image providing a contrast that indicates the composition of the sample [45, 49].

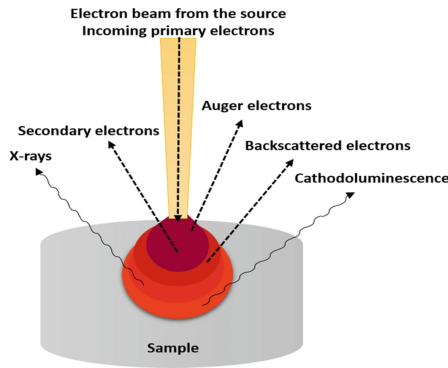


Figure 1.21: Signal emitted from the sample (from [46]).

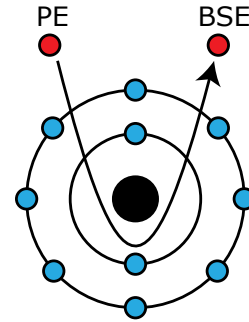


Figure 1.22: Generation of backscattered electrons (BSE) (adapted from [50]).

### 1.3 Nanoindentation

Nanoindentation is a method employed to assess the mechanical properties, specifically the Young's modulus and the hardness of materials with nanoscale resolution. The technique consists in applying a defined load on a sample using a diamond tip and measuring the resulting displacement, as depicted in FIGURE 1.23. Throughout the process, the depth of the probe and the applied load is continuously measured, allowing the generation of a load-depth curve, as illustrated in FIGURE 1.24. This curve provides valuable insights into the material's mechanical characteristics [51, 52].

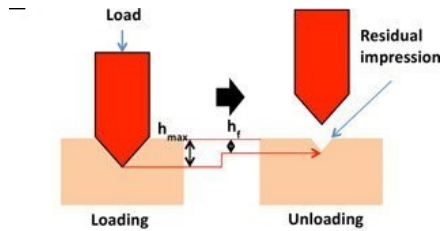


Figure 1.23: Schematic of the indenter that penetrates the sample (adapted from [53]).

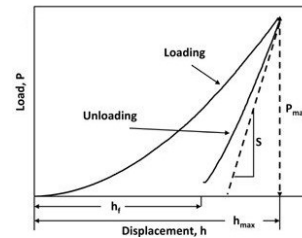


Figure 1.24: Load-depth curve (adapted from [53]).

Olivier-Pharr proposes a model to extract the hardness ( $H$ ) and reduced modulus ( $E_r$ ) from the load-depth curve. The hardness is obtained by dividing the peak indentation load ( $P_{max}$ ) by the projected area at the corresponding contact depth  $h_c$  ( $A$ ) as depicted by EQUATION 1.3 [54, 55]. Their model is based on Sneddon's analysis of elastic contact by a rigid and axisymmetric indenter [51]. They propose the EQUATION 1.4 known as the fundamental equation of nanoindentation [51, 52]:

$$H = \frac{P_{max}}{A} \quad (1.3)$$

$$S = 2E_r a = \frac{2}{\sqrt{\pi}} E_r \sqrt{A} \quad (1.4)$$

$S$  is the stiffness, i.e. the slope of the load-depth curve and is derived from  $E_r$  and  $a$  or from  $E_r$  and  $A$ , where  $E_r$  is the effective modulus depending on the material,  $a$  is the contact radius and  $A$  is the contact area.

When conducting nanoindentation experiments, it is crucial to observe several precautions, particularly concerning the penetration depth and indent spacing. The following points should be considered:

- Penetration depth: The surface roughness of the sample should be minimised as much as possible. A smoother surface ensures more accurate and reliable measurements. To ensure that the roughness will not impact the results, it is advisable to limit the maximum indentation depth to approximately 10 times the roughness of the sample surface, as recommended by previous studies [56, 57].
- Indent spacing: During the indentation process, inelastic deformation occurs, leading to a larger affected area than the visible mark on the surface, known as the influence area. Ensuring accurate and independent measurements for each indent requires preventing the overlap of influence areas. To achieve this, maintaining a gap between indents, at least three times the contact radius of the tip as suggested in prior research [58], is recommended. This spacing helps prevent interference between adjacent indentations and ensures reliable results during the testing process.

By adhering to these precautions, researchers can obtain more reliable and meaningful results from nanoindentation experiments while minimising potential distortions caused by surface roughness and influence area effects. These considerations are vital for obtaining accurate mechanical property data at the nanoscale.

## 1.4 Main aim of This Thesis

The fibrolamellar bone structure is a prevalent feature within the animal kingdom, often associated with rapid growth in larger organisms. Despite this, investigations into its mechanical properties have been limited. A comprehensive understanding of the contributions of each substructure within fibrolamellar bone to material properties necessitates a nano-scale study. Fortunately, a novel methodology has emerged, introduced here for the first time to bone tissue, previously utilised on biomaterials such as stomatopods [59]. This novel approach offers the potential to establish a direct connection between structure and function at the nanometre level, revealing promising avenues. Moreover, our research is driven by the motivation to investigate the effects of surface roughness and calibration methods in a unique context, considering their pioneering application to bone tissue. This investigation not only illuminates the mechanical attributes of fibrolamellar bone but also pioneers the application

of state-of-the-art techniques in bone analysis, rendering it an appealing prospect for a master's thesis.

The aims of this thesis are twofold:

- The main goal of this research is to dive into the world of fibrolamellar bone and understand its mechanical behaviour better. In particular, we seek to examine the stress-strain curves of fibrolamellar bone, with a keen focus on the lamellar region. Certainly, within the scope of this thesis, a substantial amount of data is gathered at the local level, diverging from the prevailing focus of current studies primarily centred on tissue-level analysis. By doing so, we aim to obtain a better understanding of the structure-function relationship of fibrolamellar bone by analysing the correlation between the local mechanical properties with their underlying structure.
- The second goal is to explore the influence of the surface roughness and the calibration method on the measurements. Through this investigation, we aim to enhance the precision of our results, facilitating a more comprehensive comprehension of the mechanical properties of the bone.

# Chapter 2

## Methodology

The purpose of this chapter is to provide a detailed description of the experimental procedures undertaken in this project. The first section is dedicated to the sample preparation. Subsequently, the second section is dedicated to the nanoindenter and elucidates the process of obtaining stress-strain behaviour of biological materials. Finally, the use of scanning electron microscopy is briefly explained in the last part.

### 2.1 Sample preparation

The samples used for this thesis were prepared by Astrid Cantamessa and the protocol employed to prepare them is explained below and summarised in FIGURE 2.1. This protocol is the one currently followed by the Ludwig Boltzmann Institute of Osteology in Vienna which has been established for several years and has proven effective since [60]-[63].

The initial step involves sample collection. One femur of calf whose age was unknown was harvested from a butcher. To prevent the formation of micro-cracks occurring when stored in the freezer, the cutting process was performed on the same day.

The long bone was first cut into several transverse sections of the diaphysis of the femur and then refined into 2 cm cubes using a band saw. Subsequently, a low-speed diamond saw was employed to further reduce the cubes size to 1 cm.

Next, the samples underwent a dehydration process in graded ethanol and acetone series for 11 days. It is important to note that this dehydration process can impact the mechanical properties of the bone, making it more rigid, as commonly observed.

Finally, the samples were embedded in poly-methyl methacrylate (PMMA), composed of 400 ml of MMA, 7 g of Benzoylperoxide (BPO), and 100 ml of Nonylphenylpolyethyleneglycol acetate in a total volume of 500 millilitres (ml).

Subsequently, the samples underwent grinding and polishing. Initially, a diamond saw was used to cut the top of the sample in order to remove the part that did not cure properly and it also frees the surface of the resin. This freed section was subsequently polished and subjected to analysis. The grinding process involved two stages using carbide paper (P1500 and P2500) with decreasing grains size. Both grinding stages lasted for 3 minutes at a speed of 20 rpm, under ethylene glycol irrigation. After grinding, two polishing steps were carried out with diamond suspension of 3  $\mu m$  and 1  $\mu m$ . The first polishing stage lasted for six minutes at 45 rpm, while the second stage lasted for seven minutes at 35 rpm. To ensure a consistent and uniform polishing effect, a force of 10  $N$  was applied to the sample.

As the nanoindentation technique concerned in this study is really sensitive, requiring indents at small depths, further surface polishing was performed by Astrid Cantamessa and Dr. Shahrouz Amini at Max Planck Institute of Colloids and interfaces in Potsdam. Two methods were tested: ion sectioning and ion polishing. The first method is a technique used to polish or thin a sample in a controlled and refined manner. A broad ion beam is directed at the sample surface, and the ions cause sputtering, removing material from the surface [64]. However, this process resulted in extremely refined samples, making it impossible to locate the various sub-regions of fibrolamellar units with an optical microscope. Therefore, the second method, ion polishing, was employed to address this limitation. Indeed, this technique is used to enhance the surface quality of the sample, by efficiently removing surface damage and irregularities [65]. This technique proves to be the optimal choice for our specific application, as it strikes a balance between achieving the lowest roughness possible while retaining the ability to discern intricate microscopic features within each sub-region of fibrolamellar bone.

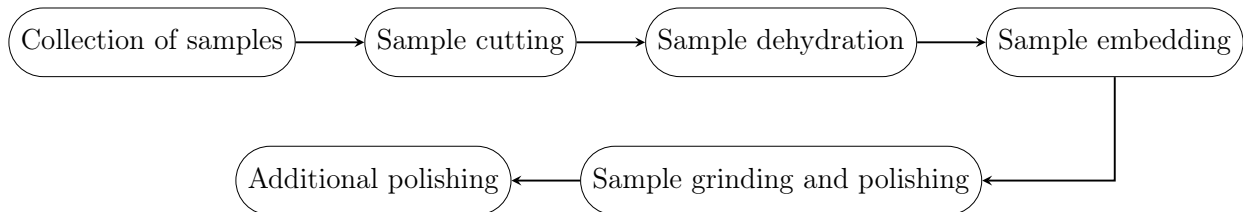


Figure 2.1: Process of the sample preparation.

A total of two different samples were utilised in the study. Despite both samples undergoing the same polishing process, the second sample exhibited superior polishing results.

## 2.2 Nanoindenter

The nanoindenter used is the Triboindenter TI 950, Bruker, US. A conospherical diamond probe (5  $\mu m$  tip radius) was used to perform the calibration and the cyclic indents enabling to obtain the stress-strain behaviour.

### 2.2.1 System

The system is a highly advanced and precise instrument used for material characterisation, specifically for nanoindentation and scanning probe microscopy (SPM) imaging. It consists of various interconnected components, each serving a specific purpose in achieving accurate and reliable results which can be seen in FIGURE 2.2.

- **Sample stage:** The sample is placed on this stage which is automated with X, Y, and Z axis control. The platform is magnetic allowing the sample to be stabilised as a magnetic disk is glued under the specimen. Additionally, the magnetic disk is glued onto the stage to ensure that vibrations do not move the sample.
- **Granite frame:** It is a stable frame that provides thermal stability, reduces environmental noise, and suppress the resonant frequencies.
- **Piezo scanner:** It is mounted on the granite frame and allows precise positioning of the tip very close to the sample, ensuring accurate measurements during nanoindentation and SPM imaging.
- **Transducer:** It is mounted on the piezo scanner and serves the purpose of measuring the displacement of the tip during experiments.
- **Optical microscope:** It allows to view the sample and with a magnification capability of the sample allowing users to view the sample at different magnifications which are in the order of  $\mu m$ .

To further enhance the instrument's performance and accuracy, it is housed within an acoustic enclosure. This enclosure reduces the influence of unwanted air currents, ensuring a controlled environment for accurate measurements in a noise-sensitive setting.

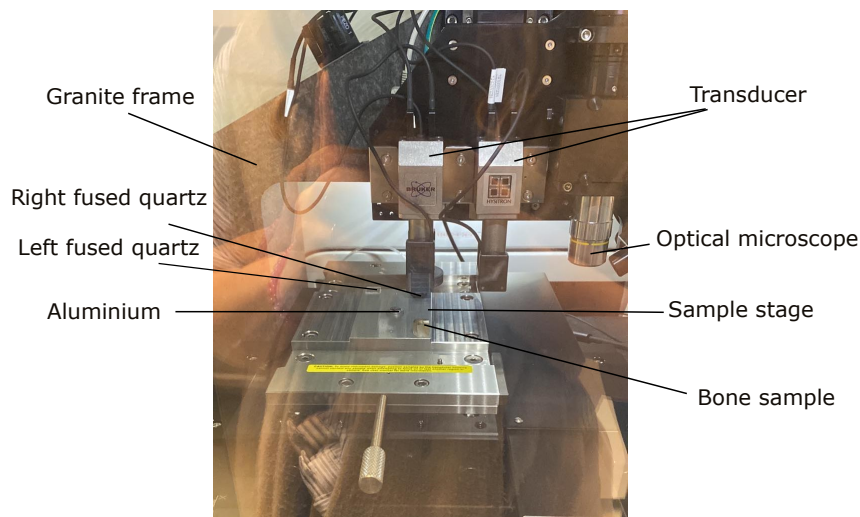


Figure 2.2: Illustration of the Triboindenter TI 950, Bruker, US.



### 2.2.2 Scanning probe microscopy

In this thesis SPM is the abbreviation of the scanning probe microscopy. In order to get appropriate SPM images, one needs to adjust the following parameters.

- **Scan rate (Hz):** The value varies depending on the level of clarity that we wish to achieve. A low value results in a scan that takes more time and therefore leads to a better image resolution.
- **Scan size ( $\mu\text{N}$ ):** It represents the window of the sample that is scanned. This value changes according to the use.
- **Scan resolution:** This is the number of pixels used to produce the image which is 256 by default and this value does not change throughout this these.
- **Scan orientation:** As the name said, it is the way the probe performs the scan which is horizontal by default and does not change throughout this thesis.
- **Setpoint ( $\mu\text{N}$ ):** This value was set at 2  $\mu\text{N}$  and represents the force which is applied when the probe is in contact with the sample. Again, this value stay the same throughout the use of the nanoindenter.
- **Integral gain:** This value was set at 240 and never change throughout the different SPM.

When the appropriate parameters are selected, the user has the option to generate two types of images: topographical or gradient. In this thesis, the topographical images are predominantly favoured due to their ability to provide precise representations of various lamellae. It involves mapping the three-dimensional surface structure of a sample, revealing variations in height or depth. As a result, the images showcase a colour gradient, with darker shades indicating lower elevations and lighter shades representing higher elevations. Gradient images are used to reveal variations in specific properties across a surface. This involves scanning a probe or sensor over the sample while measuring the property of interest, in this case the difference in elevation. The resulting data points are then used to create a visual representation. Analysing these images can be more challenging since their visual interpretation is not straightforward.

### 2.2.3 Calibration of the transducer

Before starting any measurement, the first step is to calibrate the transducer which involves what is called "Indentation Axis calibration". During this step, the nanoindentation probe conducts an air indent with specifications preconfigured within the machine system, requiring no adjustments from the user. Indeed, a triangular load function is employed, exerting a peak load of 1300  $N$ , resulting in the probe's displacement falling between 3.5-4.5  $\mu\text{m}$  within the air. Should the displacement exceed this range, force adjustments are made to ensure the desired displacement range is attained. Following the calibration, a graph is generated

which is compared with a fitted linear plot, and the Root Mean Square Error (RMSE) value, indicating the difference between the two, is calculated. For the calibration to be considered successful, the RMSE value must be in the order of  $10^{-5}$  and  $10^{-6}$ .

### 2.2.4 Cleaning of the tip

The subsequent calibration step involves a thorough cleaning of the tip to eliminate any debris or particles that could potentially be present on its surface. To achieve this, 1 indent is made in an aluminium sample using a basic QS trapezoid load function is employed with a peak load of  $10000 \mu N$  as illustrated in FIGURE 2.3. This specific load function, with its relatively high peak load, ensures that the tip can penetrate the surface of the aluminium sufficiently to remove any dirt or debris which guarantees an effective cleaning and ensures that the tip is free from contaminants.

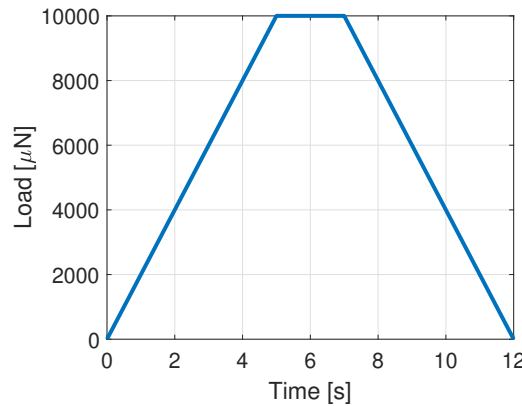


Figure 2.3: Load function used for the cleaning of the tip.

### 2.2.5 Tip calibration

In order to have accurate measurements, the tip must be calibrated after its cleaning. This step is crucial and needs to be performed several times to ensure accuracy and reproducibility of the results as the nanoindenter is very sensitive. It is performed on fused quartz as this material is considered perfect with no impurity.

In the study of stress and strain dynamics, a fundamental requirement is to determine the contact radius. This radius is intricately influenced by the depth of penetration, which is quantified using nanoscale measurements. To comprehensively explore the relationship between contact radius and penetration, a systematic investigation was undertaken, encompassing various series of indentation tests. In each indentation, a consistent load function was applied, with the load varying. The load function is a basic QS Trapezoid and can be seen in FIGURE 2.4. This approach facilitated an exploration of a wide spectrum of forces, resulting in an array of displacements. These experiments were conducted on fused quartz, utilising

its established modulus ( $E_r$ ) which is about 69.5 [GPa]. The stiffness ( $S$ ) and measurements penetration depth ( $h_c$ ) obtained during each indentation to deduce the contact area ( $A$ ). From the contact area, one can also deduce the contact radius ( $a$ ). The equation establishing the relationship between these variables are given in EQUATION 2.2 and 2.1.

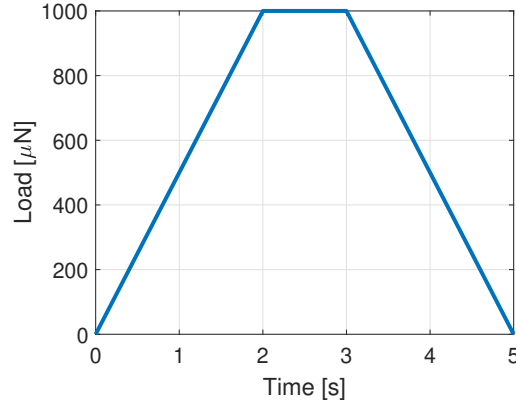


Figure 2.4: Load function used for calibration.

$$A = \frac{\pi S^2}{4 E_r} \quad (2.1)$$

Formula for the contact area

$$a = \sqrt{\frac{A}{\pi}} \quad (2.2)$$

Formula for the contact radius

Once the contact radius ( $a$ ) is computed, one can link it with the experimental point of the penetration depth ( $h_c$ ) using the following fitting equations (EQUATION 2.3 to 2.5):

$$a = C_0 \times h_c^{C_1} \quad (2.3) \quad a = C_0 \times (1 + h_c)^{C_1} \quad (2.4) \quad a = C_0 \times (C_1 + h_c)^{C_2} \quad (2.5)$$

In practice, the following steps were executed:

### ➤ Scanning procedure

First, a scanning procedure is conducted on the fused quartz to inspect the surface and identify any potential dirt or contaminants. The scanning zone has a size of 50  $\mu m$ . The purpose of this scanning step is to assess the surface roughness and ensure that the Root Mean Square (RMS) value, computed using EQUATION 2.6, is kept low. RMS is a measure of the variability of the roughness and maintaining a low value is essential for achieving a more accurate calibration of the nanoindenter. TABLE 2.1 provides information about the different roughness values observed in different zones of the sample. Once the scanning procedure is completed, the indentation process can be carried out. This step is a

$$RMS = \sqrt{\frac{1}{N} \sum_{i=0}^N (x_i - u)^2} \quad (2.6)$$

RMS formula from [66] with  $N$  = the number of data points,  $x$  the specific value of the point  $i$  and  $u$  the mean average of the region of interest.

crucial part of the calibration process and is essential for achieving reliable and precise measurements during subsequent nanoindentation experiments.

	CAL 0	CAL 1	CAL 2	CAL 3	CAL 4	CAL 5
Roughness	13.153	6.6685	6.4670	6.9617	6.2111	6.7966

Table 2.1: Roughness of the fused quartz on a window of 50  $\mu m$ .

### ➤ Indentation grids

Afterwards, indentation grids were performed to determine the appropriate coefficients. Different parameters were tested to obtain a dataset allowing a good fitting. The first one consists of static indents. These methods are described in this section and the load functions can be seen in Figure 2.4. In fact, all the load functions have the same form which is basic QS Trapezoid. The probe penetrates the fused quartz with increasing load for 2 seconds. Then it stays at the same place for 1 second at the desired peak load. Finally, the probe removes itself with decreasing load for 2 seconds. As a result, one indent takes 5 seconds to be made. The difference between the methods resides in the variation of the peak loads. All the important parameters are summarised in TABLE 2.2.

- (i) The first method used consists of static indents with a peak load that starts at 1000  $\mu N$  and finishes at 10  $\mu N$  with an increment of -15.7143. In total, 64 indents performed arranged in a grid of 8 by 8 with a spacing of 6  $\mu m$ . The indents are arranged in a serpentine pattern to minimise errors that may arise due to extensive movement of the transducer. This method was done in four different regions.
- (ii) The second method used also consists of static indents with a peak load that starts at 10000  $\mu N$  and finishes at 10  $\mu N$ . In total, 100 indents performed arranged in a grid of 10 by 10 with a spacing of 6  $\mu m$ . The indents are also arranged in a serpentine pattern for the same reason as previously stated. This method was performed in three different zones.
- (iii) The last method consists of using two different grids on two different regions. The first region undergoes a peak force that starts at 500  $\mu N$  and finishes at 10  $\mu N$ . The second region undergoes a peak load that starts at 1500  $\mu N$  and finishes at 500  $\mu N$ . The number of indents is the same as the first method as well as the spacing and the serpentine patterns.

	First method	Second method	Third method
Number of zone	4	3	2
Start load	1000 $\mu N$	10000 $\mu N$	500 $\mu N$ and 1500 $\mu N$
End load	10 $\mu N$	10 $\mu N$	10 $\mu N$ and 500 $\mu N$
Number of indent	64 (8X8)	100 (10X10)	64 (8X8)
Spacing	6 $\mu m$	6 $\mu m$	6 $\mu m$
Name	CAL 0, CAL 1, CAL 2 and CAL 3	CAL 4, CAL 5 and CAL 6	CAL 7 and CAL 8

Table 2.2: Important parameters to perform the calibration.

### ➤ Choosing the right data-set

When all the tests are done, one can compute the relevant information with the following method:

The coefficients  $C_0$ ,  $C_1$ , and  $C_2$  of EQUATION 2.3 to 2.5 are determined through the curve fitting functionality provided by MATLAB. Subsequently, the fitting equation is calculated based on the experimental data points, as depicted in FIGURE 2.5. It is worth noting that an additional data-set called "Postdam" has been included in these figures. These data-sets were acquired by Cantamessa A. and serve as a reference for performing the calibration accurately. By comparing the fitting equation and experimental data with the "Postdam" data-set, one can validate and ensure that the calibration process is being carried out correctly.

When looking at the graph, one can remove the use of coefficients from CAL 4, CAL 5 and CAL 6 as they are best used for high penetration which means for higher loads which is not the purpose of this thesis. Indeed, the stress-strain curves are obtained using low loads, necessitating a focus on obtaining a majority number of experimental points at low penetration depths. Afterwards, one can also remove CAL 2 and CAL 3 as their pattern differ a lot from the other ones. This can be explained by the fact that there was a lot of noise and vibration in the room next to the nanoindenter as well as someone left the door open which influences the result. Moreover, CAL 3 was removed as it was done on an old fused quartz which gave weird results. Finally, CAL 0 was removed as it is not close to the result obtained at Postdam. As a result, CAL 7 and CAL 8 were selected, further supported by their numerous experimental data points at low loads. These datasets are combined to get the coefficient and FIGURE 2.6 was obtained.

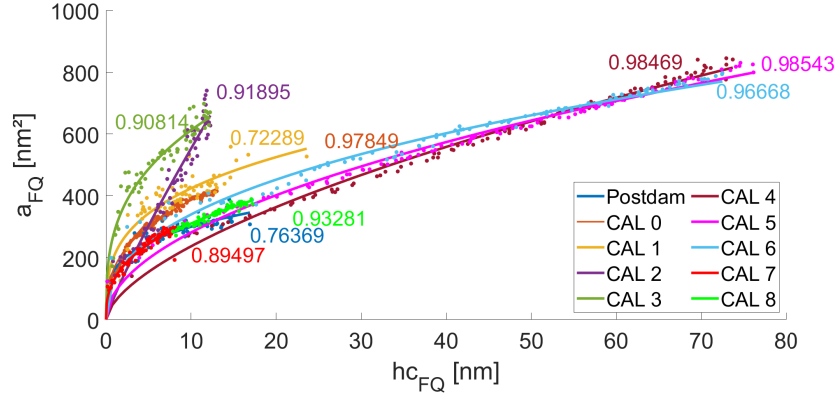
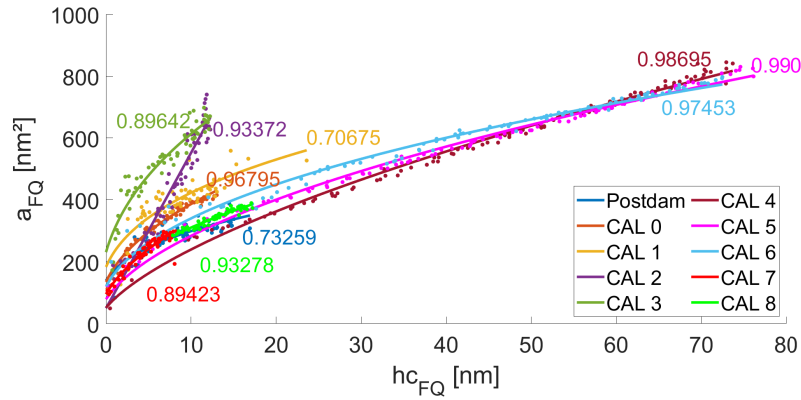
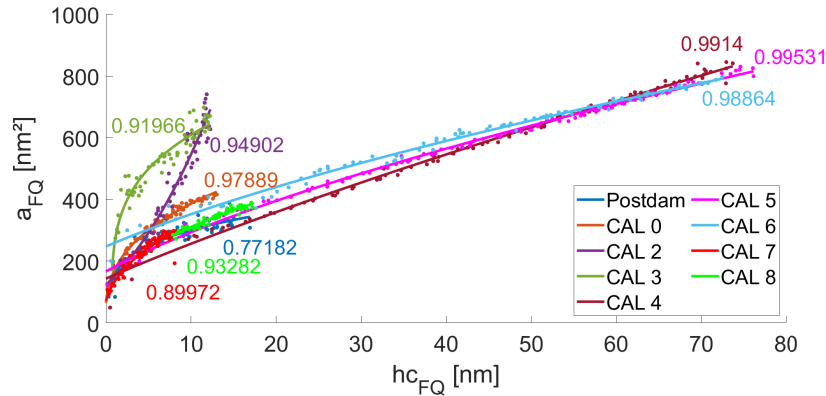
(a) First fitting ( $a = C_0 * h_c^{C_1}$ ).(b) Second fitting ( $a = C_0 * (1 + h_c)^{C_1}$ ).(c) Third fitting ( $a = C_0 * (C_1 + h_c)^{C_2}$ ).

Figure 2.5: Calibration using all the fitting equations. The bullet represents the experimental point and the line is the fitting. The value next to each line is the R-squared value of the fitting.

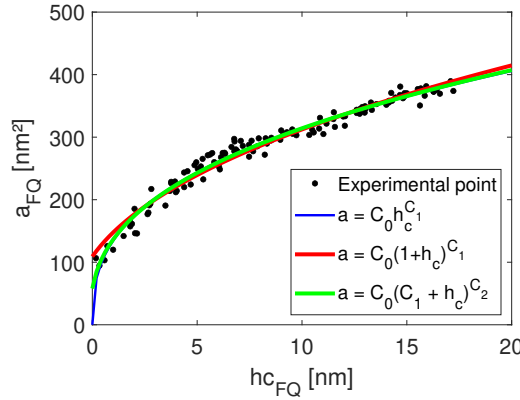


Figure 2.6: Final Calibration with all the fitting equations.

### ➤ Fitting choice

Now that we have the right data set for the computation of the coefficients, the last step is to choose the appropriate fitting equation from EQUATIONS 2.3 to 2.5. As the curves look quite the same in FIGURE 2.6, the right fitting equation was chosen on the basis of the results on bone. This is discussed in the SECTION 2.2.10

### ➤ Stress-strain analysis

Having established the correlation between contact radius and displacement, we can now elucidate the method for deriving stress and strain based on this relationship, which is discussed in the next subsection.

## 2.2.6 Sample measurement

Once the calibration steps are completed, the nanoindentation tests can be initiated. The process starts with an indentation axis calibration, followed by a cleaning step on the aluminium sample, as explained in previous sections.

After these preparatory steps, a new SPM is performed on the surface of the sample to evaluate the roughness and analyse its influence on the results as well as to ensure that lamellae are visible. The sizing and positioning of the scanning zone are established based on particular goals, such as visualising lamellae or analysing specific structures like parallel fibered bone (PFL).

Once the zone is defined, the actual testing phase begins and the indentation can be performed. The indentation process involves pressing the nanoindenter's tip onto the selected zone with controlled force, measuring the resulting displacement and recording the data for analysis. The choice of scan zone and indentation parameters is crucial, as it determines the

accuracy and relevance of the obtained data. The test was performed on both fibrolamellar bone (11 zones) and fused quartz (1 zone) by using a cyclic load as seen in FIGURE 2.7. This cyclic load performs 20 indents with an increasing load which starts at  $5 \mu N$  and ends at  $200 \mu N$ . The first three indents at low load ( $5 \mu N$ ) are performed to ensure the reproducibility of the results and the absence of drifts. This function was created and optimised by Dr. Amini and Cantamessa A. in order to be able to reach the yield point in the stress-strain curves.

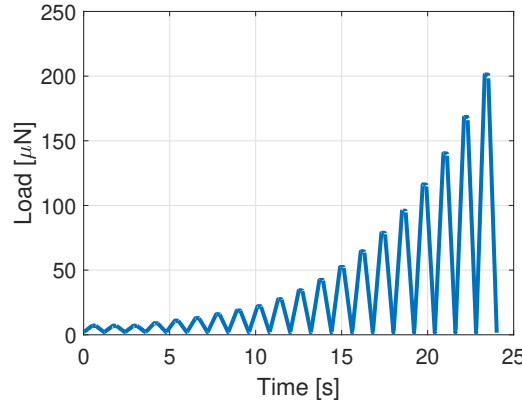


Figure 2.7: Cyclic load used on fibrolamellar bone and fused quartz.

When all the indents are performed, the stress-strain curves can be generated using the following procedure:

First of all, we obtain the load  $P_t$  and penetration  $h_c$  from the nanoindenter. Then, one can compute the contact radius ( $a$ ) from either the fitting EQUATION 2.3, 2.4 or 2.5. With this information, the tip radius  $R$  can be computed with EQUATION 2.7. Lastly, one can compute the stress  $\sigma$  and strain  $\epsilon$  with the EQUATION 2.8 and 2.9 respectively. Then to get the stress-strain curves, one can plot the stress as a function of the strain.

$$R = \frac{a^2}{2h_c} + \frac{h_c}{2} \quad (2.7)$$

$$\sigma = \frac{P_t}{\pi a^2} \quad (2.8)$$

$$\epsilon = \frac{a}{R} \quad (2.9)$$

The final step of the nanoindentation test involves restarting the process, and there are two possible scenarios for starting this step. The first one is to start at the indentation axis calibration step. If the previous indentation test took a considerable amount of time or was performed during the night, the nanoindenter might not have been in use for an extended period. In this case, it is recommended beginning by performing the indentation axis calibration again. This ensures that the instrument's positioning and alignment are accurate and reliable before proceeding with further tests. The second scenario is to start at the step concerning the cleaning of the tip in aluminium. Indeed, if the nanoindenter was not left unattended for a significant period, and the calibration and alignment are still



considered reliable, one can proceed with the test directly after cleaning the tip in aluminium. This scenario is suitable when the nanoindenter has been in use more frequently and recently.

### 2.2.7 Static indent

Some static indents were also performed for two different reasons.

- The first one is to get the Young modulus of the lamellae. For this purpose, the load function illustrated in FIGURE 2.8 was used. This function is called Basic QS Trapezoid Bone and has a peak load of  $500 \mu N$ . It has the same shape as the one used to calibrate. The difference relies on the time it takes to perform one indent (40 seconds here) and on the peak load.
- The second one is to create some boundaries around the indentation areas in order to located them using the SEM. In order to create them the load function basic QS Trapezoid used for the calibration was used with a peak load of  $10000 \mu N$ .

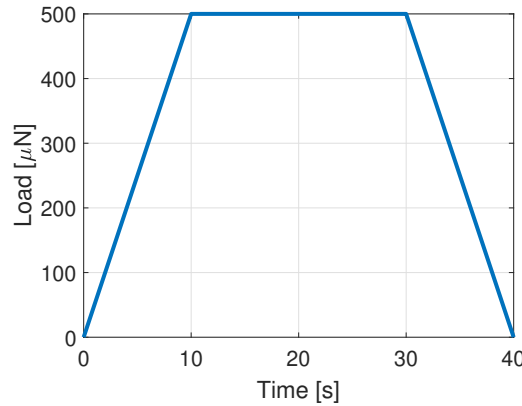


Figure 2.8: Static load used on fibrolamellar bone.

### 2.2.8 Summary of the protocol

As described, performing the nanoindentation test is a complex process that requires a strict and well-established protocol to ensure the relevance and accuracy of the data obtained. The steps involved in this protocol have been carefully developed and validated through numerous tests, particularly on fused quartz. This protocol has been summarised in FIGURE 2.9.

Firstly, it is essential to calibrate the nanoindenter. This involves calibrating the transducer and then cleaning the tip on aluminium before proceeding to calibrate it. This meticulous process ensures accurate calibration for precise measurements.

After this calibration process, one can finally perform the nanoindentation test which consists of the calibration of the transducer then a cleaning of the tip. After this, the sample measurement can be made. When the measurements are finished the user can choose to perform static indents to create boundaries around the indentation area or not. Then one can restart the process at the cleaning of the tip or at the calibration of the transducer if needed.

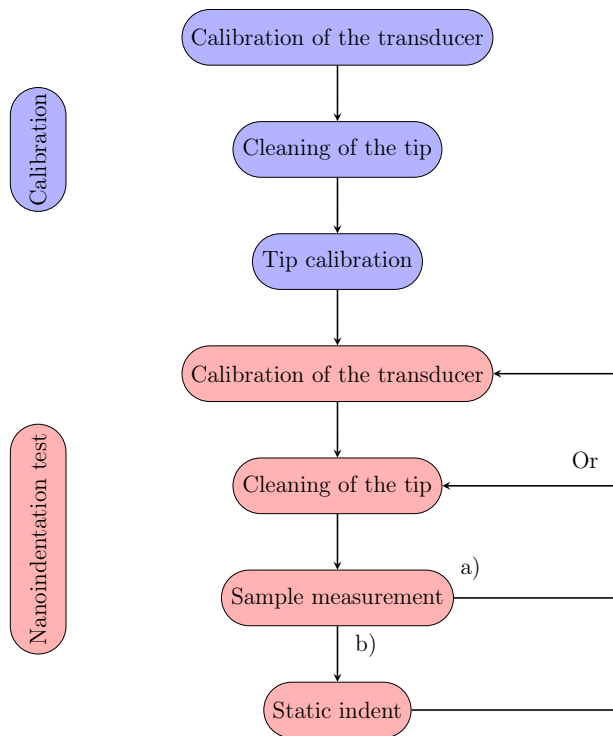


Figure 2.9: Summary of the various steps in the established protocol

### 2.2.9 Impact of the roughness.

Other load functions were used in order to flatten the roughness before performing the measurements on the sample. These load functions are represented in FIGURE 2.10 which are cyclic and composed of 5 indents each. The difference between them resides in the load. Indeed, all of them start at  $5 \mu N$  and they end at  $10 \mu N$ ,  $30 \mu N$  and  $50 \mu N$ . These load functions are used prior to the main cyclic load function.

Something to keep in mind is that the nanoindenter is very sensible, especially at low load. The consequence is that even if we encode a low load value, the value that is applied differs a bit as observed in the graph of the load function. Indeed, they all start at  $7 \mu N$  and not  $5 \mu N$ .

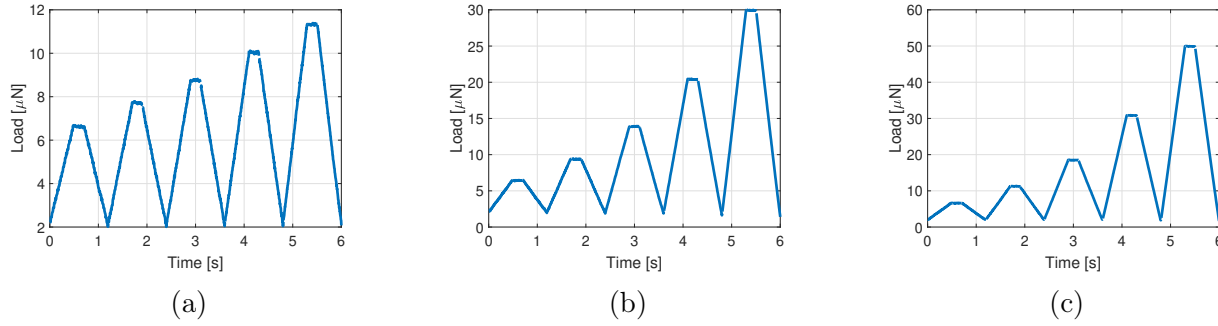


Figure 2.10: Cyclic load to flatten the roughness. a) Load that varies from 5  $\mu N$  to 10  $\mu N$ , b) Load that varies from 5  $\mu N$  to 30  $\mu N$  and c) Load that varies from 5  $\mu N$  to 50  $\mu N$ .

### 2.2.10 Impact of the fitting equation

As previously discussed in SECTION 2.2.5, there are three fitting equations available for determining the contact radius (a). For the sake of clarity, these equations are restated below:

$$a = C_0 \times h_c^{C_1} \quad (2.10) \quad a = C_0 \times (1 + h_c)^{C_1} \quad (2.11) \quad a = C_0 \times (C_1 + h_c)^{C_2} \quad (2.12)$$

These equations provide valuable insights into calculating the contact radius and have a great impact on the stress-strain curves, as depicted in FIGURE 2.11. These curves represent data obtained from fibrolamellar bone, within a 20  $\mu m$  window. Although a total of 25 indents were performed in the region, this section focus on presenting the results of 4 indents, while the remaining ones are observed and discussed in greater detail in section 3 and 4 respectively. FIGURE 2.11a was obtained using no other cyclic load function to flatten the roughness while the FIGURE 2.11b to 2.11d used one with a load that varies from 5  $\mu N$  to 10, 30 and 50  $\mu N$  respectively.

The impact of the fitting equations on the stress-strain curve is evident, particularly at low loads when the strain is below 2%. At higher loads, the behaviour of the curves remains consistent. Therefore, selecting an appropriate fitting equation involves examining the curve below the 2% strain threshold. Usually, obtaining a low strain value requires applying low stress, which is not the case for the first and third fitting equations (EQUATION 2.10 and 2.12). These equations lead to curves that start at around 0.3 GPa, which is not ideal. On the other hand, the second fitting equation (EQUATION 2.11) presents a more suitable curve as it starts with a stress of approximately 0.15 GPa. The higher stress value might initially appear to be influenced by the roughness of the sample, but experimental evidence reveals that even when a cyclic load is applied to flatten the roughness, the high stress value persists as shown in FIGURE 2.11b to 2.11d. Consequently, EQUATION 2.11 was chosen for computing the stress-strain curves, and all subsequent stress-strain curves are generated using this fitting equation. This choice ensures that the curves accurately represent the behaviour of the material at low strains.

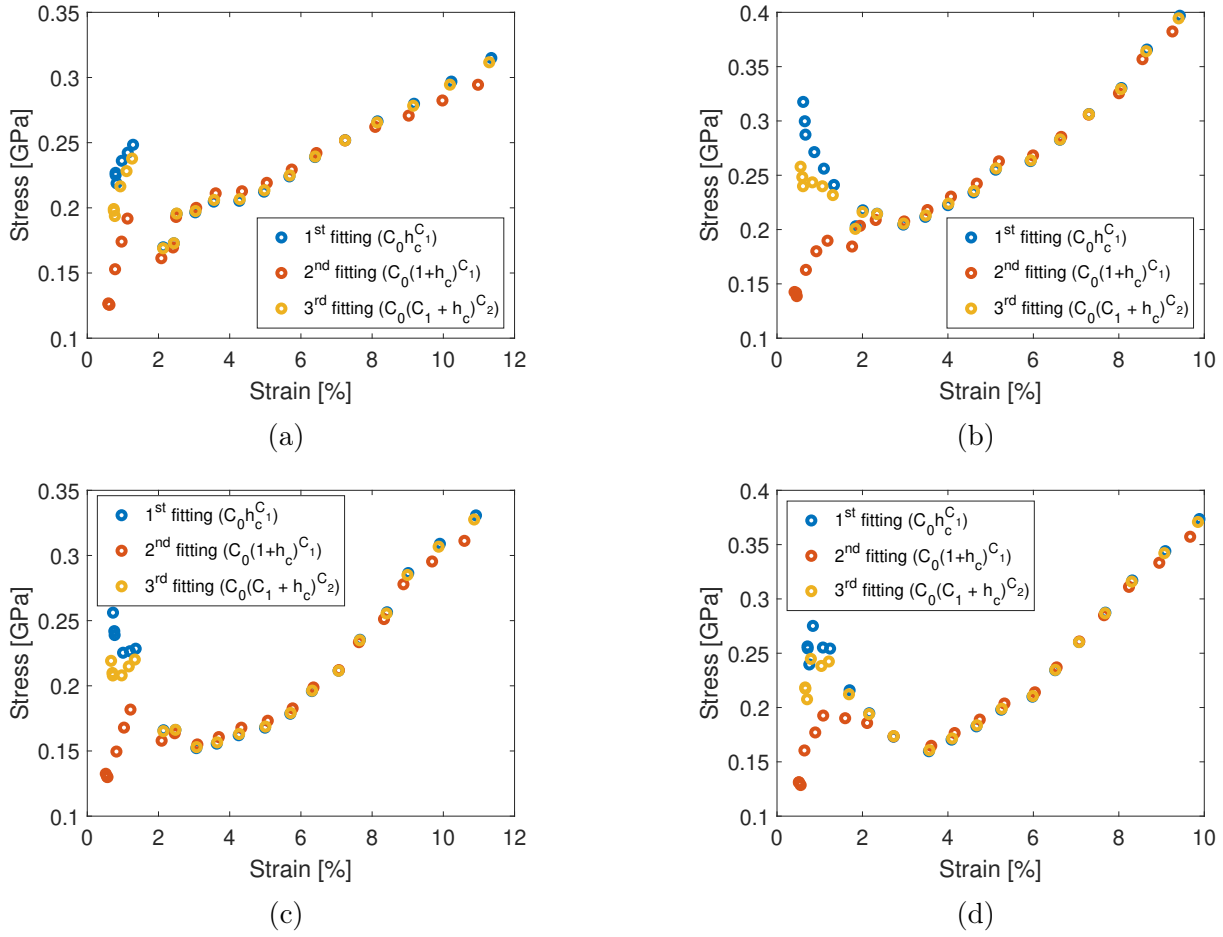


Figure 2.11: Stress-strain curves of fibrolamellar bone in a 20  $\mu m$  window (a) No other load function was used in order to flatten the roughness (b) A cyclic load varying from 5  $\mu N$  to 10  $\mu N$  was applied to flatten the roughness (c) A cyclic load varying from 5  $\mu N$  to 30  $\mu N$  was applied to flatten the roughness (d) A cyclic load varying from 5  $\mu N$  to 50  $\mu N$  was applied to flatten the roughness.

## 2.3 Scanning electron microscopy

A Tescan Clara Ultra-High Resolution (UHR) SEM was used to capture some images of the surface of the sample and of the indents locations. Fortunately, no coating was needed as the resolution was already good. The samples were placed inside a low vacuum chamber, maintaining a pressure lower than atmospheric pressure but not as low as in high vacuum conditions. The typical accelerating voltage used during the experiment ranged from 10 to 20 keV.

The main objective behind capturing SEM images is to precisely locate the indent. Precise coordinates of the indents and their boundaries can be obtained from the nanoindenter. Moreover, in certain indentation areas, some high static loads were applied to border the indented zones. These larger indents are visible in the SEM images and the parameters chosen to perform those indents are explained in SECTION 2.2.7. Subsequently, it is possible to generate a plot including both the deeper indents and the cyclic indents based on their coordinates on MATLAB. By superimposing this plot onto the SEM images, the exact position of all indents can be visually determined.

# Chapter 3

## Results

This chapter presents the obtained results. The first section explains the terminology used to display the results. Then a section is devoted to the results acquired using the nanoindenter, such as optical views of the indentation zones, SPM pictures of the indentation areas, stress-strain curves and load-displacement over time. The last section encompasses diverse pictures and lamella thickness acquired using the scanning electron microscopy.

### 3.1 Data Structuring

As previously stated, two different Samples were tested and are referred as Sample 1 and Sample 2. Within each Sample, multiple zones were subjected to indentation. To ensure clarity, the following labelling scheme was employed for the different zones:

- In Sample 1, seven different zones were indented and identified as zone 1a, zone 1b, zone 1c, zone 2, zone 3, zone 4, and zone 5. The first three zones will not be analysed in the context of this thesis as the accuracy of the results was not guaranteed due to the possible drift of the nanoindenter. Nonetheless these results can be seen in the APPENDIX A.
- In Sample 2, four different zones were indented and identified as zone 6, zone 7, zone 8, and zone 9.

The method to get the stress-strain curves is explained in SECTION 2.2.6. In zone 4, zone 5, zone 6, and zone 7, a pre-load function was used in order to flatten the roughness present on the surface of the sample. The pre-load used is the one that varies from 0 to 10  $\mu\text{N}$  as shown in FIGURE 2.10a. Notably, zone 7 underwent a unique treatment involving five distinct tests. The first one is a regular one without flattening the roughness. For the three subsequent tests, a pre-load function was used with a varying peak loads. These different tests were done to compare the result with and without a pre-load. The last one concerns static indents to obtain the Young's modulus.

## 3.2 Nanoindentation tests

This section is dedicated to presenting all the data gathered from the nanoindentation tests. It is structured as follows: first, an optical view of the indentation area is presented, followed by an adjacent SPM picture illustrating the precise location of the indents. The acquisition of these SPM images was conducted using the following specific parameters:

- Scan rate = 0.4 Hz
- Scan size = 20  $\mu m$
- Scan resolution = 256
- Scan orientation = horizontal
- Set point = 2  $\mu N$
- Integral gain = 240

The term black lamella will refer to the lamellae that appear black on the SPM picture while the term white lamella refers to the one that appears white. After these pictures, the stress-strain curves are given the corresponding roughness of the indented zones. This roughness is computed on a 1  $\mu m$ -square around the indent with the EQUATION 2.6 and explained in SECTION 2.2.8. The value is provided next to its corresponding curve.

### 3.2.1 Sample 1

As mentioned earlier, the results for the first Sample are presented for four different zones: Zone 2, Zone 3, Zone 4, and Zone 5. These zones are located within the lamellar bone.

#### No flattening of the roughness

Within this Sample, nanoindentation tests were conducted on Zone 2 and Zone 3. No pre-load was applied to flatten the roughness.

##### ► Zone 2

The optical view of the nanoindentation area is depicted in FIGURE 3.1a, with the indented zone positioned in the middle. The two adjacent pictures (FIGURE 3.1b and 3.1c) represent the topographical and gradient images, respectively. A total of six indents were conducted: three on a black lamella and three on a white one.

In FIGURES 3.2, the stress-strain curves for each indent are presented. The curves corresponding to the indents within the black lamella are placed on the left side (FIGURE 3.2a), whereas the curves for the indents within the white lamella are situated on the right side (FIGURE 3.2a). Information on each indent can be found in TABLE 3.1.

	Indent 0	Indent 1	Indent 2	Indent 3	Indent 4	Indent 5
Location	black	black	black	white	white	white
Roughness	9.2673	5.2809	13.0507	10.0143	7.4352	16.6455

Table 3.1: Roughness and type of lamella of each indent of Zone 2.

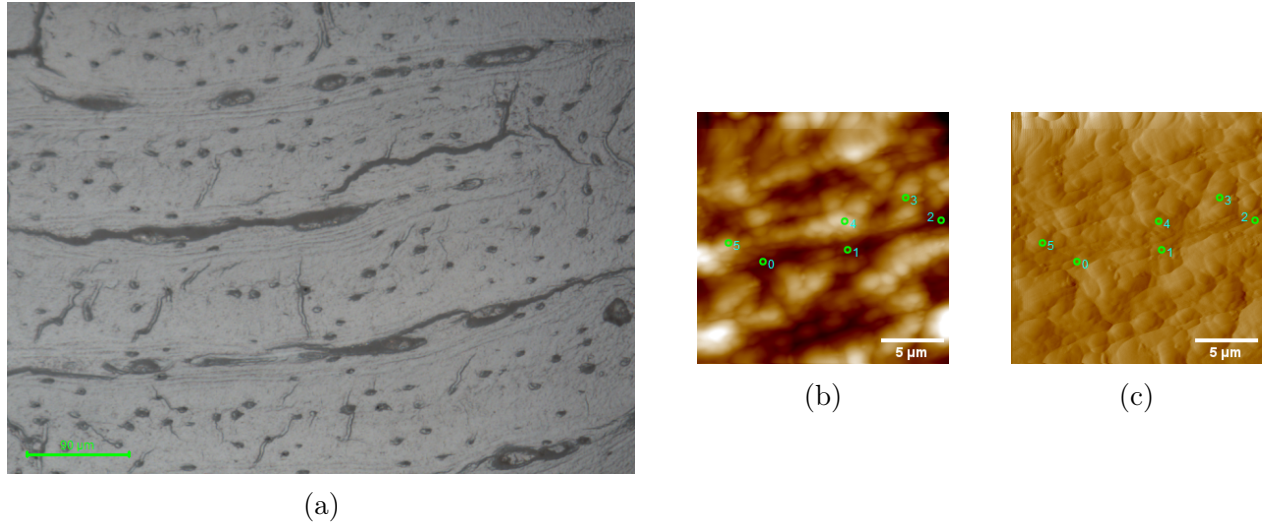


Figure 3.1: Indentation zone 2 a) Optical view b) Topographical SPM picture c) Gradient SPM picture.

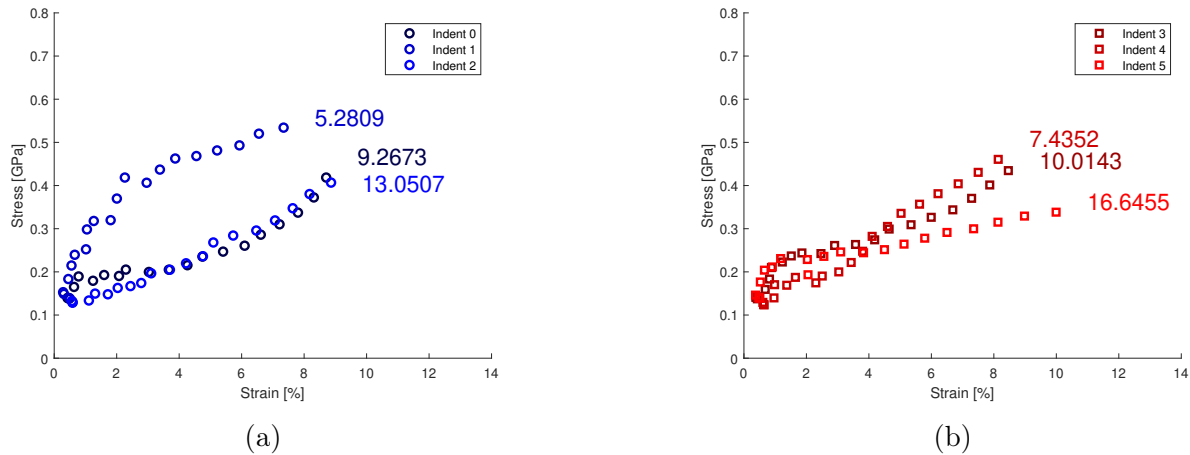


Figure 3.2: Stress-strain curves of zone 2 a) black lamella b) white lamella.

In FIGURE 3.2a, the behaviour of indents 0 and 2, situated on a black lamella, clearly stands out. It exhibits a notable feature of a convex upward trend in both stress and strain, culminating at around 0.4 GPa stress and 9% strain. In contrast, indent 1, positioned on a



black lamella as well, showcases a different behaviour. It demonstrates a concave trend in both stress and strain, reaching 8% strain and approximately 0.6 GPa stress. Transitioning to indents 3, 4, and 5 (FIGURE 3.2b) located on a white lamella, they demonstrate an initial rapid escalation in both stress and strain, reaching 2% strain and around 0.2 GPa stress. Subsequently, the rate of increase becomes less important in stress, with indents 3 and 4 reaching 8% strain and approximately 0.44 GPa stress, while indent 5 reaches around 10% strain and 0.3 GPa stress. In summary they have a similar behaviour.

### ► Zone 3

In FIGURE 3.3a, the optical view of the nanoindentation area is presented, with the indented zone positioned in the middle. The two adjacent pictures, FIGURE 3.1b and FIGURE 3.1c, illustrate the topographical and gradient images, respectively. Within this zone, a total of seven indents were performed: four on a black lamella and three on a white lamella.

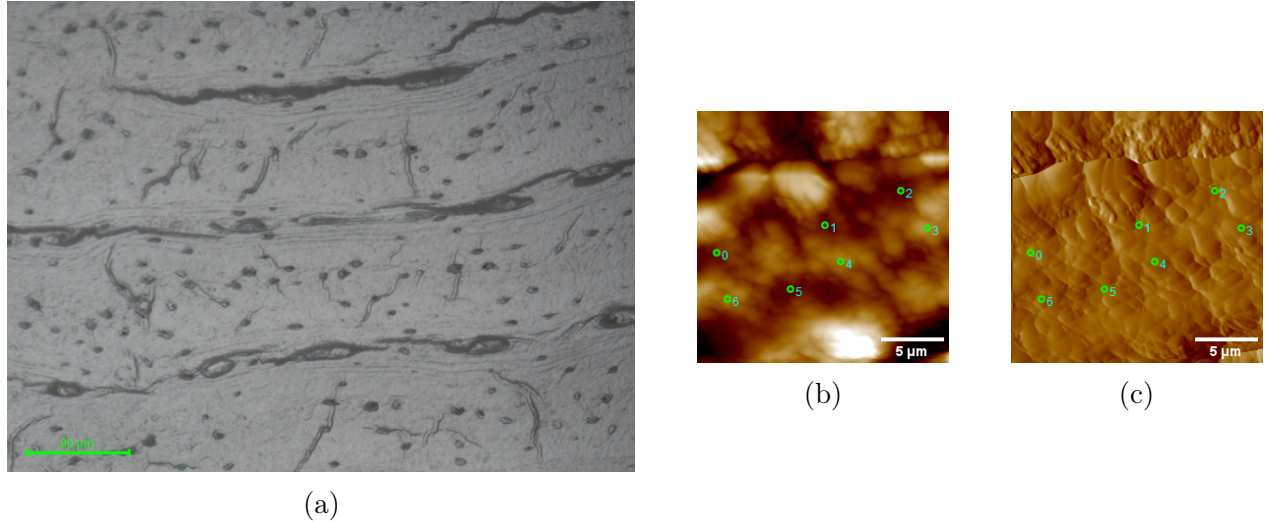


Figure 3.3: Indentation zone 3 a) Optical view b) Topographical SPM picture c) Gradient SPM picture.

Within FIGURES 3.4, the stress-strain curves for each indent are displayed. The curves corresponding to the indents within the black lamella are placed on the left side (FIGURE 3.4a), while the curves for the indents within the white lamella are situated on the right side FIGURE 3.4a. Information on each indent can be found in TABLE 3.2.

	Indent 0	Indent 1	Indent 2	Indent 3	Indent 4	Indent 5	Indent 6
Location	black	black	black	white	white	black	white
Roughness	11.9596	10.2074	7.6681	6.4538	8.1719	5.7462	5.3050

Table 3.2: Roughness and type of lamella of each indent of Zone 3.

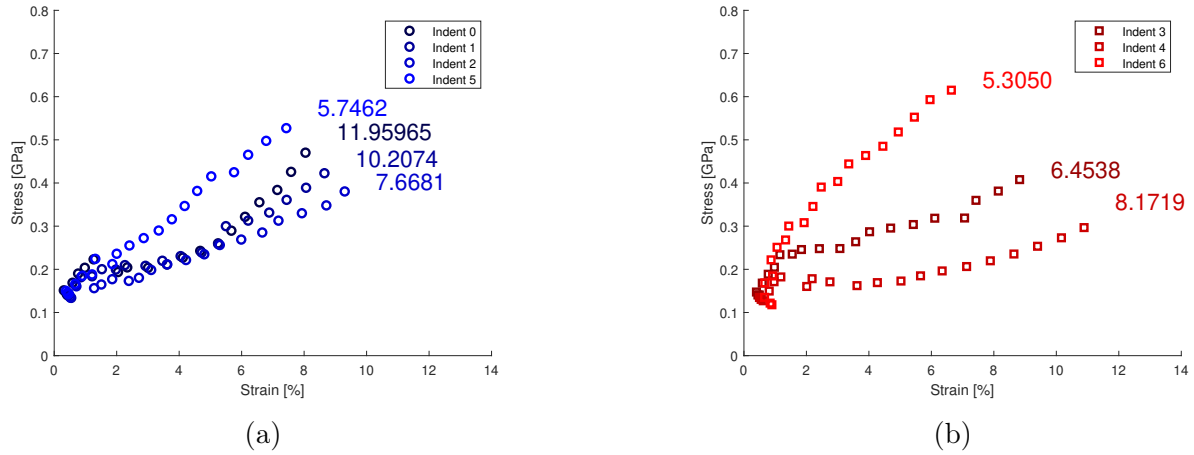


Figure 3.4: Stress-strain curves of zone 3 a) black lamella b) white lamella.

As depicted in FIGURE 3.4a, indents 0, 1, and 2 positioned on a black lamella exhibit a comparable behaviour characterised by a swift linear increase in stress and strain. This pattern persists until around 2% strain and 0.2 GPa in stress. Beyond this point, the increase remains linear in both stress and strain but the rise in stress is not as substantial, culminating at 8-10% strain and approximately 0.3-0.5 GPa in stress. Indent 5, also located on a black lamella, appears to only increase linearly until it reaches 8% in strain and 0.55 GPa in stress. Transitioning to indents 3, 4, and 6 (FIGURE 3.4b), which are situated on a white lamella, they demonstrate different behaviours. Indents 3 and 4 share a similar characteristic, with an initial linear increase in both stress and strain up to 2% in strain and 0.25 GPa stress for indent 3, and 0.2 GPa stress for indent 4. Following that, the pace of escalation notably decelerates for stress, eventually attaining 9% strain and 0.4 GPa stress for indent 3, and approximately 11% strain and 0.3 GPa stress for indent 4. In contrast, indent 6 also undergoes a linear increase in both stress and strain, but the slope is more important, reaching 3% strain and 0.4 GPa stress. The increase persists, leading to a final point of 6.5% strain and 0.65 GPa stress.

### Flattening of the roughness

In this particular Sample, nanoindentation tests were performed on Zone 4 and Zone 5. The roughness in these zones was flattened using a pre-load of  $10 \mu\text{N}$ , as detailed in SECTION 2.2.6.

#### ► Zone 4

The optical view of the nanoindentation area is illustrated in FIGURE 3.5a, with the central location of the zone highlighted by the static indent as explained in SECTION 2.2.7. The two adjacent pictures (FIGURE 3.5b and 3.5c) display the topographical and gradient images, respectively. A total of six indents were performed within this zone: three along the black lamella and three along the white lamella.

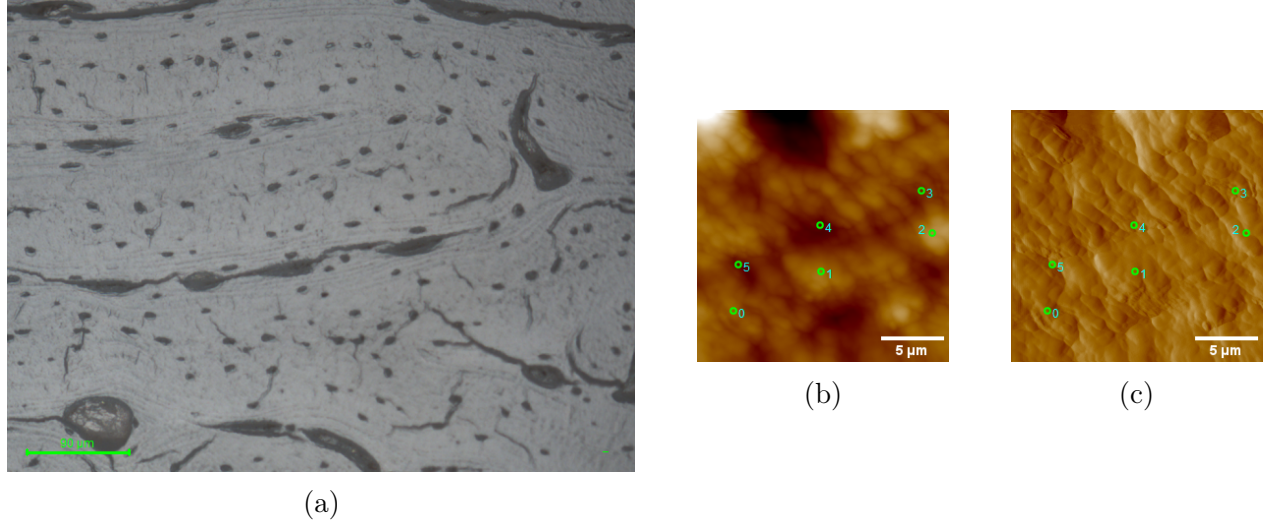


Figure 3.5: Indentation zone 4 a) Optical view b) Topographical SPM picture c) Gradient SPM picture.

In FIGURES 3.6, the stress-strain curves for each indent are displayed. The curves of the indents within the black lamella are positioned on the left side (FIGURE 3.6a), while the curves for the indents within the white lamella are located on the right side (FIGURE 3.6a). Information on each indent can be found in TABLE 3.3

	Indent 0	Indent 1	Indent 2	Indent 3	Indent 4	Indent 5
Location	white	white	white	black	black	black
Roughness	6.9857	9.6136	8.3719	6.5343	8.8955	13.3108

Table 3.3: Roughness and type of lamella of each indent of Zone 4.

As depicted in FIGURE 3.6a, indents 3, 4, and 5 positioned on a black lamella exhibit a similar behaviour characterised by a swift linear increase in stress and strain. This pattern persists until around 2% strain and 0.3 GPa in stress. Beyond this point, the elevation continues in a linear fashion for both stress and strain, albeit with a reduced gradient, culminating at 8% strain and approximately 0.5 GPa in stress. Transitioning to indents 0, 1, and 2 (FIGURE 3.6b) located on a white lamella, they demonstrate an initial rapid escalation in both stress and strain, reaching a peak at 2% strain and 0.25 GPa stress. Subsequently, the linear rise in both stress and strain persists, although the increase in stress is less pronounced. For indentations 1 and 2, the strain reaches 10% with an approximate stress of 0.4 GPa, while for indentation 0, the strain reaches around 12% with a stress of 0.3 GPa. In summary the black lamella appears stiffer than the white one.

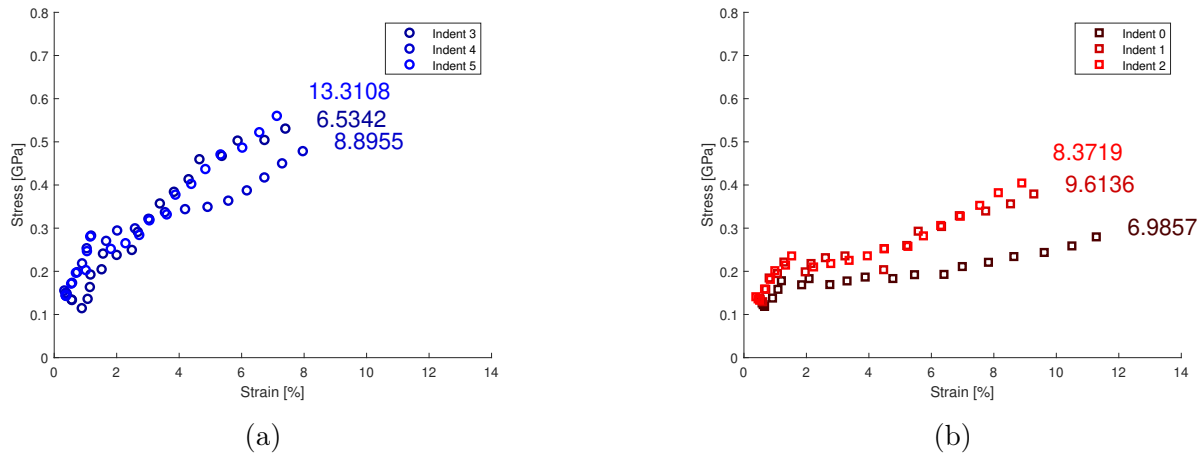


Figure 3.6: Stress-strain curves of zone 4 a) black lamella b) white lamella.

### ► Zone 5

The optical view of the nanoindentation area is presented in FIGURE 3.7a, with an emphasis made by the static indent on the central location of the zone. The two adjacent images (FIGURE 3.7b and 3.7c) depict the topographical and gradient picture, respectively. Within this zone, a total of eight indents were conducted: four along the black lamella and four along the white lamella.

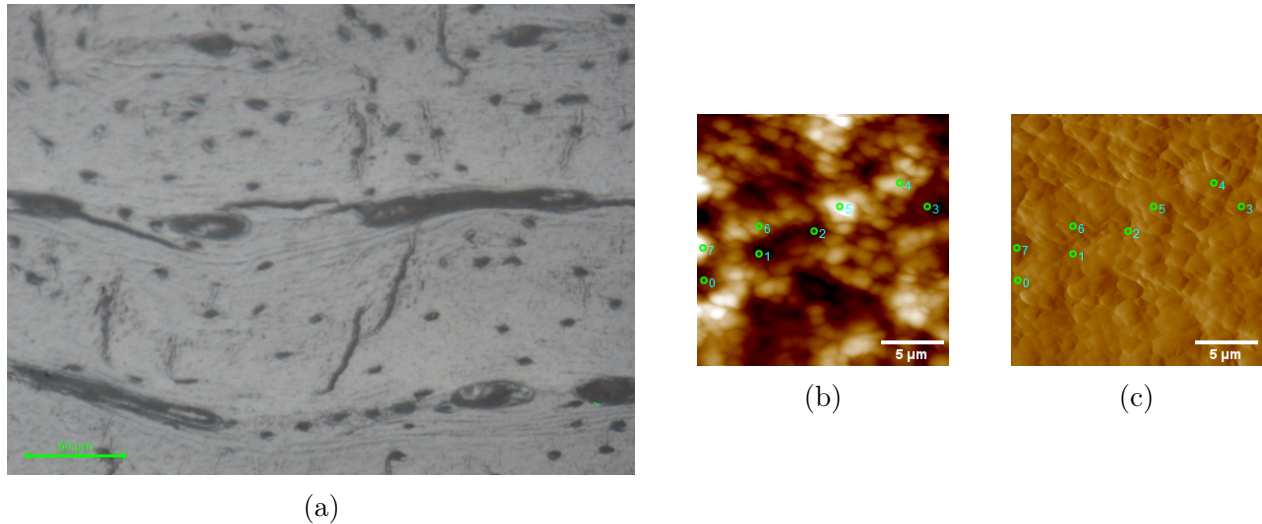


Figure 3.7: Indentation zone 5 a) Optical view b) Topographical SPM picture c) Gradient SPM picture.

In FIGURES 3.8, the stress-strain curves for each indent are showcased. Specifically, the curves pertaining to the indents within the black lamella are situated on the left side (FIGURE

3.8a), whereas the curves corresponding to the indents within the white lamella are positioned on the right side (FIGURE 3.8a). Information on each indent can be found in TABLE 3.4

	Indent 0	Indent 1	Indent 2	Indent 3	Indent 4	Indent 5	Indent 6	Indent 7
Location	black	black	black	black	white	white	white	white
Roughness	11.3789	12.0346	7.7327	10.4238	6.9168	9.3989	6.9469	17.4489

Table 3.4: Roughness and type of lamella of each indent of Zone 5.

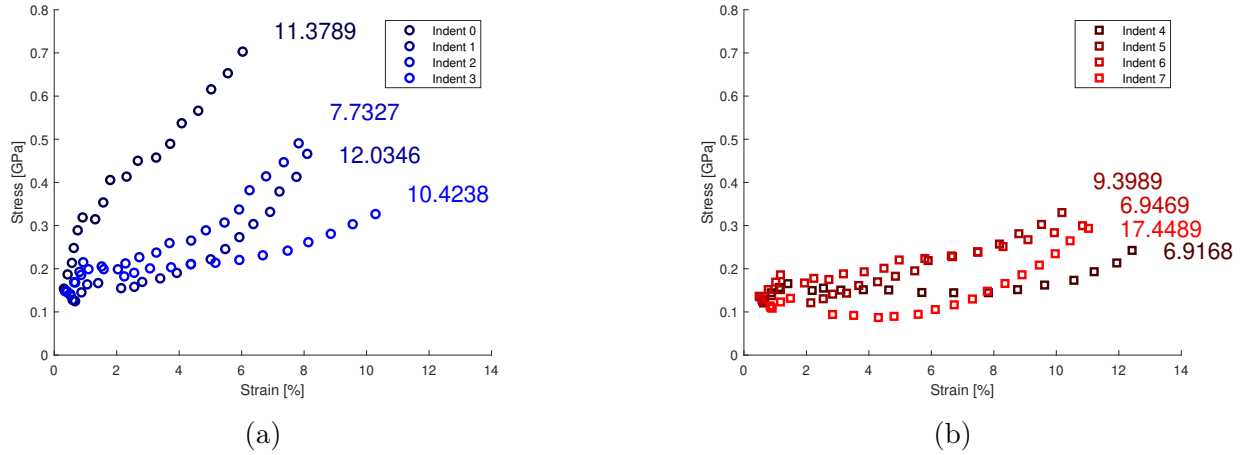


Figure 3.8: Stress-strain curves of zone 5 a) black lamella b) white lamella.

In FIGURE 3.8a, the behaviour of indents 1 and 2, positioned on a black lamella, is distinctly evident. It showcases a prominent characteristic of a linear increase in both stress and strain. This pattern persists until approximately 2% strain and 0.2 GPa stress, at which point the progression maintains linearity but at a reduced pace. Ultimately, they conclude at approximately 0.5 GPa stress and 8% strain. Meanwhile, indent 3, also on a black lamella, exhibits a behaviour similar to indents 1 and 2, but diverges after reaching 2% strain. The linear escalation slows down for stress and only attains a stress level of 0.3 GPa. Indent 0, positioned on a black lamella as well, diverges from the aforementioned behaviour. Its stress and strain experience a more rapid linear augmentation in both stress and strain until they reach 2% strain and 0.4 GPa stress. Beyond this point, the progression remains linear for both stress and strain, nonetheless the increase in stress is less pronounced, although still more significant compared to the other cases. It ultimately reaches 6% strain and 0.7 GPa stress. Shifting focus to indents 4, 5, 6, and 7 (FIGURE 3.8b) located on a white lamella, they display an initial minor yet swift rise in stress and strain, reaching a culmination at 1.75% strain and 0.2 GPa stress. Subsequently, the linear increase becomes less significant for the stress. Indeed, it only reaches 0.3 GPa stress. In summary, the black lamella demonstrates a higher stiffness compared to the white lamella.



### 3.2.2 Sample 2

As mentioned earlier, the results for the second sample are presented in this part. Focusing on four distinct zones: Zone 6, Zone 7, Zone 8, and Zone 9. The first two zones, Zone 6 and Zone 7, are located in the lamellar bone, while the latter two, Zone 8 and Zone 9, are situated in the parallel fibered layer.

#### ► Zone 6

In this particular zone, a pre-load of  $10 \mu N$  was applied to flatten the roughness, as previously discussed in the preceding chapter. The optical view of the nanoindentation area is shown in FIGURE 3.9a, with a specific focus on the central location of the zone. The two adjacent images (FIGURE 3.9b and 3.9c) provide visual representations of the topographical and gradient characteristics, respectively. Within this zone, a total of seven indents were conducted: four along a black lamella and three along a white lamella.

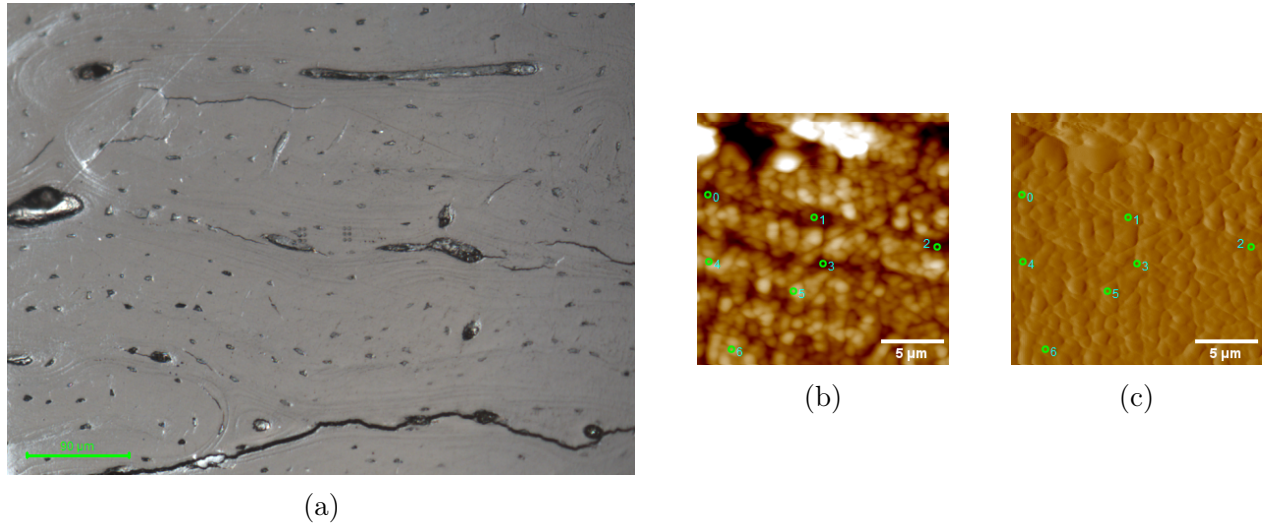


Figure 3.9: Indentation zone 6 a) Optical view b) Topographical SPM picture c) Gradient SPM picture.

In FIGURES 3.10, the stress-strain curves for each indent are presented. The curves corresponding to the indents within the black lamella are positioned on the left side (FIGURE 3.10a), while the curves for the indents within the white lamella are located on the right side (FIGURE 3.10a). Information on each indent can be found in TABLE 3.3

	Indent 0	Indent 1	Indent 2	Indent 3	Indent 4	Indent 5	Indent 6
Location	black	black	black	black	white	white	white
Roughness	7.7592	3.0090	7.5642	8.5476	5.0092	8.9181	2.7939

Table 3.5: Roughness and type of lamella of each indent of Zone 6.

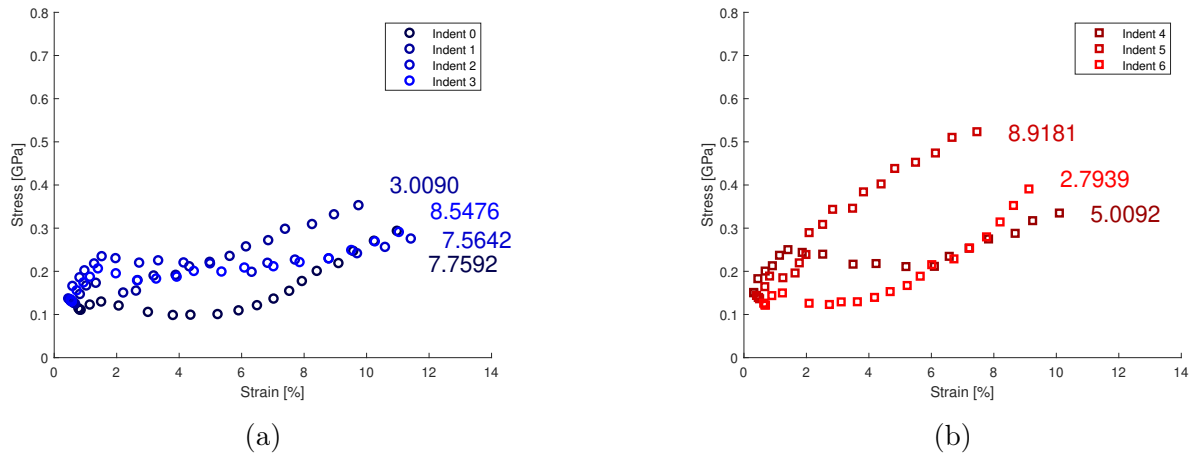


Figure 3.10: Stress-strain curves of zone 6 a) black lamella b) white lamella.

As depicted in FIGURE 3.10a, indents 0, 1, 2, and 3 positioned on a black lamella exhibit a shared initial linear rise in both stress and strain. This trend culminates at 2% strain, registering around 0.1 GPa stress for indent 0 and approximately 0.2 GPa stress for the others. Subsequently, the rate of increase becomes significantly milder. Specifically, it only reaches about 0.35 GPa stress and around 10% strain for indent 1, and about 0.3 GPa stress and around 12% strain for indent 2. It is noteworthy that the rise of indent 0 is not linear but slightly convex in nature. In FIGURE 3.10b, the behaviour of indents 4, 5, and 6 situated on a white lamella takes a distinct turn. Indent 4 exhibits a pronounced linear ascent in both stress and strain. This pattern persists until approximately 2% strain and 0.25 GPa stress, at which point the progression takes on a slightly concave shape. Eventually, they conclude at around 0.4 GPa stress and 9% strain. Indent 6 follows a different trajectory, with a minor linear increase until it reaches 1.8% strain and 0.15 GPa stress. Subsequently, the increase becomes notably slower, reaching 0.4 GPa stress and 9% strain. In contrast, indent 5 deviates from the aforementioned patterns. Its stress and strain experience a more pronounced linear increase until they reach 2% strain and 0.25 GPa stress. Beyond this point, the rise remains linear but less steep, though still more accentuated than the other cases. Ultimately, it reaches 8% strain and 0.55 GPa stress.

### ► Zone 7

In this zone, different nanoindentation tests were performed in order to analyse the impact of the roughness. The optical view of the nanoindentation area is depicted in FIGURE 3.11a, with the indented zone positioned in the middle and surrounded by the boundaries created by static indents as explained in SECTION 2.2.7. In total, the following five different tests were performed:

1. **Zone 7a:** No pre-load was applied to flatten the roughness of the surface before con-

ducting four indents. Two indents were performed on the black lamella, and two additional indents were made on the white lamella. FIGURES 3.11b and 3.11c show the topographical and gradient image of the surface, indicating the locations of the indents.

2. **Zone 7b:** A pre-load of  $10 \mu N$  was applied to flatten the roughness of the surface before conducting four indents as explained in SECTION 2.2.6. Two indents were performed on the black lamella, and two additional indents were made on the white lamella. FIGURES 3.11d and 3.11e show the topographical and gradient image of the surface, indicating the locations of the indents.
3. **Zone 7c:** A pre-load of  $30 \mu N$  was applied to flatten the roughness of the surface before conducting four indents, as detailed in SECTION 2.2.6. Two indents were performed on the black lamella, and two additional indents were made on the white lamella. Both the topographical and gradient images of the surface, show indent locations and are depicted in FIGURES 3.11f and 3.11g, respectively.
4. **Zone 7d:** A pre-load of  $50 \mu N$  was utilised to flatten the surface roughness before conducting four indents, as explained in SECTION 2.2.6. Two indents were carried out on the black lamella, and two additional indents were performed on the white lamella. Both the topographical and gradient images of the surface display the indent locations and are presented in FIGURE 3.11h and 3.11i, respectively.
5. **Zone 7e:** Several static indents were performed as explained in SECTION 2.2.7 to get the Young's modulus. Twelve indents were performed, six on the black lamella and six on the white one. The topographical image in FIGURES 3.11j and the gradient image in FIGURE 3.11k both display the locations of the indents on the surface.

FIGURE 3.12 depicts the stress-strain curves without any pre-load applied. The stress-strain curves presented in FIGURES 3.14, 3.16, and 3.18, corresponding to pre-loads of  $10 \mu N$ ,  $30 \mu N$ , and  $50 \mu N$ , respectively. For each figure, the left side represents the stress-strain curve for the black lamella, while the right side represents the white lamella. Information on each indent can be found in TABLE 3.6



	Indent 0	Indent 1	Indent 2	Indent 3
Location	black	white	black	white
Roughness	12.1080	2.9651	11.8590	4.5201

(a) Zone 7a

	Indent 0	Indent 1	Indent 2	Indent 3
Location	black	white	black	white
Roughness	9.1698	6.0605	10.8363	8.2019

(b) Zone 7b

	Indent 0	Indent 1	Indent 2	Indent 3
Location	black	white	black	white
Roughness	10.0682	7.4823	5.0238	6.3862

(c) Zone 7c

	Indent 0	Indent 1	Indent 2	Indent 3
Location	black	white	black	white
Roughness	6.4078	6.7800	3.8094	4.8504

(d) Zone 7d

Table 3.6: Roughness and type of lamella of each indent of Zone 7.

Below the stress-strain curves, additional graphs are represented that highlight the relationship between load and displacement over time. These curves aim to demonstrate whether the pre-load has any effect on the roughness, specifically if the displacement returns to zero in the case of the use of the pre-load. Within these graphs, the blue curves represent load variations over time, while the red curves depict displacement changes over time.

In Zone 7a, where no pre-load was employed, indents 0 and 2 are situated on a black lamella, while indents 1 and 3 are positioned on a white lamella. Illustrated in FIGURE 3.12a, indents 0 and 2 exhibit comparable behaviour. They initially rise linearly in both stress and strain, reaching a peak at 2% strain and approximately 0.2 GPa stress for indent 0, and around 0.3 GPa stress for indent 2. Subsequently, the linear increase in stress and strain continue although the slope diminishes. Indents 1 and 3 (FIGURE 3.12b) on a white lamellae display linear increments until they reach 10% strain and 0.4 GPa stress for indent 1, and 9% strain and 0.5 GPa stress for indent 3. Notably, the slope of the curve for indents located on the white lamellae is more pronounced compared to those on the black lamellae. In reference to FIGURE 3.13, indents 0 and 3 immediately manifest a non-zero displacements. Conversely, indents 1 and 2 shifts to a zero displacement following the 4<sup>th</sup> cycle for indent 1 at a load of 8.5  $\mu\text{N}$ , and during the 8<sup>th</sup> cycle for indent 2 at 18.1  $\mu\text{N}$ . It is important to consider an alternative perspective, which suggests that the transition to zero displacements might occur earlier in the 5<sup>th</sup> cycle at a load of 10.39  $\mu\text{N}$  for indent 2.

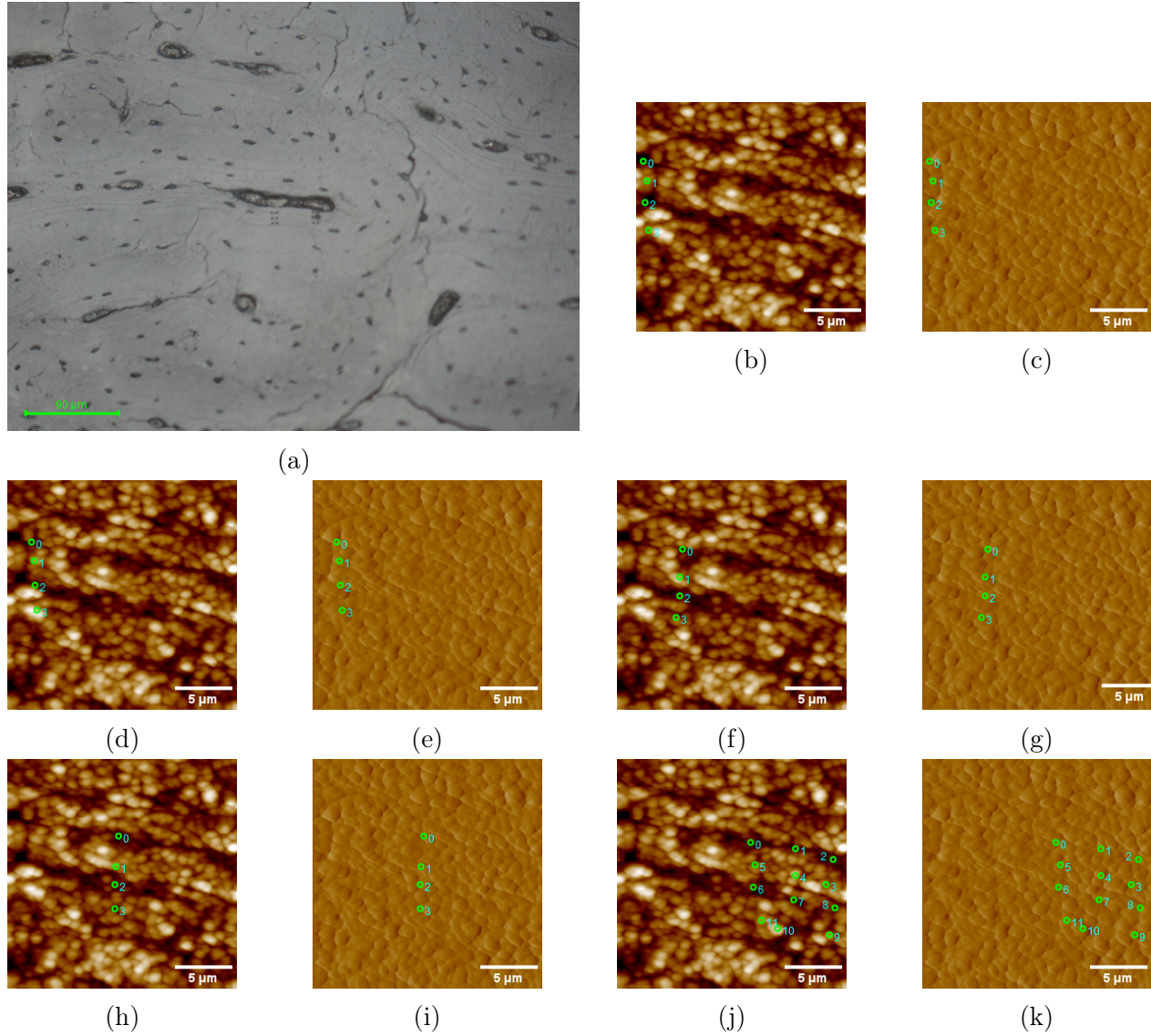


Figure 3.11: Indentation zone 7 a) Optical view b) Topographical SPM picture with no pre-load applied d)-f)-h) Topographical SPM picture with a pre-load of  $10\ \mu\text{N}$ ,  $30\ \mu\text{N}$  and  $50\ \mu\text{N}$  respectively c) Topographical SPM picture with no pre-load applied e)-g)-i) Gradient SPM picture with a pre-load of  $10\ \mu\text{N}$ ,  $30\ \mu\text{N}$  and  $50\ \mu\text{N}$  respectively j) Topographical SPM picture of the static indent k) Gradient SPM picture of the static indent.

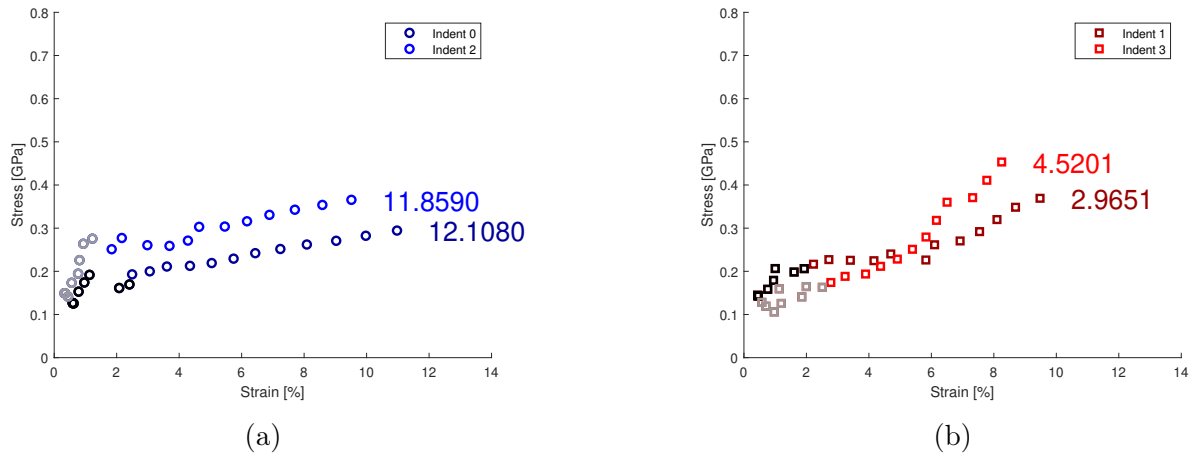


Figure 3.12: Stress-strain curves of zone 7a a) black lamella b) white lamella.

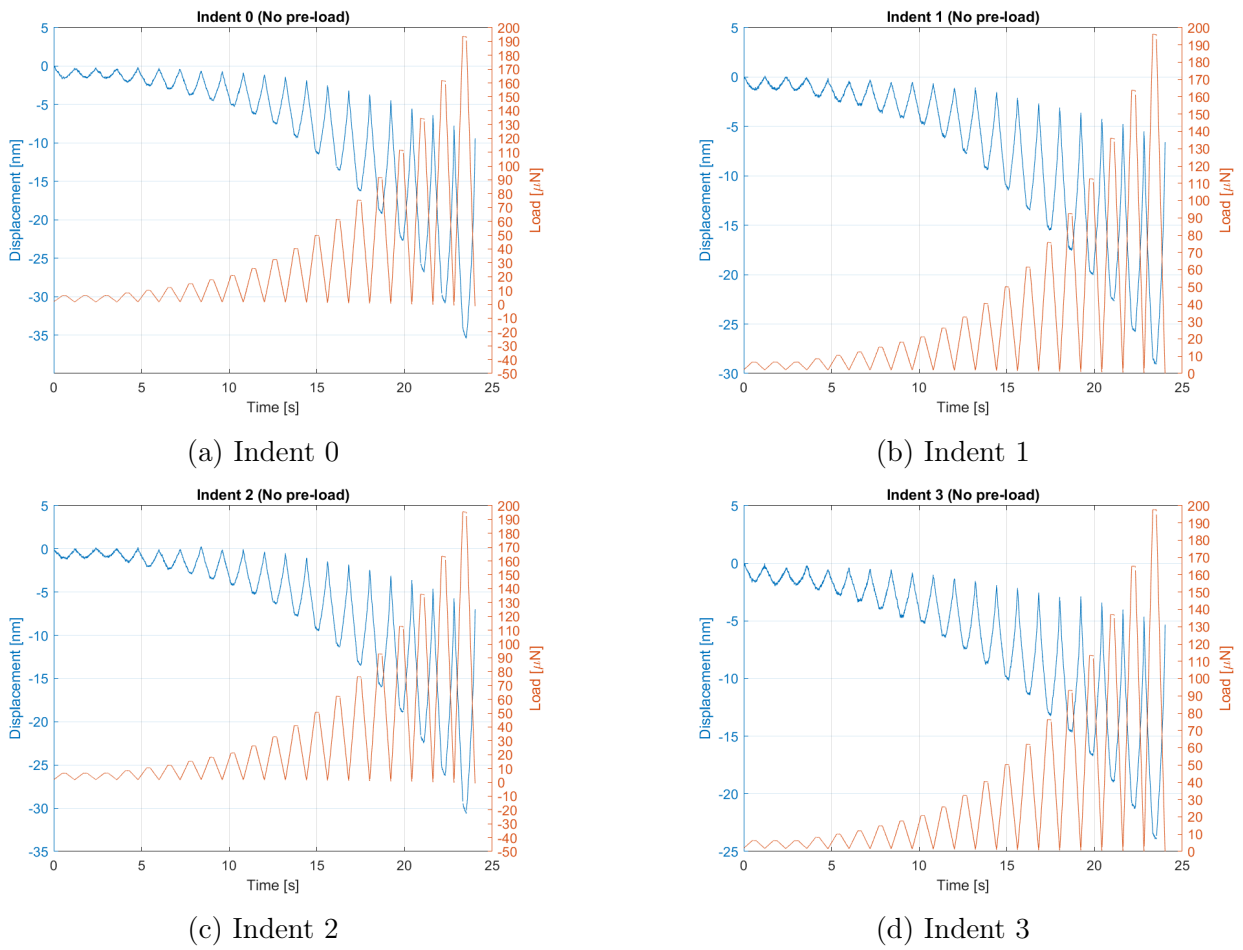


Figure 3.13: Load-displacement time plot of the indent of zone 7a.

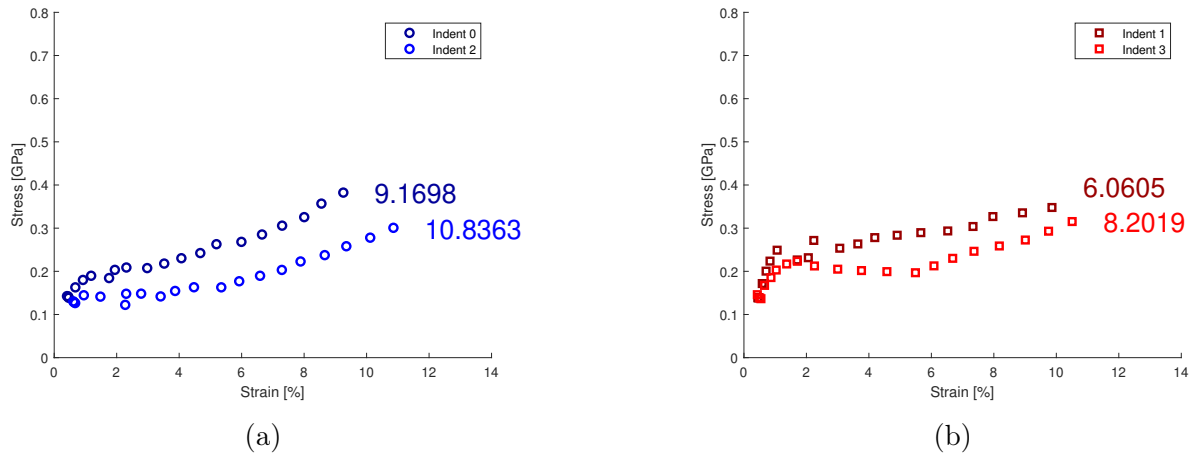


Figure 3.14: Stress-strain curves of zone 7b a) black lamella b) white lamella.

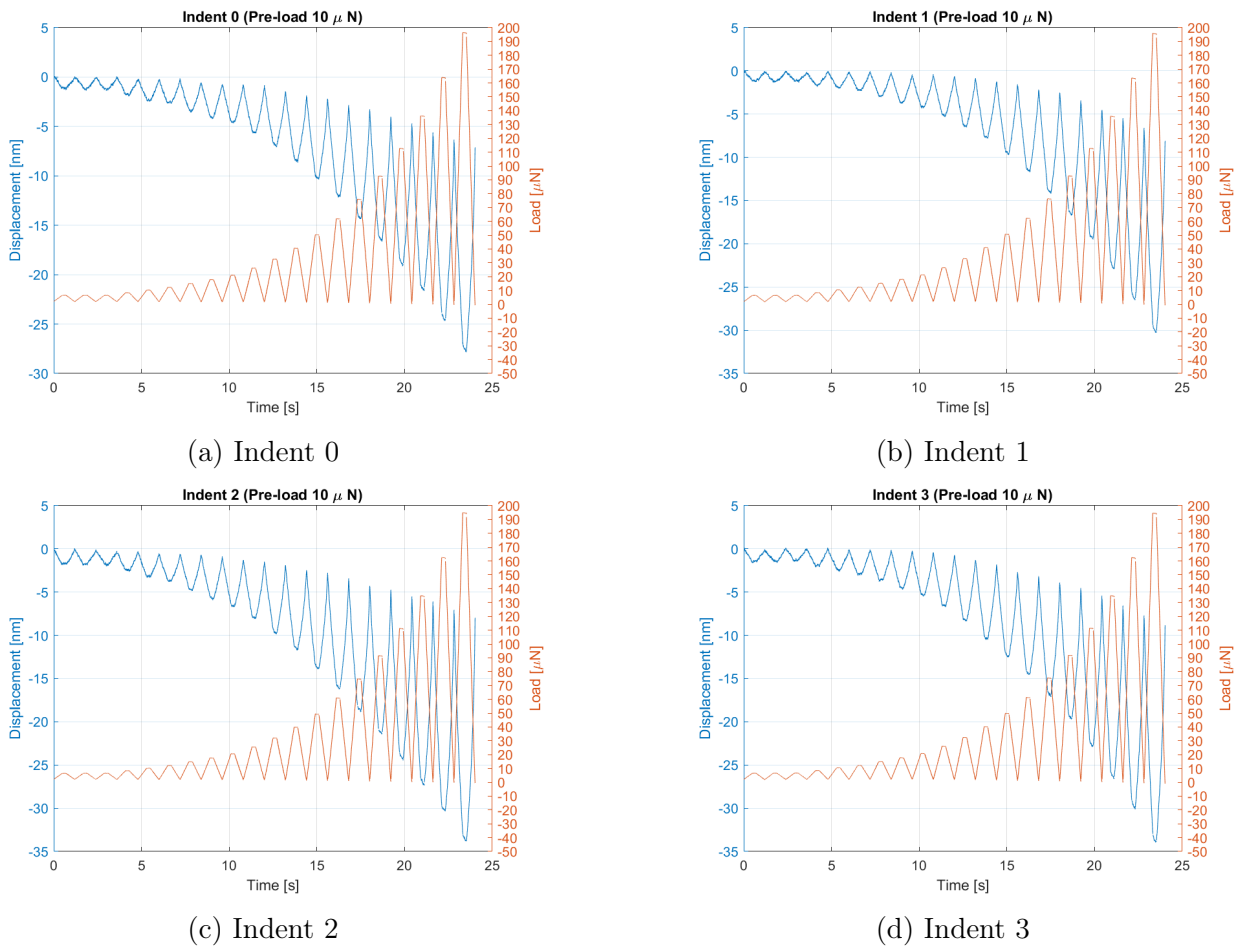


Figure 3.15: Load-displacement time plot of the indent of zone 7b.

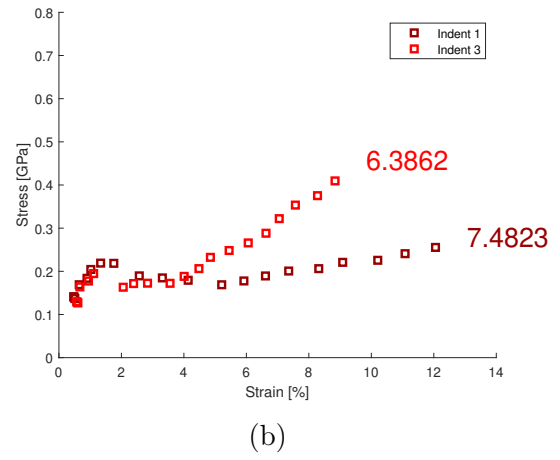
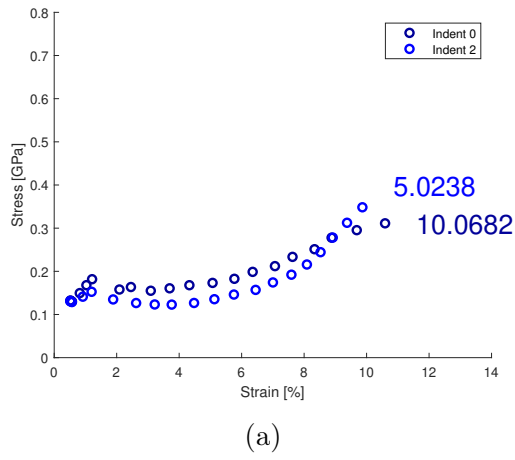


Figure 3.16: Stress-strain curves of zone 7c a) black lamella b) white lamella.

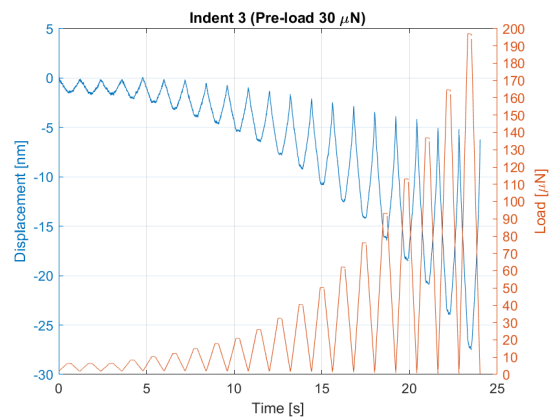
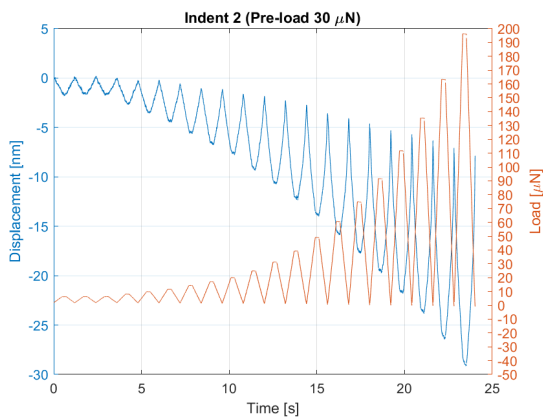
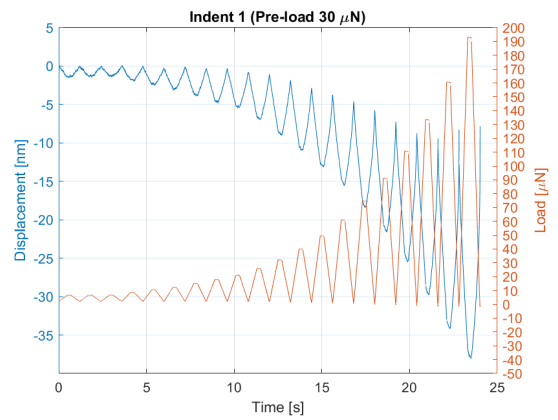
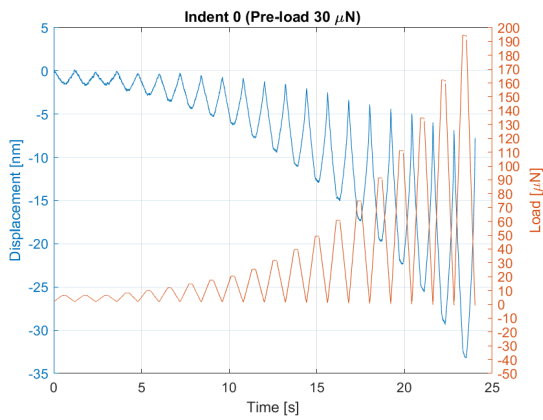


Figure 3.17: Load-displacement time plot of the indent of zone 7c.

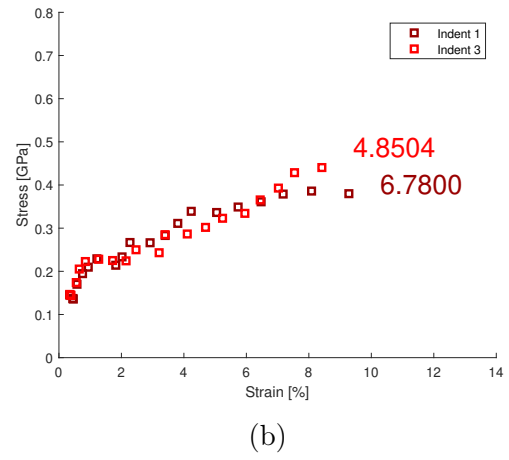
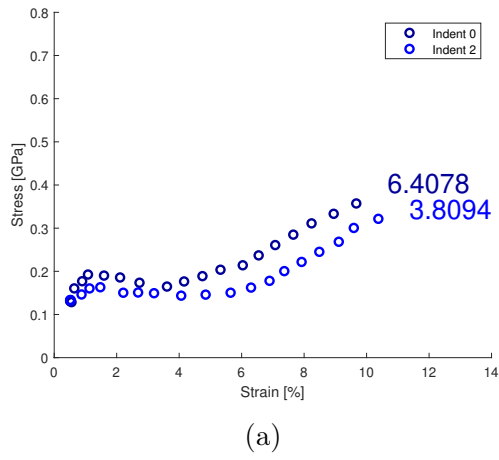


Figure 3.18: Stress-strain curves of zone 7d a) black lamella b) white lamella.

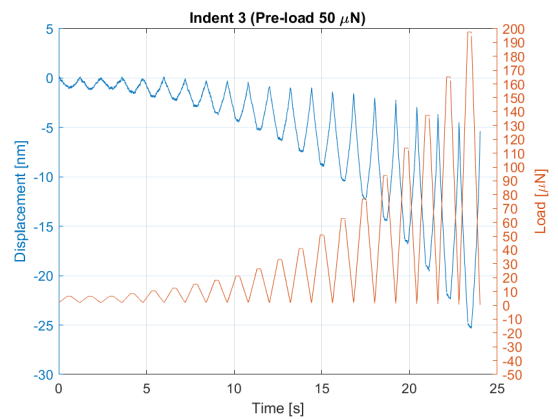
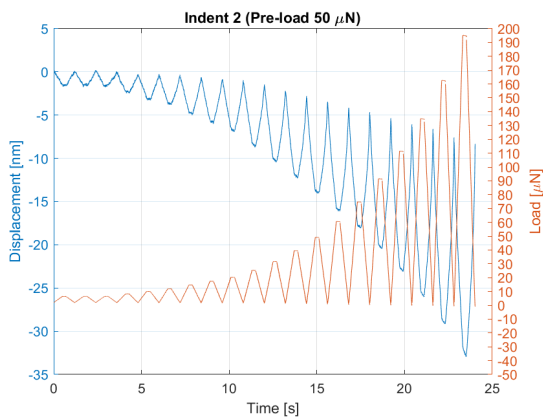
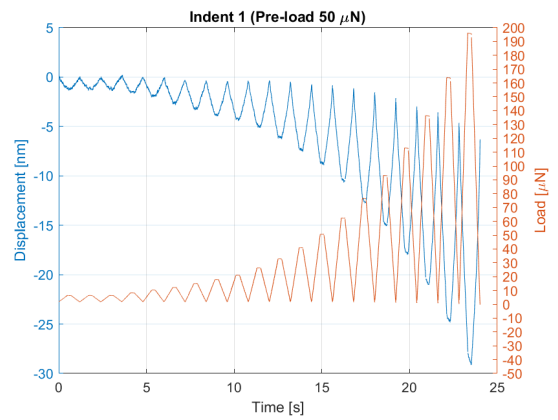
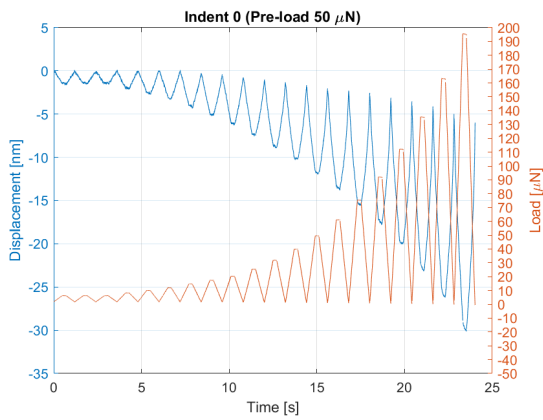


Figure 3.19: Load-displacement time plot of the indent of zone 7d.

In Zone 7b, where a pre-load of  $10\ \mu\text{N}$  was applied, indents 0 and 2 are located on a black lamella, while indents 1 and 3 are positioned on a white lamella. As illustrated in FIGURE 3.14a, indents 0 and 2 showcase a comparable pattern. They initially demonstrate a linear rise in both stress and strain, peaking at 2.5% strain and approximately 0.15 GPa stress for indent 0, and around 0.2 GPa stress for indent 2. Subsequently, this linear increase in stress and strain continues, albeit with a diminishing slope, though not to the extent observed in Zone 7a. Indents 1 and 3 (FIGURE 3.14b) on a white lamella exhibit linear increments until they reach 2% strain and 0.3 GPa stress for indent 1, and 9% strain and 0.3 GPa stress for indent 3. Following this, a linear increase in stress and strain still persists, although the slope is less prominent, as depicted in Zone 7a for the black lamella, until reaching 11% strain and 0.3 GPa stress. In FIGURE 3.15, the observations indicate a common trend where all cycle returns to a zero-displacement until a certain load is applied. For indent 0, this transition occurs at the 4<sup>th</sup> cycle with a load of  $8.32\ \mu\text{N}$ . In the case of indent 1, the transition happens during the 7<sup>th</sup> cycle at a load of  $14.73\ \mu\text{N}$ . Indent 2 achieves a non-zero value at the 3<sup>rd</sup> cycle with a load of  $6.5\ \mu\text{N}$ . Lastly, the displacement of indent 3 shifts to a non-zero value during the 5<sup>th</sup> cycle at  $10.46\ \mu\text{N}$ .

In Zone 7c, where a pre-load of  $30\ \mu\text{N}$  was applied, indents 0 and 2 are situated on a black lamella, while indents 1 and 3 are located on a white lamella. As depicted in FIGURE 3.16a, indents 0 and 2 exhibit a similar trend. They initially display a linear increase in both stress and strain, reaching a peak at 2% strain and approximately 0.2 GPa stress for both indents. Subsequently, the curve takes on an upward-curving shape in both stress and strain. Indents 1 and 3 (FIGURE 3.16b) on a white lamella demonstrate linear increments until they reach 2% strain and 0.2 GPa stress for both indents. Following this, a linear increase in stress and strain persists, although the slope is not identical to indents 1 and 3. Indent 3 presents a steeper slope than indent 1. The curve for indent 3 concludes at 9% strain and 0.4 GPa stress, while the curve for indent 1 concludes at 12% strain and 0.2 GPa stress. In FIGURE 3.17, it is clear that indents 0, 1 and 2 start with a few cycles without residual displacement until a specific load is applied. For instance, indent 0 deviates from zero displacements at the 4<sup>th</sup> cycle with a  $7.80\ \mu\text{N}$  load. Similarly, indent 2 follows suit during the same cycle corresponding to a load of  $4.8\ \mu\text{N}$ . Indent 1 shifts to a non-zero value at the 5<sup>th</sup> cycle, reached  $10.47\ \mu\text{N}$ . However, indent 3 does not start at 0 but its displacement decreases during the 5<sup>th</sup> cycle as the load reaches  $10.33\ \mu\text{N}$ .

In Zone 7d, where a pre-load of  $50\ \mu\text{N}$  was employed, indents 0 and 2 are situated on a black lamella, while indents 1 and 3 are placed on a white lamella. As depicted in FIGURE 3.12a, indents 0 and 2 exhibit a similar pattern to the indents located on a black lamella in Zone 7c. The peak is also evident at 2% strain and approximately 0.2 GPa stress. Indents 1 and 3 (FIGURE 3.12b) display a pattern comparable to the indents on a white lamella in Zone 7a. However, in this zone, a peak becomes apparent at 2.1% strain and 0.1 GPa stress for both indents. Subsequently, a linear increase in stress and strain still persists, although the slope is similar to that of indent 3 in Zone 7c. Based on the observations depicted in FIGURE 3.19, it is evident that all indents return to approximately 0 nm displacement until

a certain load is applied. For indent 0, the displacement begins to deviate from zero at a load of  $14.69 \mu\text{N}$  during the 7<sup>th</sup> cycle. Similarly, indent 1 exhibits a return to a non-zero value at the 6<sup>th</sup> cycle, corresponding to a load of  $12.19 \mu\text{N}$ . At the same number of cycles, indent 3 also reverts to a non-zero values, reaching this state at a load of  $15.30 \mu\text{N}$ . Subsequently, indent 2 follows suit during the 4<sup>th</sup> cycle, with a load of  $8.26 \mu\text{N}$  inducing the transition.

Finally, the box plot of the Young's modulus computed from the static indents performed in zone 7e thanks to EQUATION 1.4 based on the model of Oliver and Pharr, are represented in FIGURE 3.20. This plot clearly highlights that white lamellae are stiffer than black lamellae with a significance of  $p = 0.0411$ . The average Young's modulus of the black lamellae is  $17.90 \pm 2.26 \text{ GPa}$ , whereas the white lamellae have an average stiffness of  $21.23 \pm 2.37 \text{ GPa}$ . For specific data regarding each indent, refer to TABLE 3.7.

	Indent 0	Indent 1	Indent 2	Indent 3	Indent 4	Indent 5
Location	black	black	black	white	white	white
Roughness	5.2832	7.0145	4.1235	4.4161	5.1671	5.2867

	Indent 6	Indent 7	Indent 8	Indent 9	Indent 10	Indent 11
Location	black	black	black	white	white	white
Roughness	7.1477	7.7505	4.4067	7.6392	7.4447	3.7436

Table 3.7: Roughness and type of lamella of each indent of Zone 7e.

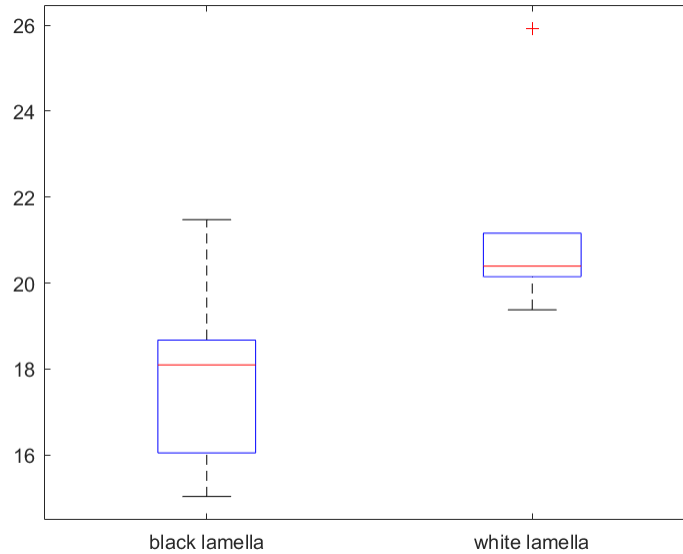


Figure 3.20: Boxplot of the Young's modulus of black and white lamellae located in zone 7e.



### Parallel-fibered bone

Nanoindentation was also performed in parallel-fibered bone in two distinct zones: zone 8 and zone 9. For both of these zones, no pre-load function was used to flatten the roughness.

#### ► Zone 8

In FIGURE 3.21a, the optical view of the nanoindentation area is presented, with an emphasis on the zone of indentations. Adjacent to it, FIGURES 3.21b and 3.21c display the topographical and gradient characteristics, respectively. A total of nine indents were conducted within this zone.

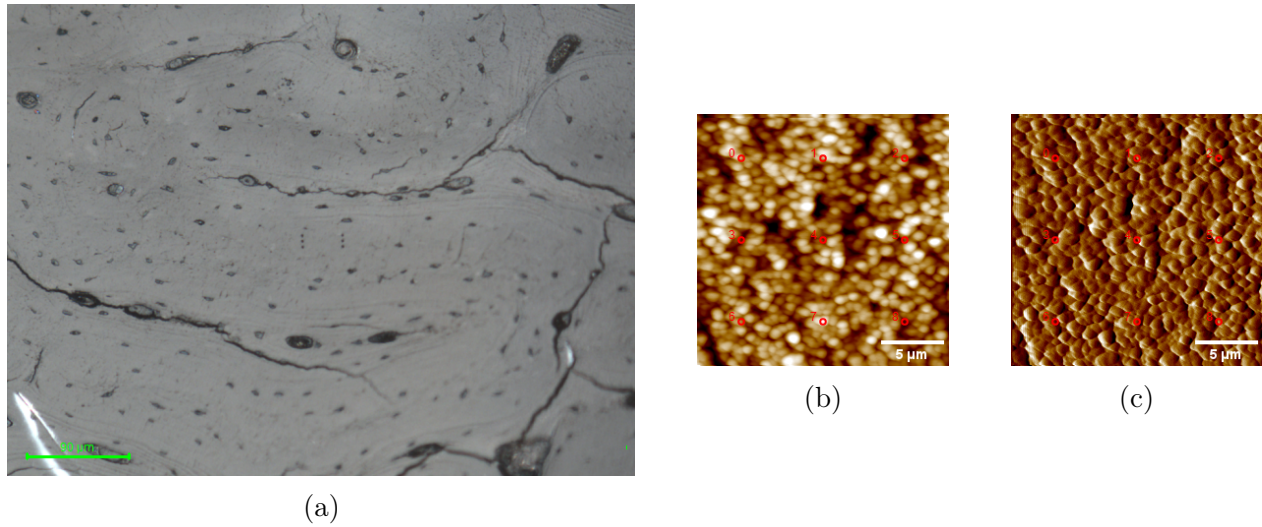


Figure 3.21: Indentation zone 8 a) Optical view b) Topographical SPM picture c) Gradient SPM picture.

FIGURE 3.22 presents the stress-strain curves for each indent. Each graph depicts three indents that are situated in the same line. Information on the roughness of each indent can be found in TABLE 3.8

	Indent 0	Indent 1	Indent 2	Indent 3	Indent 4
Roughness	4.5744	6.5059	5.7490	5.4218	3.9258

	Indent 5	Indent 6	Indent 7	Indent 8
Roughness	7.3713	3.9233	5.0569	5.8047

Table 3.8: Roughness and type of lamella of each indent of Zone 8.

As observed in FIGURE 3.22a, Indent 0 demonstrates a distinct behaviour from the others. It exhibits a linear rise in both stress and strain, marked by unusual points. Meanwhile, indents 1 and 2 share a similar pattern, displaying linear increases until reaching 1.7% strain

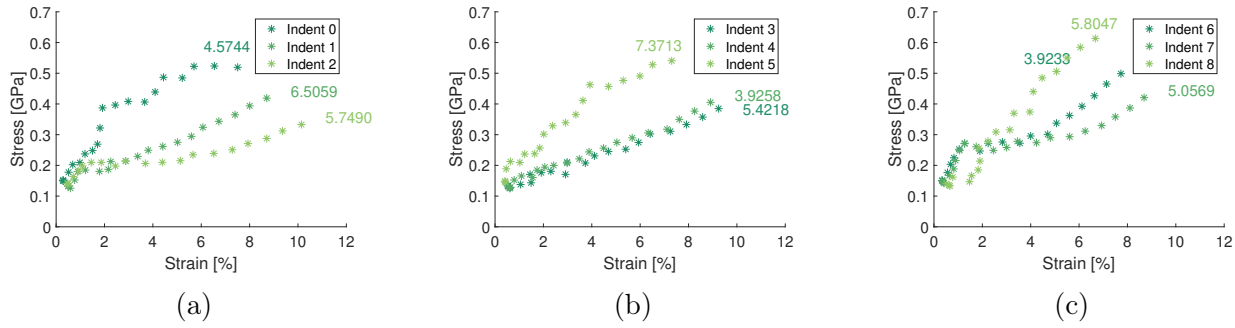


Figure 3.22: Stress-strain curves of zone 8.

and 0.2 GPa stress. Following this, a plateau emerges, more pronounced for Indent 2, extending to around 5% strain and 0.2 GPa stress for Indent 2, and approximately 2% strain and 0.2 GPa stress for Indent 1. Subsequently, both indents experience a renewed linear rise, concluding at 11% strain and 0.3 GPa stress for Indent 2, and about 9% strain and 0.4 GPa stress for Indent 1. Turning to FIGURE 3.22b, it is apparent that Indents 3 and 4 share a common behaviour. Both stress and strain increase linearly until reaching 10% strain and approximately 0.4 GPa stress. Indent 5 also follows a linear trend, but with a higher slope, reaching 8% strain and 0.6 GPa stress. Finally, referencing FIGURE 3.22c, Indents 6 and 7 exhibit similar behaviours. The curves rise linearly until reaching around 2% strain and 0.3 GPa stress. Afterwards, they enter a plateau until 5% strain and 0.3 GPa stress. Following this, they resume a linear ascent, culminating at around 8% strain and 0.5 GPa stress for Indent 6, and approximately 9% strain and 0.4 GPa stress for Indent 7. Notably, Indent 8 experiences a rapid linear increase in both stress and strain until reaching 7% strain and 0.6 GPa stress.

### ► Zone 9

The optical view of the nanoindentation area is displayed in FIGURE 3.23a, with indentation zone emphasis by the static indent. Adjacent to it, FIGURES 3.23b and 3.23c depict the topographical and gradient pictures, respectively. Within this zone, a total of nine indents were conducted.

FIGURE 3.24 display the stress-strain curves for each indent. Within each graph, three indents are depicted, all situated along the same line. Information on the roughness of each indent can be found in TABLE 3.9.

As observed in FIGURE 3.24a, Indent 2 displays a unique behaviour compared to the others. It follows a linear rise until reaching 12% strain and 0.3 GPa stress. On the other hand, Indents 0 and 1 share a similar trend, exhibiting linear increases until they reach 5% strain and around 0.3 GPa stress. Subsequently, they slightly diverge in their linear progression, with a more pronounced increase for Indent 1. This pattern concludes at 7.8%

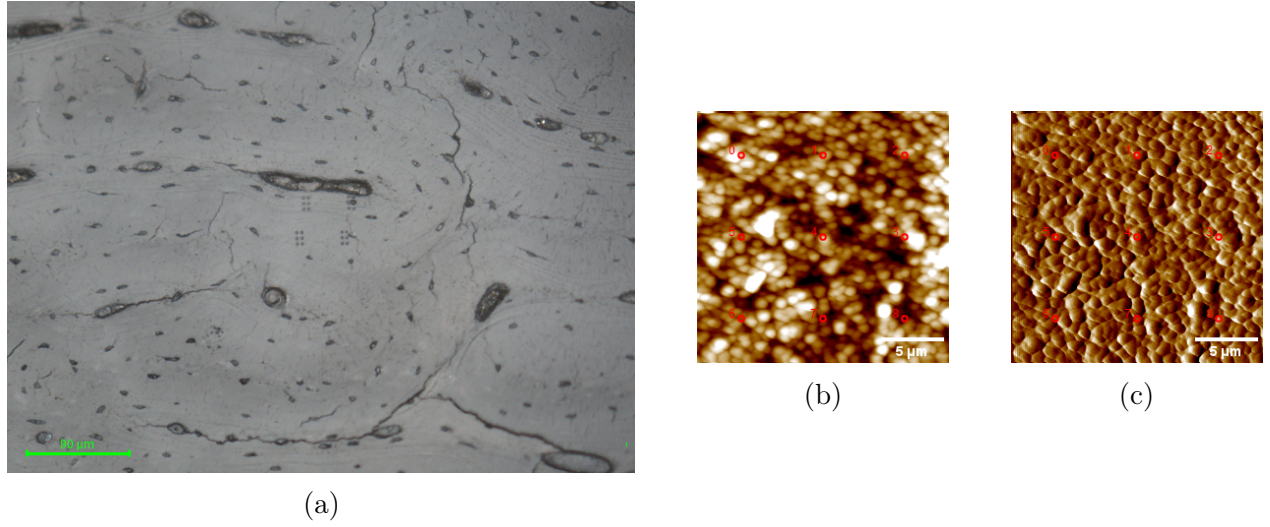


Figure 3.23: Indentation zone 9 a) Optical view b) Topographical SPM picture c) Gradient SPM picture.

	Indent 0	Indent 1	Indent 2	Indent 3	Indent 4
Roughness	5.5037	4.1554	6.3547	10.3184	6.9977

	Indent 5	Indent 6	Indent 7	Indent 8
Roughness	4.0933	3.7078	4.1615	7.0577

Table 3.9: Roughness and type of lamella of each indent of Zone 9.

strain and 0.6 GPa stress for Indent 1, and approximately 8.1% strain and 0.45 GPa stress for Indent 0. Referring to FIGURE 3.24b, indents 4 and 5 display a comparable behaviour. Both stress and strain exhibit linear growth until reaching a 3% strain and approximately 0.2 GPa stress. Subsequently, they enter a plateau phase lasting until around 6% strain and approximately 0.2 GPa stress for indent 4, and 0.3 GPa stress for indent 5. Afterwards, the increase in Indent 5's values shows a slightly gentler incline in both strain and stress, eventually reaching 9% strain and approximately 0.4 GPa stress. Meanwhile, Indent 4 attains 10% strain and approximately 0.35 GPa stress. As for Indent 3, it demonstrates a rapid linear surge in both stress and strain, reaching 8% strain and approximately 0.5 GPa stress. Finally, turning to FIGURE 3.24c, Indents 6 and 8 exhibit analogous behaviour. The curves show a linear ascent in both stress and strain until they reach approximately 10% strain and 0.4 GPa stress. In contrast, Indent 7 displays a distinct pattern, characterised by a rapid linear increase in both stress and strain until it reaches 2% strain and 0.4 GPa stress. Subsequently, the stress decreases to 0.35 GPa while the strain remains relatively constant. The curve then continues to rise linearly in both stress and strain until it reaches 8% strain and 0.5 GPa stress.

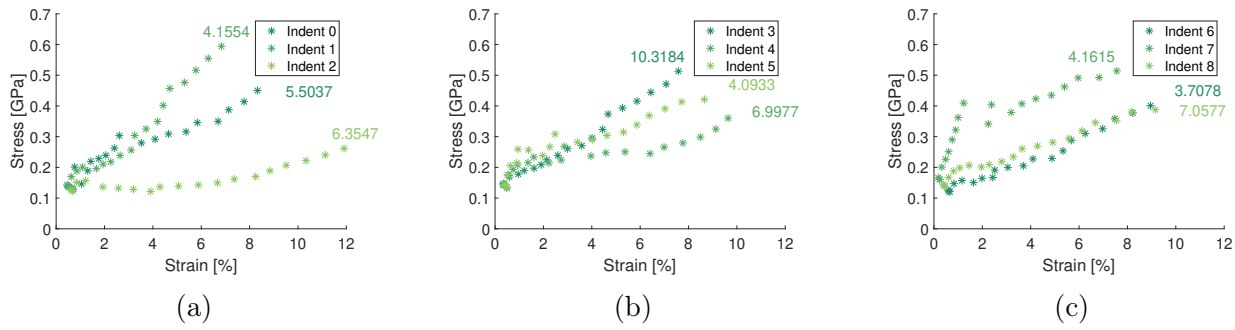


Figure 3.24: Stress-strain curves of zone 9.

### 3.3 Scanning electron microscopy

In this section some SEM images are shown from Samples 1 and 2. Additional images can be found in APPENDIX B.

#### 3.3.1 Sample 1

Unfortunately, for this sample, even if some indented zone were highlighted thanks to deeper indents, it was not possible to locate them using SEM. Nonetheless, some pictures were taken to display the difference between the two samples. FIGURE 3.25 showcases two different zones from the Sample 1 located in the lamellar region: Zone a (FIGURE 3.25a) and Zone b (FIGURE 3.25b). These pictures were taken with an accelerating voltage of 20 keV.

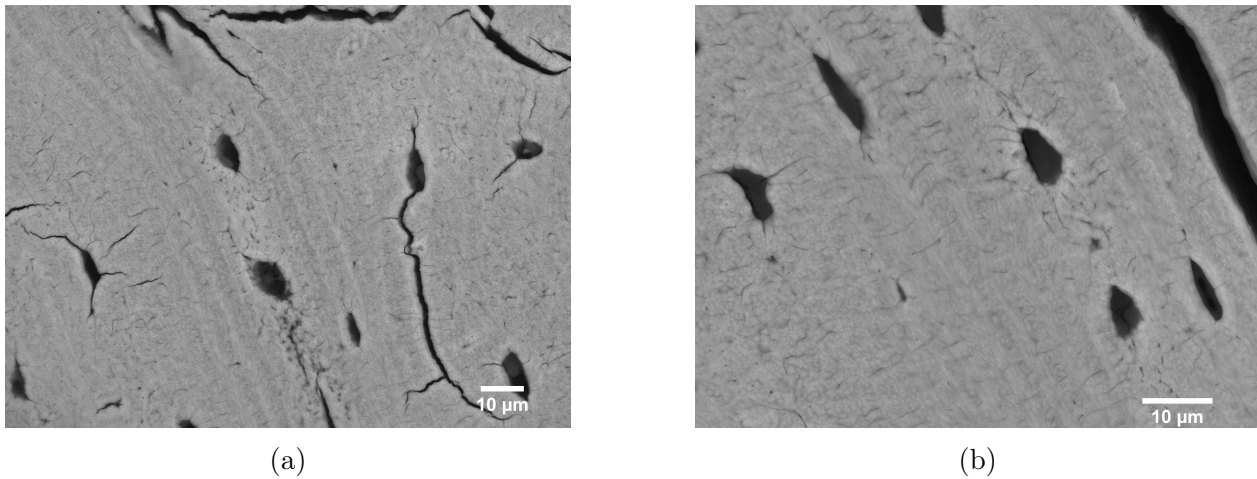


Figure 3.25: SEM pictures of Sample 1 a) Zone a b) Zone b.

The width of some lamellae was computed using FIJI and the following results are present in FIGURE 3.26. Thick lamellae have a width of  $2.97 \pm 0.94 \mu\text{m}$  in average while thin lamellae have an average of  $1.97 \pm 0.64 \mu\text{m}$ .

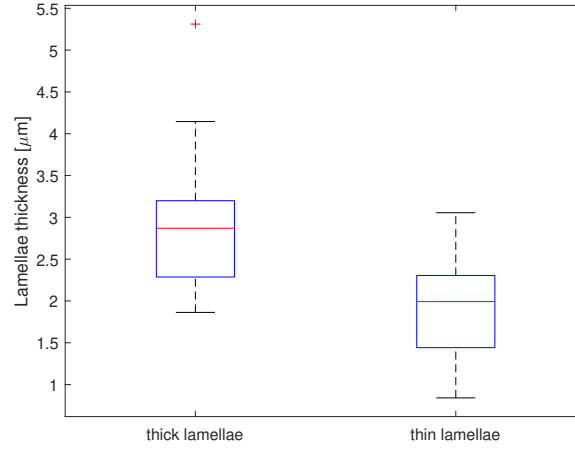


Figure 3.26: Boxplot of the lamella width in Sample 1.

### 3.3.2 Sample 2

SEM pictures in Sample 2 are available for four distinct zones: Zone 6, Zone 7, Zone 8, and Zone 9.

#### ► Zone 6

FIGURE 3.27 depict Zone 6, which is situated in the lamellar region. Although the boundaries are present, they might not be clearly visible. To enhance the visibility, adjustments such as contrast enhancements and zooming are applied. The magnified image, providing a better view of the location of the indent, is presented in FIGURE 3.27b. The acceleration voltage used to take this image is 10 keV.

From the magnified picture, one can locate the position of each indent. The information can be found in TABLE 3.10.

	Indent 0	Indent 1	Indent 2	Indent 3	Indent 4	Indent 5	Indent 6
Location	thin	thin	thin	thick <sup>*1</sup>	thick	thick	thick

Table 3.10: Location of lamellae of each indent of Zone 6.

<sup>\*1</sup> For indent 3, its location is close to a thin lamella.



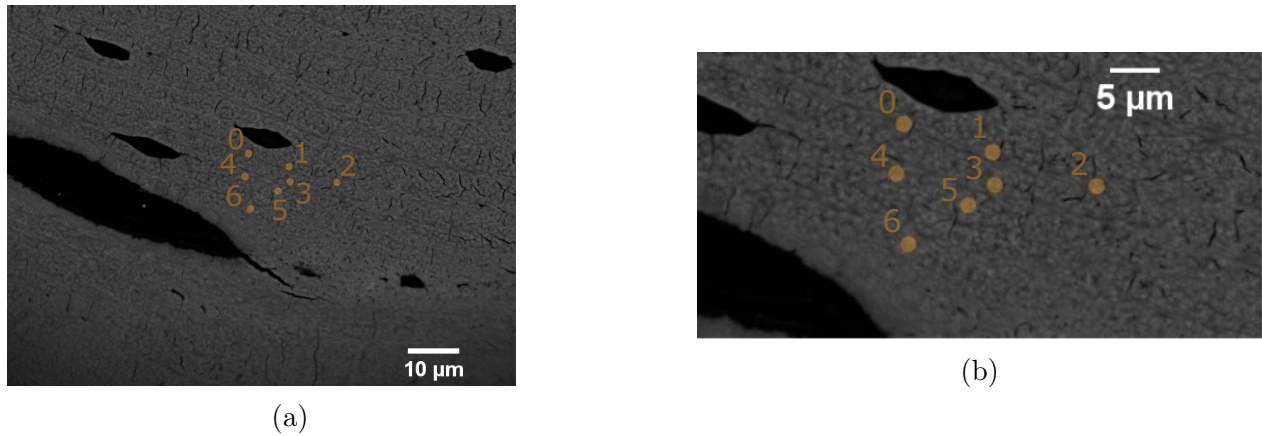


Figure 3.27: SEM pictures of zone 6 a) Indentation zone b) Zoom of the indentation zone.

The widths of certain lamellae were calculated using FIJI, and the corresponding outcomes are displayed in FIGURE 3.28. thick lamella width exhibit a mean of  $2.18 \pm 0.36 \mu\text{m}$ , whereas thin lamellae displays a mean of  $1.19 \pm 0.19 \mu\text{m}$ . The significance is  $p < 0.01$

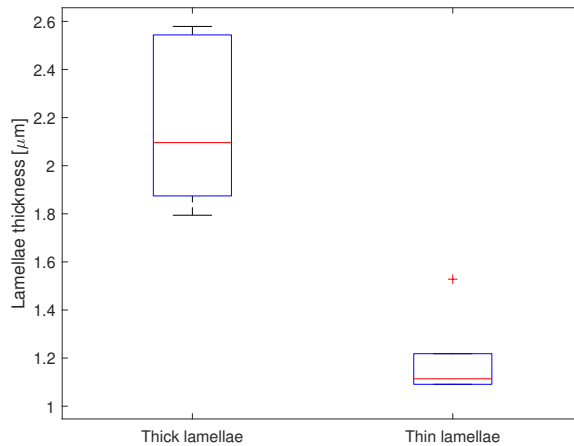


Figure 3.28: Boxplot of the lamella width in Zone 6.

### ► Zone 7

In this zone, as previously explained, five different tests were performed whose indents are represented in different colour depending on the kind of test. The colour orange (Zone 7a) is for the indent made without the use of a pre-load. The colour pink (Zone 7b), red (Zone 7c) and green (Zone 7d) are for the indent made with a pre-load of  $10 \mu\text{N}$ ,  $30 \mu\text{N}$  and  $50 \mu\text{N}$ , respectively. Finally, the colour blue (Zone 7e) is for the indent made with the static load to get the Young's modulus. FIGURE 3.29 illustrates the indentation zone with the colour code provided. The picture was taken with an accelerating voltage of 10 keV.

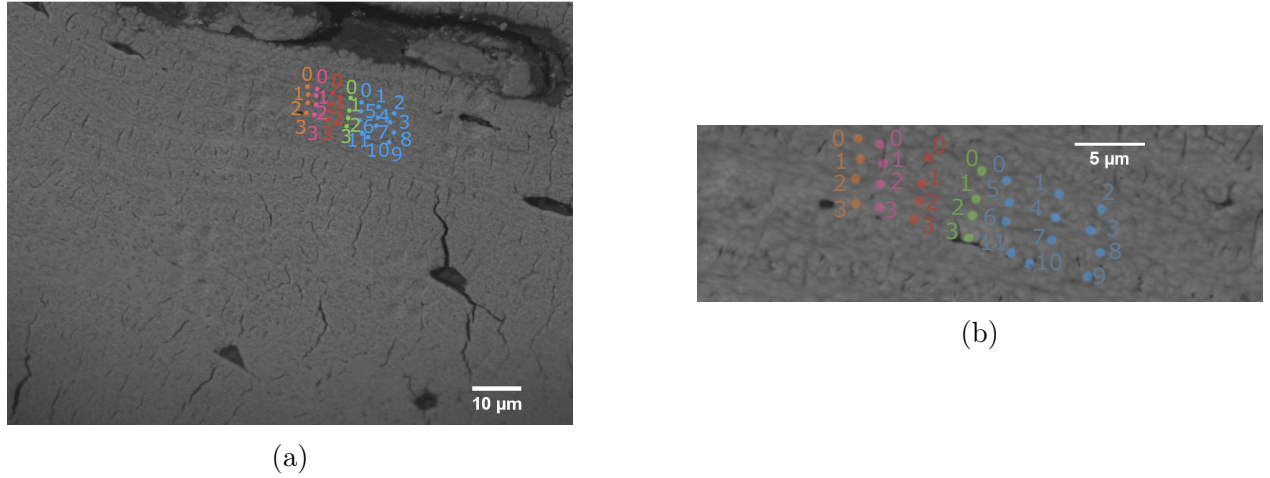


Figure 3.29: SEM pictures of zone 7 a) Indentation zone b) Zoom of the indentation zone.

From the magnified picture, one can locate the position of each indent. These positions are detailed in TABLE 3.11.

Indent °	0	1	2	3
Location	thin	thick	thin <sup>*2</sup>	thick

(a) Zone 7a

Indent °	0	1	2	3
Location	thin	thick <sup>*3</sup>	thin	thick

(c) Zone 7c

Indent °	0	1	2	3
Location	thin	thick	thin	thick

(b) Zone 7b

Indent °	0	1	2	3
Location	thin	thick <sup>*3</sup>	thin <sup>*2</sup>	thick

(d) Zone 7d

Indent °	0	1	2	3	4	5	6	7	8	9	10	11
Location	thin	thin	thin <sup>*2</sup>	thick	thick	thick	thin	thick <sup>*3</sup>	thin	thick	thick	thick

(e) Zone 7e

Table 3.11: Roughness and type of lamella of each indent of Zone 7.

<sup>\*2</sup> Even if located on a thin lamella, these indents seem to be in proximity to thicker ones, potentially impacting the results.

<sup>\*3</sup> Although situated within a thick lamella, these indents appear to be adjacent to thinner lamellae, which could potentially influence the observed outcomes.

The computation of lamella widths was carried out using FIJI, and the outcomes are illustrated in FIGURE 3.30. Thick lamellae have a width on average of  $2.54 \pm 0.46 \mu\text{m}$  while the thin one displays an average of  $1.46 \pm 0.35 \mu\text{m}$ . The significance is  $p = 0.0159$ .

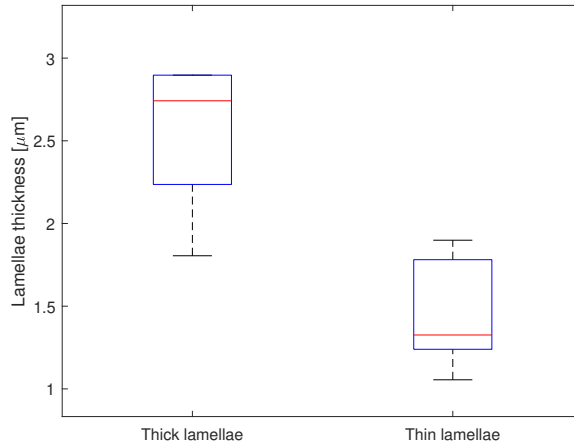
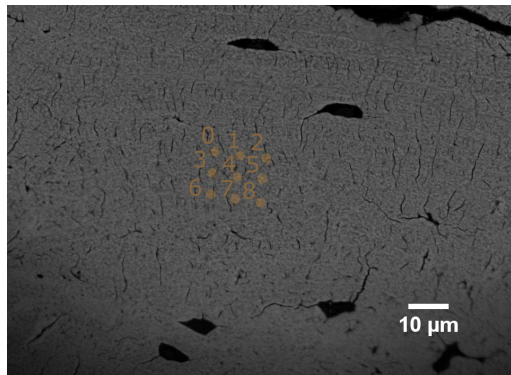


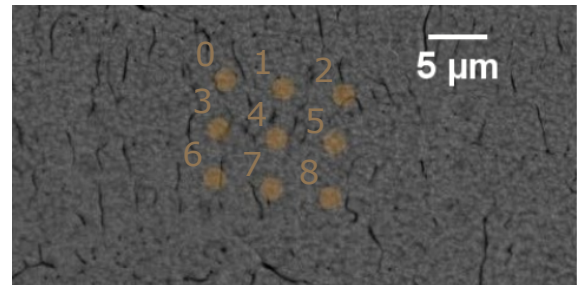
Figure 3.30: Boxplot of the lamella width in Zone 7.

### ► Zone 8

FIGURE 3.31 showcases Zone 8, located in the parallel fibered layer. However, the boundaries of this figure are also not discernible. To improve visibility, contrast enhancement and zooming techniques are applied. The resulting magnified image, displayed in FIGURE 3.31b, provides a clearer view of the indentation location. These pictures was taken with an acceleration voltage of 10 keV.



(a)



(b)

Figure 3.31: SEM pictures of zone 8 a) Indentation zone b) Zoom of the indentation zone with a change in contrast.

It is worth mentioning that both indents 2 and 6 are positioned along a canaliculi, potentially impacting the observed outcomes. Additionally, indents 3 and 7 are in close proximity to canaliculi as well.



### ► Zone 9

FIGURE 3.32 displays Zone 9, situated in the parallel fibered layer, where the boundaries are distinguishable without any modification needed. However, to offer a clearer view of the indentation location, we provide a zoomed of the region of interest in FIGURE 3.32b. The pictures was taken with an acceleration voltage of 10 keV.

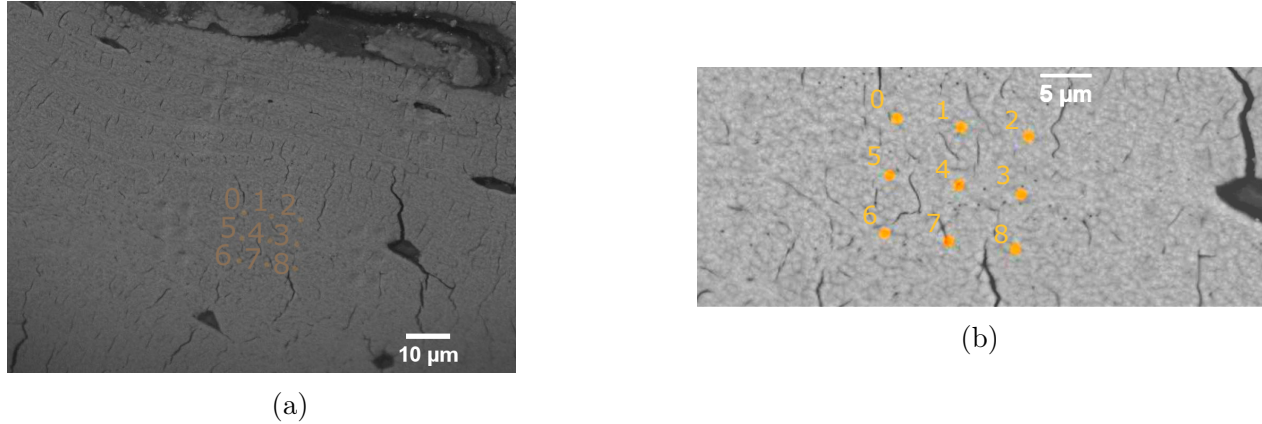


Figure 3.32: SEM pictures of zone 9 a) Indentation zone b) Zoom of the indentation zone.

Certainly, it is noteworthy that both indents 6 and 7 are situated in close proximity to a canaliculi, which could potentially influence the observed outcomes. Furthermore, indent 4 is positioned directly on an emerging canaliculi.

# Chapter 4

## Discussion

This chapter is dedicated to the discussion. The first section discuss about the SEM pictures obtained and on which information we can extract and compare to the literature. The second part is devoted to the results obtained with the nanoindentation tests. Then a section is dedicated to outlining the limitations of the obtained results. Finally the consideration of potential avenues for future research is discussed.

### 4.1 Scanning electron microscopy

From the Scanning electron microscopy (SEM), several OBSERVATIONS can be attested.

First of all, what has bee refereed to as thick lamellae are, actually, thick lamellae, whereas the black ones are thin lamellae. This association becomes evident when linking the SEM image with its corresponding SPM image, as depicted in FIGURES 3.27 and 3.9b respectively. For example, in these images, the indent labelled as 0 in the SEM picture is situated within a thick lamella, whereas the indent labelled as 4 is within a thin lamella. In the SPM image, the indent labelled as 0 is categorised as a thick lamella, while the indent labelled as 4 is categorised as a black one. Throughout the remainder of this thesis, the term thin and thick are used.

Secondly, upon observing the SEM images within the parallel-fibered bone layer, one can discern the existence of canaliculi and osteocytes, aligning with findings presented by Rotem Almany Magal et al. [37]. These canaliculi also exhibit a discernible preferred direction, and as certain indents coincide with their presence, it may potentially impact the measurements. The implications of this influence are elaborated in SECTION 4.3.

Lastly, with regard to the lamellae thickness of fibrolamellar bone, there is no relevant information in the current literature to the best of our knowledge. Fortunately, as previously stated in SECTION 1, Pauline Muraro, a former student, conducted a master thesis focusing on fibrolamellar bone focused on fibrolamellar bone. The student's research revealed that

thin lamellae measure between 1.39 and 2.6  $\mu\text{m}$ , while thick lamellae range from 2.79 to 4.65  $\mu\text{m}$ . These measurements are consistent with our findings. Furthermore, a comparison can be drawn between the thickness of lamellae in fibrolamellar bone and lamellae in osteons. In a study conducted by Zhou et al. (2020) [67] on bovine cortical bone, it was determined that thick lamellae possess a width ranging from approximately 2.8 to 13.8  $\mu\text{m}$ , while thin lamellae measure between 1.7 and 2.4  $\mu\text{m}$ . Interestingly, our findings once again align with these results, despite the relatively high upper limit for thick lamellae, which was not observed in fibrolamellar bone. This difference can be due to the technique Zhou et al. employed known as Peakforce tapping Atomic Force Microscopy. Our findings align better with the thickness of lamellae observed in human osteonal bone, where thin lamellae generally fall within the range of 1 to 3  $\mu\text{m}$ , while thick lamellae tend to measure between 3 and 6  $\mu\text{m}$  [68].

## 4.2 Static indentation

Based on the static indentation data, it can be inferred that the thick lamellae are stiffer than the thin ones, with a statistically significant level of  $p = 0.0411$ . However, when compared to Pauline's findings, who reported a storage modulus of  $40.46 \pm 3.56$  GPa for thick lamellae and  $32.8 \pm 4.17$  GPa for thin lamellae, the values are not closely aligned with our obtained results of  $17.90 \pm 2.26$  GPa for thin lamellae and  $21.23 \pm 2.37$  GPa for thick lamellae. The substantial discrepancy in our findings can be attributed to the methodologies employed. Indeed, Pauline utilised the modulus mapping method, a technique that involves scanning the sample's surface with low penetration. In contrast, I employed the model proposed by Olivier-Pharr.

In comparison with the existing literature, a study conducted by Zhou et al. (2020) [67] on bovine cortical bone highlighted that thick lamellae exhibited higher stiffness compared to thin ones, registering a modulus of  $21.49 \pm 6.58$  GPa for thick lamellae and  $9.67 \pm 2.69$  GPa for thin lamellae. The value obtained for thick lamellae harmonises with our result while the value of thin lamellae is notably lower than our computed value. This difference in the higher value could potentially be attributed to the variations in the method used, as previously explained (Zhou et al. used Peakforce tapping AFM). Moreover, it is important to note that the samples they tested were hydrated, which is known to have an impact on the mechanical properties as explained in SECTION 4.4. Our findings can also be contrasted with those obtained by Gupta et al. (2006) [69] and Xu et al. (2003) [68] in their studies on human bone. They reported a modulus ranging from 23 to 27 GPa for thick lamellae and 21 to 24 GPa for thin lamellae. These measurements are slightly higher than our obtained values, a difference that might be attributed to the tip they used. Indeed, they employed a Berkovich indenter tip, resulting in higher penetration into the material compared to a conospherical one.

### 4.3 Stress-strain curves

In this section, the different curves obtained are discussed and a comparison between the different zones of indentation is given.

#### 4.3.1 Parallel-fibered bone

The stress-strain curves observed for indents positioned near a canaliculi (e.g. indent 6 in Zone 8 FIGURE 3.31b) or on it exhibits a behaviour resembling that of trabecular bone when subjected to compression (FIGURE 1.6). This behaviour becomes evident through the delineation of three distinct phases: an initial linear elastic response, followed by a plateau, and concluding with a densification phase, as depicted in FIGURE 3.22c. This pattern can be comprehended by examining how trabecular bone responds to pressure. Under pressure, the trabeculae within the bone initiate a process of collapsing, a phenomenon attributed to the presence of pores. When pressure is exerted, the interconnected pores and voids within the trabecular structure undergo compression, ultimately leading to the collapse of the trabeculae [1]. Given that osteocyte lacuno canaliculi network are considered a type of pore in bone tissues, and considering the proximity of these indents to such regions, it is reasonable to infer that a similar process could be occurring for these indents.

On the other hand, the remaining indents display a rather consistent behaviour, characterised by a linear relationship between stress and strain. Notably, these indents exhibit a substantial slope, aligning with the findings of Pauline, who discovered that the storage modulus is notably high for indents located within parallel-fibered bone [44]. Based on these observations, it is reasonable to infer that parallel-fibered bone material possesses significant stiffness.

#### 4.3.2 Lamellar bone

As mentioned earlier, two specimens were employed to compute the different stress-strain curves. The initial sample appears to have a higher roughness compared to the second one. The variation in roughness becomes evident when observing the optical microscopy images. Indeed, in for Sample 2, the fibrolamellar bone exhibits a clearer appearance, causing the lamellae to be more challenging to discern. This surface roughness has been observed to influence the resulting curves.

In general, all the stress-strain curves initially undergo a linear increase, halting at approximately 2% strain and 0.2 GPa stress. This segment of the curves corresponds to the material's elastic phase. When the applied load is below the yield stress (in this instance, 0.2 GPa), the bone will revert to its original shape once the load is removed. Subsequently, the bone enters the plastic deformation phase, during which it does not fully recover its initial shape after the load is released. To evaluate the stiffness of a material, the slope of the elastic phase, known as the Young's modulus, is analysed. A higher Young's modulus value

indicates a greater stiffness in the material.

In the case of Sample 1, a general observation is that thin lamellae exhibit higher stiffness compared to thick ones. This finding contradicts the results obtained from the static indentation tests, which demonstrate the opposite relationship. Furthermore, these findings also diverge from the results presented by Pauline, who asserted that thin lamellae are the stiffest [44]. These discrepancies can be attributed to surface roughness. For instance, in the case of certain indents, such as indent 6 in Zone 3 (FIGURE 3.4b), the observations align with the expectation that thick lamellae are indeed stiffer. Notably, the roughness at this specific indent is relatively low.

On the other hand, in Sample 2, it is evident that the thick lamellae exhibit greater stiffness, aligning with the findings put forth by Pauline [44]. The disparity in results could potentially arise from variations in surface roughness. In this particular sample, the roughness is noticeably reduced.

### 4.3.3 Impact of roughness

When observing the behaviour of thick lamellae, a consistent pattern emerges, particularly starting from a pre-load of 10. The initial 5-6 data points follow a steep linear trend, after which yielding occurs. By identifying the yield stress within this yielding phase, an estimated value of approximately 0.23-0.25 GPa is obtained. This value is intriguing because the macroscopic yield stress of cortical bone is considerably lower, averaging  $147.89 \pm 16.36$  MPa as reported by Mirzaali et al. (2016) [70], making it nearly twice as small. This difference may stem from the fact that the analysis conducted here operates at a local level, specifically testing the individual fibers themselves. In contrast, the other analysis is performed at a macroscopic level, encompassing the overall tissue. This comparison essentially contrasts properties at the microstructural (fibers) level versus those of the larger tissue.

On the other hand, for thin lamellae, the points forming a linear trend are slightly fewer, and the yield stress appears slightly lower, around 0.2 GPa. With the roughness flattened out, these lamellae seem to exhibit a more compliant behaviour. Moreover a gradual increase in the stress-strain curves can be seen. The different mechanical behaviour between thick and thin lamellae might arise from the varying orientations of collagen fibers.

Considering these findings, an observation can be drawn regarding the reproducibility of the results. It seems that when a pre-load function is applied to level the results, there is an enhancement in the consistency (FIGURES 3.16 and 3.18).

## 4.4 Limitations

The primary limitation to acknowledge is that all the bone samples underwent dehydration, a process known to affect mechanical properties, as discussed in previous studies. Indeed, it was discovered that in the dehydrated sample, the Young's modulus was increased. [43].

Secondly, another significant limitation relates to the annotated SEM images. Even though great care was taken in their generation, confirming the precise localisation of the indentation remains a challenging task, lacking absolute certainty.

Furthermore, an additional limitation stemmed from the constrained number of samples employed. Because of the limited time available, only two samples were at our disposal for test execution. Consequently, there was insufficient time to conduct a more comprehensive series of tests.

Last but not least, the nanoindenter is a device designed to measure extremely small loads and displacements. Consequently, it exhibits high sensitivity and demands meticulous calibration. Additionally, a low surface roughness is essential, as it significantly influences the outcomes. To mitigate this effect, a pre-load is necessary to flatten the surface roughness.

Finally, the last limitation pertains to the load function used. It would be highly beneficial to incorporate additional cycles within the load range of 0-0.3 GPa. This augmentation could significantly enhance our ability to capture responses under low loads. Consequently, stress-strain curves would more accurately represent behaviour in this low-stress regime, and pinpointing the yield point would become a more straightforward task.

## 4.5 Future Works

In the context of future research, it is worth exploring the impact of surface roughness in greater detail. Notably, our current analysis focused primarily on roughness effects within a single zone. However, an intriguing avenue for future investigation involves expanding this analysis to encompass multiple zones. This can also be combined by using different pre-load than the one established in the context of this thesis. Moreover, one could use the Finite Element Method (FEM) to reconstruct the bone and conduct simulations to verify the accuracy of the results, as well as to assess the impact of surface roughness.

Another intriguing approach is to delve deeper into the investigation of the exact location of the indentation. It is worth noting that there is not absolute certainty that the indentation occurred precisely where we initially indicated, even with the SEM image. To address this, a potential solution is to strategically mark the area of the specimen where the indentations were carried out using additional static indents. By doing so, the alignment of the SEM im-

age with the graph containing coordinates of all indentation points becomes more accurate and precise.

In conclusion, as soon as the impact of roughness is comprehended and the accuracy of indent location is enhanced, there is potential to delve deeper into the examination of fibrolamellar bone. Exploring additional samples could also be pursued to gather more data, consequently enabling more comprehensive statistical analyses to be conducted. Additionally, similar investigations could be conducted on human bone or on other biomaterials, thereby broadening the scope of research in this field.

# Conclusion

The aims of this thesis were twofold: firstly, to enhance the understanding of the mechanical attributes demonstrated by fibrolamellar bone, achieved through an intricate examination of its stress-strain behaviour with a specific emphasis on the lamellar region. Secondly, the goal was to gain a deeper insight into the effects of surface roughness variations on the conducted analyses. To achieve this, the nanoindentation technique is employed, providing precise analysis at the nanoscale level. By integrating the acquired data with the Olivier-Pharr model, stress-strain curves can be computed.

The project's initial phase centres on calibration methods, leading to the determination of the subsequent points:

- The choice of the calibration dataset holds significant importance. It is crucial to consider both the environmental conditions during indentation and ensure that the points acquired are obtained under low load conditions.
- The choice of the fitting equation is also of critical importance, as an ill-suited selection can yield to inaccurate results. This becomes particularly evident when dealing with low loads.

The second phase concentrates on establishing and analysing stress-strain curves, yielding the following observations:

- Parallel-fibered bone displays higher stiffness compared to other structures.
- Thin and thick lamellae coexist within the lamellar bone structure. Notably, the thick lamellae exhibit higher stiffness than their thin counterparts. However, this observation might not be immediately evident when tests are conducted on samples with higher surface roughness.
- The curves originating from thick lamellae exhibit an initial linear elastic phase followed by a rapid transition to yielding. In contrast, the curves from thin lamellae demonstrate a more compliant behaviour. This distinction is probably due to the variation in collagen fiber orientation between the thick and thin lamellae.
- Lamellar bone exhibits similarities with osteons, encompassing distinctions in lamellar size and modulus.



- The roughness need to be flatten using pre-load.

This study represents a pioneering effort, introducing a method capable of elucidating and connecting mechanical properties to underlying structures. In subsequent research, this methodology can be extended to further comprehend the impact of roughness on fibrolamellar bone, or even applied to osteons to establish connections given their shared characteristics.

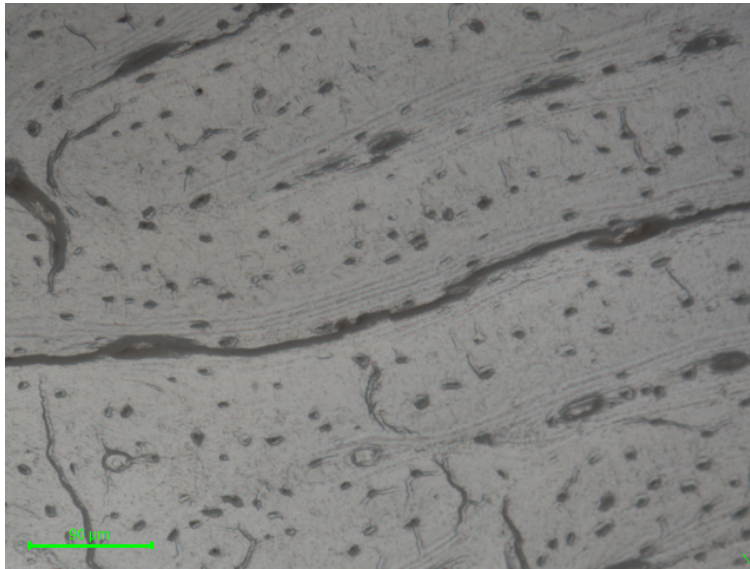
# Appendices

# Appendix A

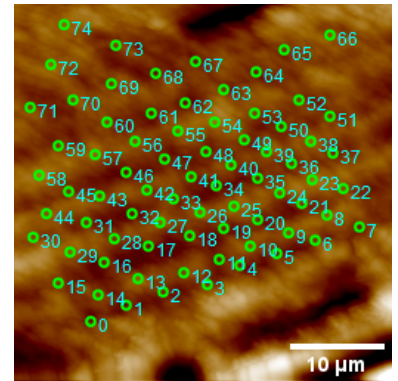
## Nanoindentation test

The stress-strain curves displayed in the following sections were obtained using the same protocol as describe in SECTION 2.2.5 but the dataset chosen is CAL0.

### A.1 Zone 1b



(a)



(b)

Figure A.1: Indentation zone 1b a) Optical view b) Topographical SPM picture.

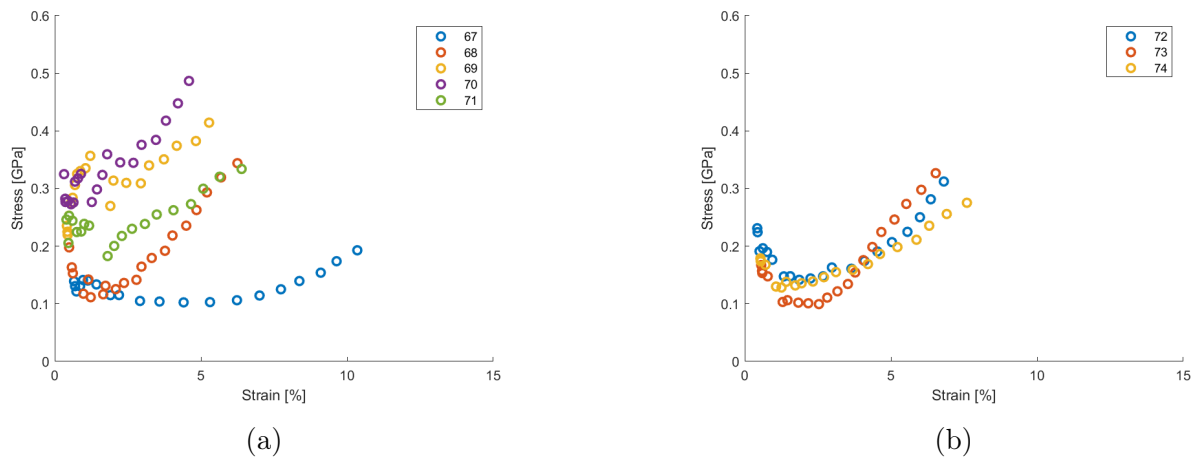


Figure A.2: Stress-strain curves in Zone 1b for indent on parallel-fibered bone.

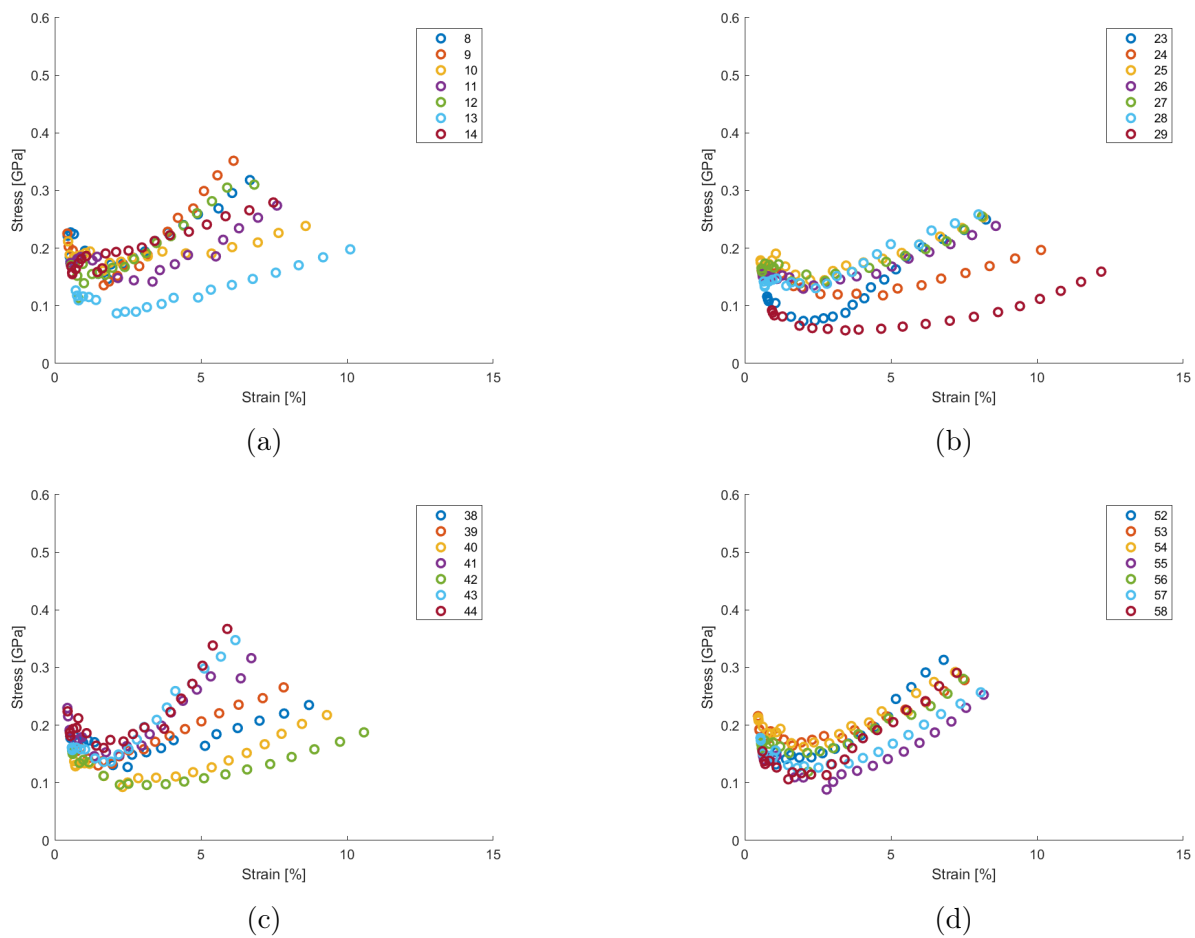


Figure A.4: Stress-strain curves in Zone 1b for indent on white lamellae.

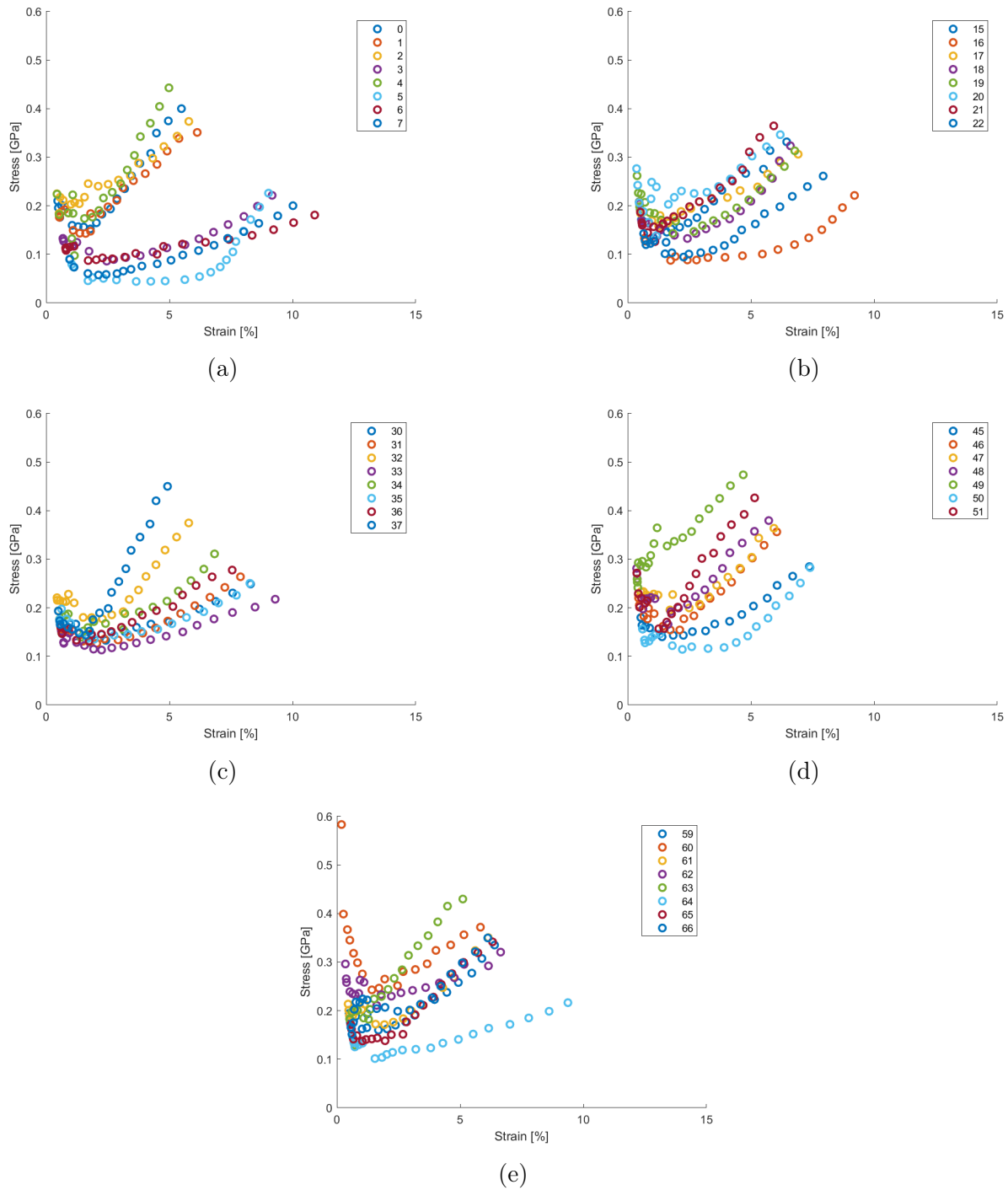


Figure A.3: Stress-strain curves in Zone 1b for indent on black lamellae.

## A.2 Zone 1c

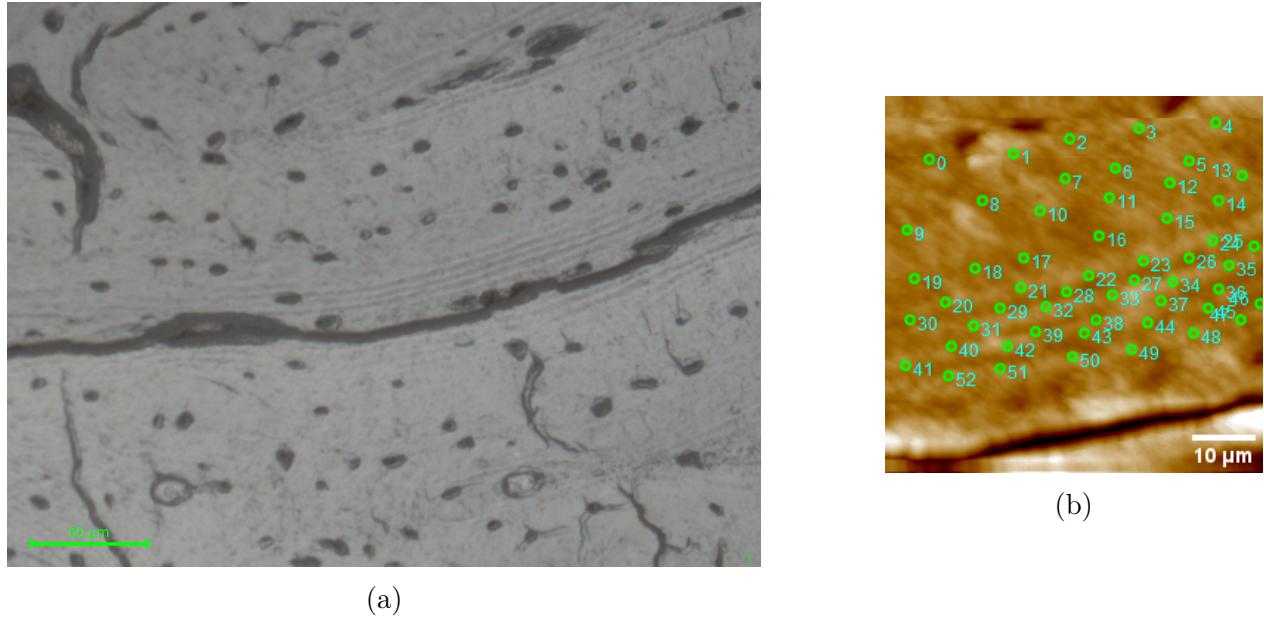


Figure A.5: Indentation zone 1c a) Optical view b) Topographical SPM picture.

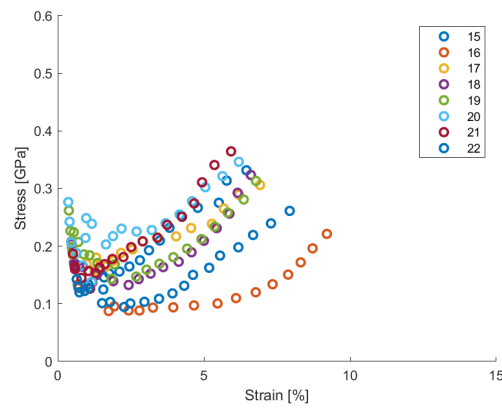


Figure A.6: Stress-strain curves in Zone 1c for indent on parallel-fibered bone.

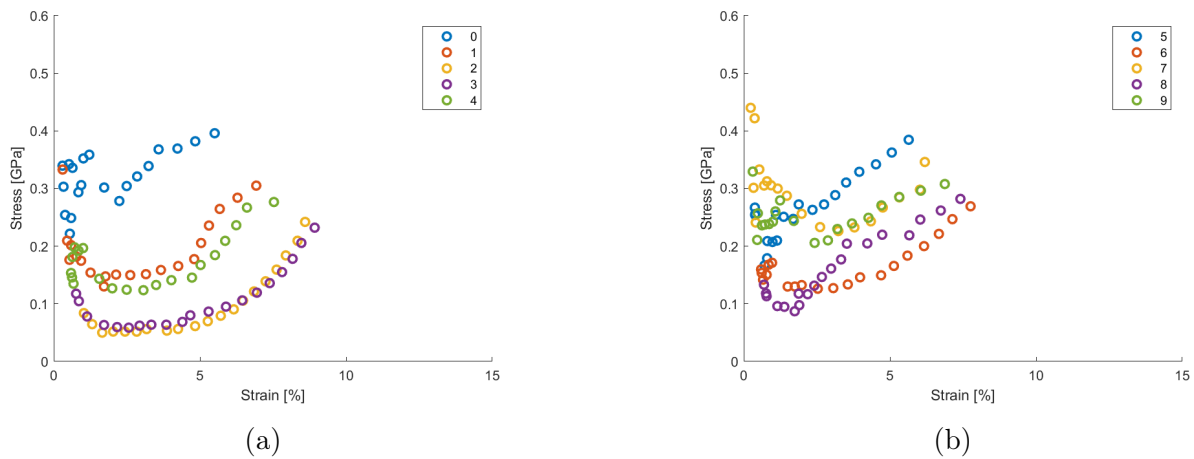


Figure A.7: Stress-strain curves in Zone 1c for indent on parallel-fibered bone or hypercalcified bone.

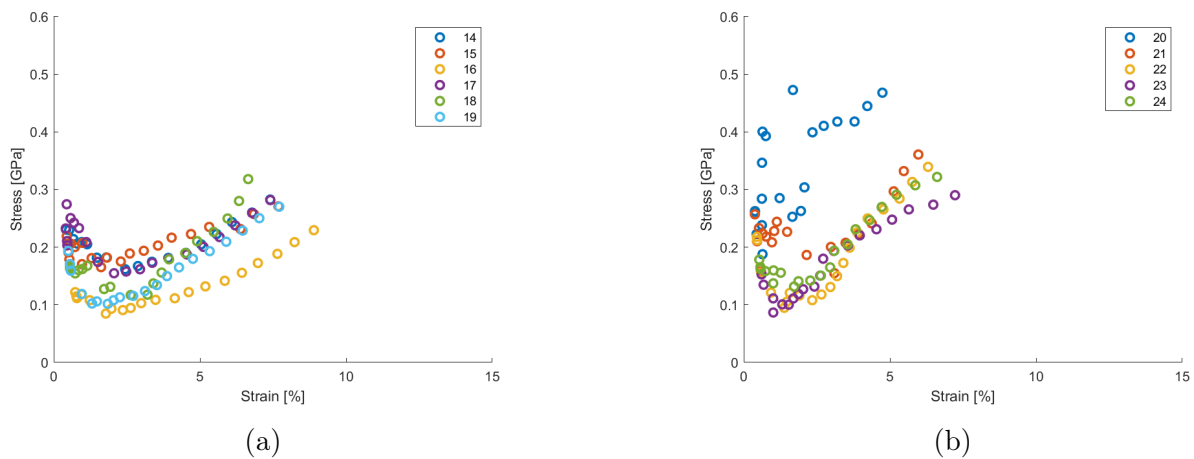


Figure A.8: Stress-strain curves in Zone 1c for indent on parallel-fibered bone or a) on black lamellae b) on white lamellae.

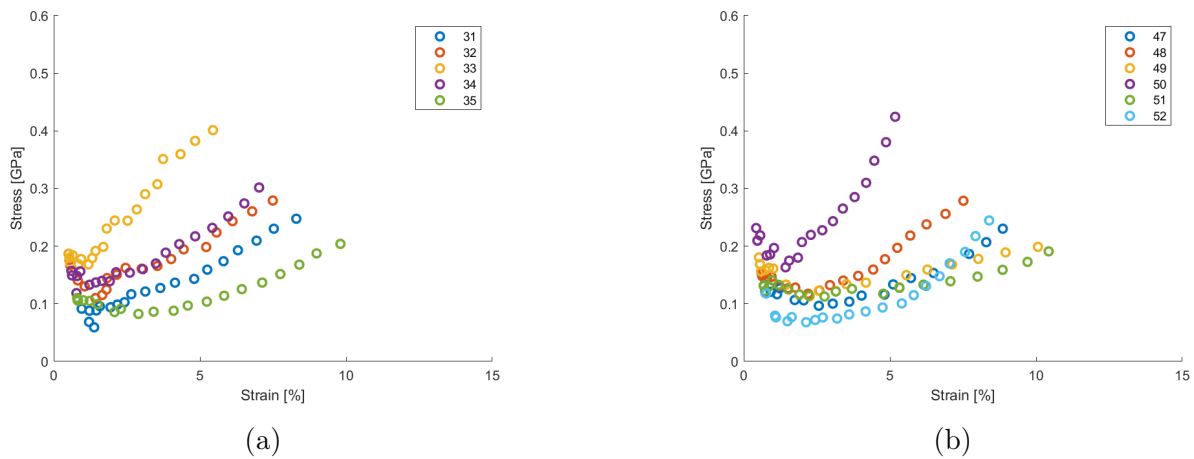


Figure A.9: Stress-strain curves in Zone 1c for indent on white lamellae.

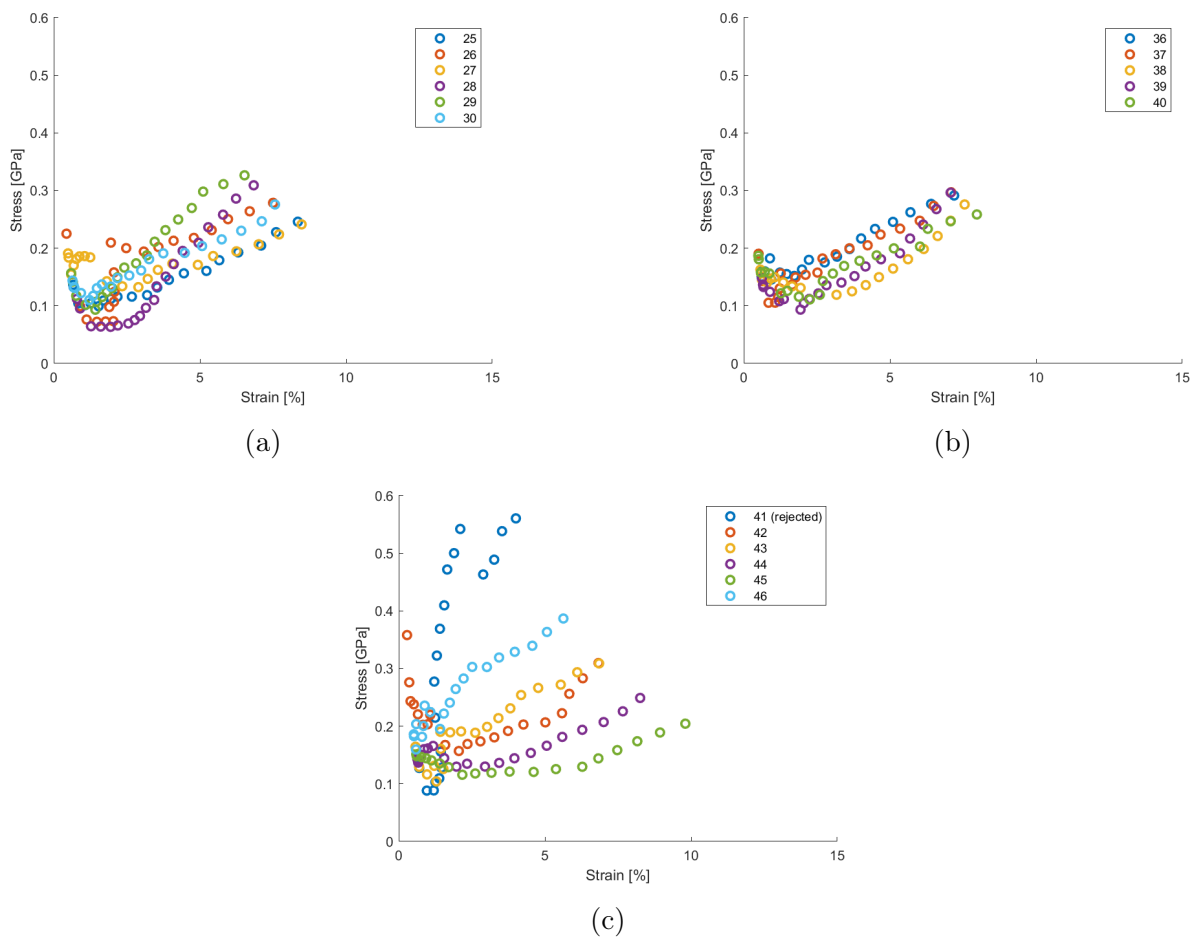


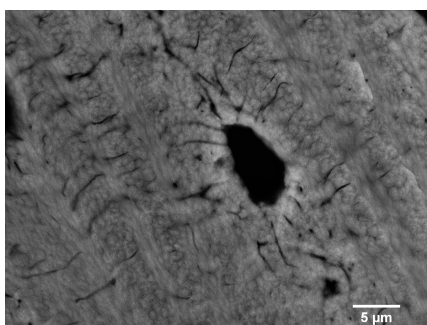
Figure A.10: Stress-strain curves in Zone 1c for indent on black lamellae.



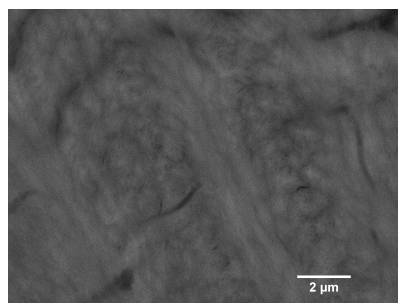
# Appendix B

## SEM picture

### B.1 Sample 1



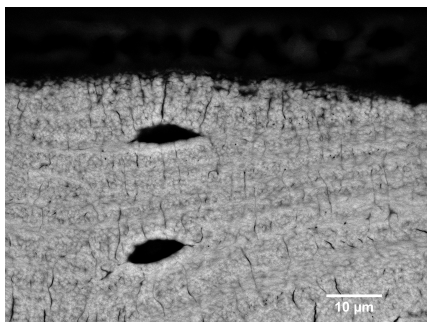
(a)



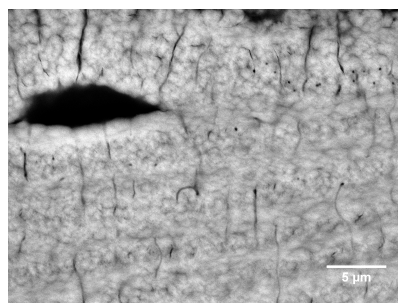
(b)

Figure B.1: SEM pictures of Sample 1.

### B.2 Sample 2



(a)



(b)

Figure B.2: SEM pictures of Sample 2.

# Bibliography

- [1] Christopher Ross Ethier and Craig A. Simmons. *Introductory biomechanics: from cells to organisms*. en. 13th printing. Cambridge texts in biomedical engineering. Cambridge: Cambridge University Press, 2018. ISBN: 978-0-521-84112-2.
- [2] Bart Clarke. “Normal bone anatomy and physiology”. In: *Clinical journal of the American Society of Nephrology* 3.Supplement 3 (2008), S131–S139.
- [3] Davide Ruffoni. *GBIO0012-2 : Biomechanics (slides)*. en. University of Liege, 2021.
- [4] Marco Lambert. *Le système squelettique et musculaire chez l’humain*. fr. Nov. 2014. URL: [https://16.ticfga.ca/files/old/IMG/pdf/BIO\\_5066-1\\_Guide\\_d\\_apprentissage\\_CEB-2.pdf](https://16.ticfga.ca/files/old/IMG/pdf/BIO_5066-1_Guide_d_apprentissage_CEB-2.pdf).
- [5] Shyni Varghese and Adam J Engler. “Bone Biomechanics”. en. In: *Orthopaedic Biomechanics*. CRC Press, Dec. 2012, pp. 3–47.
- [6] J Gordon Betts et al. “Anatomy & Physiology”. en. In: ().
- [7] Matthew R. Allen, Janet M. Hock, and David B. Burr. “Periosteum: biology, regulation, and response to osteoporosis therapies”. en. In: *Bone* 35.5 (Nov. 2004), pp. 1003–1012. ISSN: 87563282. DOI: 10.1016/j.bone.2004.07.014.
- [8] Michael J.F. Blumer. “Bone tissue and histological and molecular events during development of the long bones”. en. In: *Annals of Anatomy - Anatomischer Anzeiger* 235 (May 2021), p. 151704. ISSN: 09409602. DOI: 10.1016/j.aanat.2021.151704.
- [9] Justin L. Brown, Sangamesh G. Kumbar, and Cato T. Laurencin. “Bone Tissue Engineering”. en. In: *Biomaterials Science*. Elsevier, 2013, pp. 1194–1214. ISBN: 978-0-12-374626-9. DOI: 10.1016/B978-0-08-087780-8.00113-3.
- [10] OpenStaxCollege. *Bone Structure*. URL: <https://pressbooks-dev.oer.hawaii.edu/anatomyandphysiology/chapter/bone-structure/> (visited on 07/03/2023).
- [11] Tony M. Keaveny et al. “Biomechanics of Trabecular Bone”. en. In: *Annual Review of Biomedical Engineering* 3.1 (Aug. 2001), pp. 307–333. ISSN: 1523-9829, 1545-4274. DOI: 10.1146/annurev.bioeng.3.1.307.
- [12] R. Bruce Martin et al. *Skeletal Tissue Mechanics*. en. New York, NY: Springer New York, 2015. ISBN: 978-1-4939-3001-2 978-1-4939-3002-9. DOI: 10.1007/978-1-4939-3002-9.

- [13] M Ding and I Hvid. “Quantification of age-related changes in the structure model type and trabecular thickness of human tibial cancellous bone”. en. In: *Bone* 26.3 (Mar. 2000), pp. 291–295. ISSN: 87563282. DOI: 10.1016/S8756-3282(99)00281-1.
- [14] Peter Fratzl and Richard Weinkamer. “Nature’s hierarchical materials”. en. In: *Progress in Materials Science* 52.8 (Nov. 2007), pp. 1263–1334. ISSN: 00796425. DOI: 10.1016/j.pmatsci.2007.06.001.
- [15] G.H. Van Lenthe, M. Stauber, and R. Müller. “Specimen-specific beam models for fast and accurate prediction of human trabecular bone mechanical properties”. en. In: *Bone* 39.6 (Dec. 2006), pp. 1182–1189. ISSN: 87563282. DOI: 10.1016/j.bone.2006.06.033.
- [16] Matthias Mähr et al. “Increased Osteocyte Lacunae Density in the Hypermineralized Bone Matrix of Children with Osteogenesis Imperfecta Type I”. en. In: *International Journal of Molecular Sciences* 22.9 (Apr. 2021), p. 4508. ISSN: 1422-0067. DOI: 10.3390/ijms22094508.
- [17] Ramin Oftadeh et al. “Biomechanics and Mechanobiology of Trabecular Bone: A Review”. en. In: *Journal of Biomechanical Engineering* 137.1 (Jan. 2015), p. 010802. ISSN: 0148-0731, 1528-8951. DOI: 10.1115/1.4029176.
- [18] Xiran Cai et al. “Anisotropic elastic properties of human femoral cortical bone and relationships with composition and microstructure in elderly”. In: *Acta Biomaterialia* 90 (2019), pp. 254–266. ISSN: 1742-7061. DOI: <https://doi.org/10.1016/j.actbio.2019.03.043>.
- [19] John D. Currey. *Bones: structure and mechanics*. Princeton university press, 2006. ISBN: 0-691-12804-9.
- [20] Ulrike G. K. Wegst et al. “Bioinspired structural materials”. en. In: *Nature Materials* 14.1 (Jan. 2015), pp. 23–36. ISSN: 1476-1122, 1476-4660. DOI: 10.1038/nmat4089.
- [21] Amnon Sharir, Meir Max Barak, and Ron Shahar. “Whole bone mechanics and mechanical testing”. en. In: *The Veterinary Journal* 177.1 (July 2008), pp. 8–17. ISSN: 10900233. DOI: 10.1016/j.tvjl.2007.09.012.
- [22] D. J. Hadjidakis and I. I. Androulakis. “Bone Remodeling”. en. In: *Annals of the New York Academy of Sciences* 1092.1 (Dec. 2006), pp. 385–396. ISSN: 0077-8923. DOI: 10.1196/annals.1365.035.
- [23] Liza J. Raggatt and Nicola C. Partridge. “Cellular and Molecular Mechanisms of Bone Remodeling”. en. In: *Journal of Biological Chemistry* 285.33 (Aug. 2010), pp. 25103–25108. ISSN: 00219258. DOI: 10.1074/jbc.R109.041087.
- [24] Robert L. Jilka. “Biology of the basic multicellular unit and the pathophysiology of osteoporosis”. en. In: *Medical and Pediatric Oncology* 41.3 (Sept. 2003), pp. 182–185. ISSN: 0098-1532, 1096-911X. DOI: 10.1002/mpo.10334.
- [25] Petar Milovanovic et al. “Bone tissue aging affects mineralization of cement lines”. en. In: *Bone* 110 (May 2018), pp. 187–193. ISSN: 87563282. DOI: 10.1016/j.bone.2018.02.004.

- [26] M. Doblaré, J.M. Garcia, and M.J. Gómez. “Modelling bone tissue fracture and healing: a review”. en. In: *Engineering Fracture Mechanics* 71.13-14 (Sept. 2004), pp. 1809–1840. ISSN: 00137944. DOI: 10.1016/j.engfracmech.2003.08.003.
- [27] Xu Feng and Jay M. McDonald. “Disorders of Bone Remodeling”. en. In: *Annual Review of Pathology: Mechanisms of Disease* 6.1 (Feb. 2011), pp. 121–145. ISSN: 1553-4006, 1553-4014. DOI: 10.1146/annurev-pathol-011110-130203.
- [28] Jae-Young Rho, Liisa Kuhn-Spearing, and Peter Zioupos. “Mechanical properties and the hierarchical structure of bone”. en. In: *Medical Engineering & Physics* 20.2 (Mar. 1998), pp. 92–102. ISSN: 13504533. DOI: 10.1016/S1350-4533(98)00007-1.
- [29] Natalie Reznikov, Ron Shahar, and Steve Weiner. “Bone hierarchical structure in three dimensions”. en. In: *Acta Biomaterialia* 10.9 (Sept. 2014), pp. 3815–3826. ISSN: 17427061. DOI: 10.1016/j.actbio.2014.05.024.
- [30] Fayez F. Safadi et al. “Bone Structure, Development and Bone Biology”. en. In: *Bone Pathology*. Ed. by Jasvir S. Khurana. Totowa, NJ: Humana Press, 2009, pp. 1–50. ISBN: 978-1-58829-766-2 978-1-59745-347-9. DOI: 10.1007/978-1-59745-347-9\_1.
- [31] W. Wagermaier et al. “Spiral twisting of fiber orientation inside bone lamellae”. en. In: *Biointerphases* 1.1 (Mar. 2006), pp. 1–5. ISSN: 1934-8630, 1559-4106. DOI: 10.1116/1.2178386.
- [32] Ramnath Ramachandran (Ram). *HIERARCHY OF BONE STRUCTURE*. Report. Complex Polymer Morphology, 2006. URL: [https://www.eng.uc.edu/~beaucag/Classes/MorphologyofComplexMaterials/Hierarchy\\_of\\_Bone\\_Structure.pdf](https://www.eng.uc.edu/~beaucag/Classes/MorphologyofComplexMaterials/Hierarchy_of_Bone_Structure.pdf).
- [33] P. Fratzl et al. “Structure and mechanical quality of the collagen–mineral nano-composite in bone”. en. In: *J. Mater. Chem.* 14.14 (2004), pp. 2115–2123. ISSN: 0959-9428, 1364-5501. DOI: 10.1039/B402005G.
- [34] Yan Liu, Dan Luo, and Tie Wang. “Hierarchical Structures of Bone and Bioinspired Bone Tissue Engineering”. en. In: *Small* 12.34 (Sept. 2016), pp. 4611–4632. ISSN: 16136810. DOI: 10.1002/smll.201600626.
- [35] Helena Kuivaniemi and Gerard Tromp. “Type III collagen (COL3A1): Gene and protein structure, tissue distribution, and associated diseases”. en. In: *Gene* 707 (July 2019), pp. 151–171. ISSN: 03781119. DOI: 10.1016/j.gene.2019.05.003.
- [36] AnaMaria Abreu-Velez and MichaelS Howard. “Collagen IV in normal skin and in pathological processes”. en. In: *North American Journal of Medical Sciences* 4.1 (2012), p. 1. ISSN: 1947-2714. DOI: 10.4103/1947-2714.92892.
- [37] Rotem Almany Magal et al. “Three-dimensional structure of minipig fibrolamellar bone: Adaptation to axial loading”. en. In: *Journal of Structural Biology* 186.2 (May 2014), pp. 253–264. ISSN: 10478477. DOI: 10.1016/j.jsb.2014.03.007.

- [38] Michael Kerschnitzki et al. “Poorly Ordered Bone as an Endogenous Scaffold for the Deposition of Highly Oriented Lamellar Tissue in Rapidly Growing Ovine Bone”. en. In: *Cells Tissues Organs* 194.2-4 (2011), pp. 119–123. ISSN: 1422-6405, 1422-6421. DOI: 10.1159/000324467.
- [39] Ryoichi Mori et al. “Histological and physicochemical studies of hypercalcified primar lines in the laminar bone of young calves”. en. In: *Anatomical Science International* 82.2 (June 2007), pp. 108–115. ISSN: 1447-6959, 1447-073X. DOI: 10.1111/j.1447-073X.2007.00178.x.
- [40] Michael Kerschnitzki et al. “The organization of the osteocyte network mirrors the extracellular matrix orientation in bone”. en. In: *Journal of Structural Biology* 173.2 (Feb. 2011), pp. 303–311. ISSN: 10478477. DOI: 10.1016/j.jsb.2010.11.014.
- [41] John W. Barrera, Adeline Le Cabec, and Meir M. Barak. “The orthotropic elastic properties of fibrolamellar bone tissue in juvenile white-tailed deer femora”. en. In: *Journal of Anatomy* 229.4 (Oct. 2016), pp. 568–576. ISSN: 00218782. DOI: 10.1111/joa.12500.
- [42] Gunthard Benecke et al. “Digital image correlation shows localized deformation bands in inelastic loading of fibrolamellar bone”. en. In: *Journal of Materials Research* 24.2 (Feb. 2009), pp. 421–429. ISSN: 0884-2914, 2044-5326. DOI: 10.1557/JMR.2009.0064.
- [43] Jong Seto et al. “Tough Lessons From Bone: Extreme Mechanical Anisotropy at the Mesoscale”. en. In: *Advanced Functional Materials* 18.13 (July 2008), pp. 1905–1911. ISSN: 1616301X, 16163028. DOI: 10.1002/adfm.200800214.
- [44] P Muraro. “Biomechanical characterization of fibrolamellar bone using nano-scale modulus mapping”. en. In: ().
- [45] K.D. Vernon-Parry. “Scanning electron microscopy: an introduction”. en. In: *III-Vs Review* 13.4 (July 2000), pp. 40–44. ISSN: 09611290. DOI: 10.1016/S0961-1290(00)80006-X.
- [46] Kalsoom Akhtar et al. “Scanning Electron Microscopy: Principle and Applications in Nanomaterials Characterization”. en. In: *Handbook of Materials Characterization*. Ed. by Surender Kumar Sharma. Cham: Springer International Publishing, 2018, pp. 113–145. ISBN: 978-3-319-92954-5 978-3-319-92955-2. DOI: 10.1007/978-3-319-92955-2\_4.
- [47] Astrid Weston. *Atomic and Electronic Properties of 2D Moiré Interfaces*. en. Springer Theses. Cham: Springer International Publishing, 2022. ISBN: 978-3-031-12092-3 978-3-031-12093-0. DOI: 10.1007/978-3-031-12093-0.
- [48] Azad Mohammed and Avin Abdullah. “SCANNING ELECTRON MICROSCOPY (SEM): A REVIEW”. en. In: ().

- [49] Furqan A. Shah, Krisztina Ruscsák, and Anders Palmquist. “50 years of scanning electron microscopy of bone—a comprehensive overview of the important discoveries made and insights gained into bone material properties in health, disease, and taphonomy”. en. In: *Bone Research* 7.1 (May 2019), p. 15. ISSN: 2095-6231. DOI: 10.1038/s41413-019-0053-z.
- [50] Wikipedia. *File:Electron emission mechanisms.svg*. URL: [https://en.wikipedia.org/wiki/File:Electron\\_emission\\_mechanisms.svg](https://en.wikipedia.org/wiki/File:Electron_emission_mechanisms.svg) (visited on 06/07/2023).
- [51] Warren C. Oliver and George M. Pharr. “Nanoindentation in materials research: Past, present, and future”. en. In: *MRS Bulletin* 35.11 (Nov. 2010), pp. 897–907. ISSN: 0883-7694, 1938-1425. DOI: 10.1557/mrs2010.717.
- [52] Li H. He and Michael V. Swain. “Nanoindentation derived stress–strain properties of dental materials”. en. In: *Dental Materials* 23.7 (July 2007), pp. 814–821. ISSN: 01095641. DOI: 10.1016/j.dental.2006.06.017.
- [53] Ran He et al. “Studies on mechanical properties of thermoelectric materials by nanoindentation: Studies on mechanical properties of thermoelectric materials”. en. In: *physica status solidi (a)* 212.10 (Oct. 2015), pp. 2191–2195. ISSN: 18626300. DOI: 10.1002/pssa.201532045.
- [54] W.C. Oliver and G.M. Pharr. “An improved technique for determining hardness and elastic modulus using load and displacement sensing indentation experiments”. en. In: *Journal of Materials Research* 7.6 (June 1992), pp. 1564–1583. ISSN: 0884-2914, 2044-5326. DOI: 10.1557/JMR.1992.1564.
- [55] W C Oliver and G M Pharr. “Measurement of hardness and elastic modulus by instrumented indentation: Advances in understanding and refinements to methodology”. en. In: *J. Mater. Res.* 19.1 (2004).
- [56] Eve Donnelly et al. “Effects of surface roughness and maximum load on the mechanical properties of cancellous bone measured by nanoindentation”. en. In: *Journal of Biomedical Materials Research Part A* 77A.2 (May 2006), pp. 426–435. ISSN: 1549-3296, 1552-4965. DOI: 10.1002/jbm.a.30633.
- [57] M. S. Bobji and S. K. Biswas. “Estimation of hardness by nanoindentation of rough surfaces”. en. In: *Journal of Materials Research* 13.11 (Nov. 1998), pp. 3227–3233. ISSN: 0884-2914, 2044-5326. DOI: 10.1557/JMR.1998.0438.
- [58] Sara E. Campbell, Virginia L. Ferguson, and Donna C. Hurley. “Nanomechanical mapping of the osteochondral interface with contact resonance force microscopy and nanoindentation”. en. In: *Acta Biomaterialia* 8.12 (Dec. 2012), pp. 4389–4396. ISSN: 17427061. DOI: 10.1016/j.actbio.2012.07.042.
- [59] Shahrouz Amini et al. “The role of quasi-plasticity in the extreme contact damage tolerance of the stomatopod dactyl club”. en. In: *Nature Materials* 14.9 (Sept. 2015), pp. 943–950. ISSN: 1476-1122, 1476-4660. DOI: 10.1038/nmat4309.

- [60] Tengting Tang et al. “Subcanalicular Nanochannel Volume Is Inversely Correlated With Calcium Content in Human Cortical Bone”. en. In: *Journal of Bone and Mineral Research* 38.2 (Feb. 2023), pp. 313–325. ISSN: 0884-0431, 1523-4681. DOI: 10.1002/jbmr.4753.
- [61] P Roschger et al. “Constant mineralization density distribution in cancellous human bone”. en. In: *Bone* 32.3 (Mar. 2003), pp. 316–323. ISSN: 87563282. DOI: 10.1016/S8756-3282(02)00973-0.
- [62] P Roschger et al. “Validation of quantitative backscattered electron imaging for the measurement of mineral density distribution in human bone biopsies”. en. In: *Bone* 23.4 (Oct. 1998), pp. 319–326. ISSN: 87563282. DOI: 10.1016/S8756-3282(98)00112-4.
- [63] Markus A. Hartmann et al. “Quantitative Backscattered Electron Imaging of Bone Using a Thermionic or a Field Emission Electron Source”. en. In: *Calcified Tissue International* 109.2 (Aug. 2021), pp. 190–202. ISSN: 0171-967X, 1432-0827. DOI: 10.1007/s00223-021-00832-5.
- [64] V. Jantou et al. “Focused ion beam milling and ultramicrotomy of mineralised ivory dentine for analytical transmission electron microscopy”. en. In: *Micron* 40.4 (June 2009), pp. 495–501. ISSN: 09684328. DOI: 10.1016/j.micron.2008.12.002.
- [65] Leo F. Johnson and K. A. Ingersoll. “Ion polishing with the aid of a planarizing film”. en. In: *Applied Optics* 22.8 (Apr. 1983), p. 1165. ISSN: 0003-6935, 1539-4522. DOI: 10.1364/AO.22.001165.
- [66] Gwyddion. *One-Dimensional Roughness Parameters*. URL: <http://gwyddion.net/documentation/user-guide-en/roughness-iso.html> (visited on 06/07/2023).
- [67] Yuxiao Zhou et al. “Elastic modulus mapping for bovine cortical bone from submillimeter-to submicron-scales using PeakForce Tapping atomic force microscopy”. en. In: *Extreme Mechanics Letters* 41 (Nov. 2020), p. 101031. ISSN: 23524316. DOI: 10.1016/j.eml.2020.101031.
- [68] J. Xu et al. “Atomic force microscopy and nanoindentation characterization of human lamellar bone prepared by microtome sectioning and mechanical polishing technique”. en. In: *Journal of Biomedical Materials Research* 67A.3 (Dec. 2003), pp. 719–726. ISSN: 0021-9304, 1097-4636. DOI: 10.1002/jbm.a.10109.
- [69] H.S. Gupta et al. “Mechanical modulation at the lamellar level in osteonal bone”. en. In: *Journal of Materials Research* 21.8 (Aug. 2006), pp. 1913–1921. ISSN: 0884-2914, 2044-5326. DOI: 10.1557/jmr.2006.0234.
- [70] Mohammad J. Mirzaali et al. “Mechanical properties of cortical bone and their relationships with age, gender, composition and microindentation properties in the elderly”. en. In: *Bone* 93 (Dec. 2016), pp. 196–211. ISSN: 87563282. DOI: 10.1016/j.bone.2015.11.018.